SANDIA REPORT
SAND98–1155
Unlimited Release
Printed June 1998

Cylindrical Target Li-beam-Driven Hohlraum Experiments

M. S. Derzon, J. Aubert, T. L. Barber, G. A. Chandler, D. K. Derzon, R. J. Dukart, D. L. Fehl, D. J. Johnson, E. J. McGuire, A. R. Moats, D. D. Noack, C. L. Ruiz

Prepared by
Sandia National Laboratories
Albuquerque, New Mexico 87185 and Livermore, California 94550

Sandia is a multiprogram laboratory operated by Sandia Corporation, a Lockheed Martin Company, for the United States Department of Energy under Contract DE-AC04-94AL85000.

Sandia National Laboratories

VI, 157p.

Issued by Sandia National Laboratories, operated for the United States Department of Energy by Sandia Corporation.

Available to DOE and DOE contractors from
Office of Scientific and Technical Information
P.O. Box 62
Oak Ridge, TN 37831

Prices available from (615) 576-8401, FTS 626-8401

Available to the public from
National Technical Information Service
U.S. Department of Commerce
5285 Port Royal Rd
Springfield, VA 22161

NTIS price codes
Printed copy: A08
Microfiche copy: A01

SAND98-1155
Unlimited Release
Printed June 1998

Cylindrical Target Li-beam-Driven Hohlraum Experiments

M. S. Derzon, J. Aubert, G. A. Chandler, D. K. Derzon, R. J. Dukart, D. L. Fehl, D. J. Johnson, E. J. McGuire, A. R. Moats, D. D. Noack, C. L. Ruiz

Sandia National Laboratories
P.O. Box 5800
Albuquerque, NM 87185-1196

T. L. Barber
K-tech Corporation
Albuquerque, NM 87185-1196

Abstract

We performed a series of experiments on the Particle Beam Fusion Accelerator II (PBFA II) in May, 1994, and obtained a brightness temperature of 61 ± 2 eV for an ion-beam heated hohlraum. The hohlraum was a 4-mm-diameter, right-circular cylinder with a 1.5-mm-thick gold wall, a low-density CH foam fill, and a 1.5- or 3-mm-diameter diag-nostic aperture in the top. The nominal parameters of the radially-incident PBFA II Li ion beam were 9 MeV peak energy (~10 MeV at the gas cell) at the target at a peak power of 2.1 $\pm$ 0.3 TW/cm^2 and a 15 ns pulse width. Azimuthal variations in intensity of a factor of 3, with respect to the mean, were observed. Nonuniformities in thermal x-ray emission across the area of the diagnostic hole were also observed. Time-dependent hole-closure velocities were measured: the time-averaged velocity of ~2 cm/μs is in good agreement with sound speed estimates. Unfolded x-ray spectra and brightness temperatures as a function of time are reported and compared to simulations. Hole closure corrections are discussed with comparisons between XRD and bolometer measurements. Temperature scaling with power on target is also presented.

Intentionally Left Blank

Contents

Intentionally Left Blank

Cylindrical Target Li-beam-Driven Hohlraum Experiments

1. Acknowledgements

We would like to thank our management (Don Cook, Ray Leeper, Keith Matzen, Tom Mehlhorn, and Jeff Quintenz) as well as the rest of the staff of the ion beam program at Sandia National Laboratories for their guidance and assistance. In addition, we acknowledge and thank all of those who provided the excellent support at the PBFA-II facility.

Intentionally Left Blank

2. Introduction and Goals - M. S. Derzon

Light ion beams are being developed as a potential driver for the national Inertial Confinement Fusion (ICF) program on the Particle Beam Fusion Accelerator II (PBFA II) at Sandia National Laboratories.[1] The long-term goal of ICF is to compress a fuel capsule to ignition and gain. In indirect-drive ICF, a thermal x-ray source is used to compress a fuel capsule along a low temperature adiabat to ignition and gain. In light ion-beam-driven ICF the target consists of a foam-filled high-Z radiation case (called a hohlraum) and a fuel capsule. The hohlraum converts the incident ion-beam energy into a uniform thermal x-ray source by stopping the ions in the low-density foam and confining the radiation field in the high-Z case. In a prior publication we demonstrated the formation of a hohlraum with an ion beam in a conical target geometry.[2] In this report we describe a series of experiments in which we investigated the thermal scaling and the effects of the closure of a diagnostic aperture.

The ion beam deposited roughly 800-1400 TW/g within the foam volume. This is comparable to that required in the foot pulse, the low-power early time heating prior to the final high-power drive, of a high gain target. Pulse width is shorter and beam voltage is much lower than required for high gain.

There were five primary goals to the experiment: (1) to understand and measure the beam properties, (2) to achieve 70 eV brightness temperature, (3) to quantify hole closure, (4) to scale hohlraum temperature with ion beam intensity in this geometry, and (5) to compare with the experiments in conical geometry.

We report new diagnostic capabilities for both beam characterization and thermal emission. These include the ability to obtain absolute beam intensity near the target at 2 TW/cm^2 with inner-shell x-ray measurements and aperture closure velocities as low as 2 cm/μs. Several diagnostics were used to measure properties of the thermal radiation from the target. Time-integrated cameras were used for high-resolution imaging of the thermal x-ray source. Two bolometers were used to estimate the total soft x-ray emission. XRDs were used to estimate the brightness temperature and were compared to the temperature estimated with the bolometers. A broadband energy-resolved, one-dimensional spatially-resolved, and time-resolved diagnostic observed hydrodynamic motion.

This paper is meant to serve as a reference for the work performed on the 1994 Li beam target experiments. The analysis continues, but at the time of this writing most of it is complete. This document highlights the important lessons learned and serves as an archive of the work performed. The document includes descriptions of target fabrication, diagnostics development, and pertinent physical interpretation of the measurements. Some of these results have been published already.[2,3]

References

[1] J. P. VanDevender and D. L. Cook, Science **232**, 831 (1986).

[2] M. S. Derzon, et al., Phys. Rev. Lett. **76**, No. 3, 435(1996).

[3] A. B. Filuk, et al., International Atomic Energy Agency (IAEA) technical committee meeting on drivers for inertial confinement fusion, Paris (France), Conf. date 14-18, Nov 1994, ISBN: 2-7272-0178-8, Publ. date May 1995, p 233-241, (408 p).

3. Diagnosing Lithium Beam Focus Intensity on PBFA II - D. J. Johnson

A determination of the beam characteristics for the lithium beam focus on the target series was obtained from shots 6472 and 6476, which were fired prior to the target series. The results for shot 6472 will be presented here and are similar to those for shot 6476. The results from a number of earlier shots with the same geometry will be included in the discussion. These shots and the target shots used a compound anode curve shape defined by $bz+cz^2+fz^5$, where b, c, and f are 0.064 radians/cm, -0.015 radians/cm^2 and -1.0 e^{-4} radians/cm^5, respectively. The anode shape, designated b64, had a radius of curvature ~15.6 cm in the axial direction, compensated for applied- and self -magnetic field bending to give a good vertical focus (see Chapter 8 by Moats for a quantitative estimate of the focus on the thermal targets). The lithium beam undergoes charge-exchange at the gas cell window and therefore must have a non-zero anode stream function $\psi_a = qA\theta = (q_a-q_{gc})/(q_a \psi_{gc})$ to achieve an on-axis focus for no energy loss or scattering in the gas cell. Here, ψ_{gc} is the gas cell stream function and q_a and q_{gc} are the charge of the beam ions in the anode-cathode gap and gas cell. On-axis focus was achieved by adjusting the coil currents, placing the zero stream function (separatrix between the anode and cathode fields) approximately 2 cm from the anode surface, and using a "V"-shaped gas cell. The layout of the anode, gas cell, and separatrix are shown in Figure 1 along with lithium orbit calculations obtained from the TRIDIF[1] magnetic diffusion field solver code. This arrangement gave a good vertical focus (which dis-agrees with Moats, who interprets a large vertical focus, this report), and minimized horizontal focus broadening due to variations in canonical angular momentum of the beam.

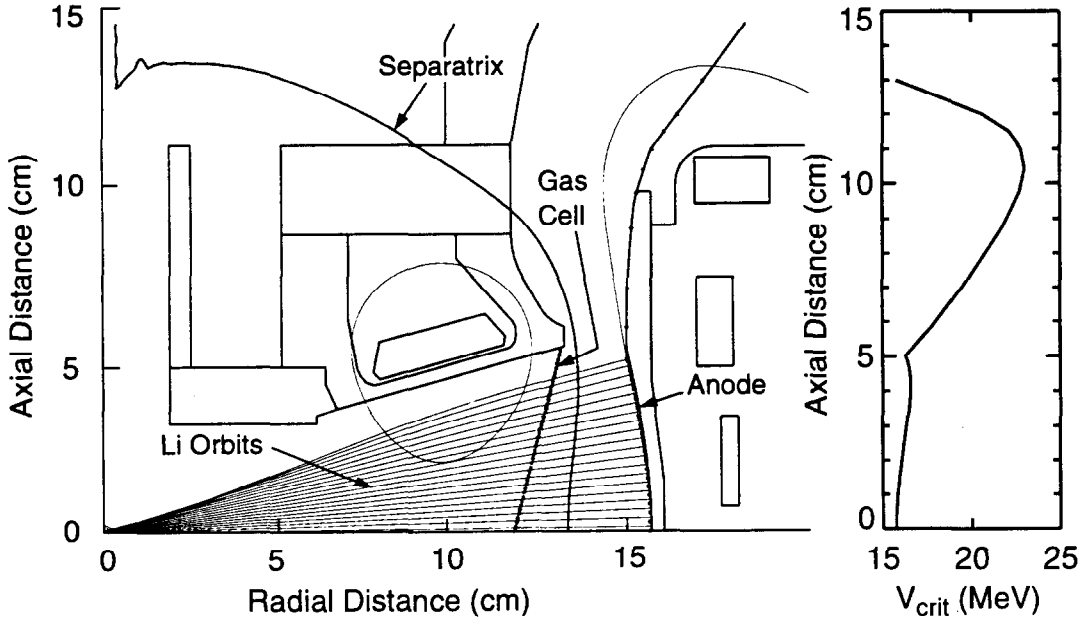

Figure 1. A TRIDIF plot of the diode geometry, applied B-field, and lithium ion trajectories.

The time-resolved focus intensity of the lithium beam on PBFA II was determined from ions Rutherford-scattered from a planar gold target, located at the center of the diode, and oriented at 45° to the centerline. A 64° azimuthal sector of the beam, set by an aperture at 1.2 cm radius, was focused on the target for these measurements. The scattered ions were detected with a spatially-imaging spectrometer[2], a time-resolved ion-pinhole camera (MOCAM[3]), and a multiple- filtered six-frame ion-pinhole camera (IPC[4]). The analysis of the data from each diagnostic requires an accurate knowledge of the beam energy (voltage) striking the target. Since the beam has an energy-momentum correlation (E-cP) caused by the ion mode instability[5] in the accelerating gap, it is necessary to measure the beam voltage as a function of time and distance from the center line of the diode. The E-cP correlation causes the beam voltage to be higher on the right side of the center line than on the left. Therefore the focus is determined by a convolution of the initial source divergence and differing times of flight from the anode to the target. The additional time of flight to the diagnostics further distorts the detected images of the beam. The analysis and the data will be presented at the time of acceleration (anode time), time of incidence to the target, or detected time.

The initial step in analyzing the beam on PBFA II was to obtain the accelerated lithium beam voltage versus time and emission angle. These measurements were made with a spatially-imaging magnetic spectrometer, which is shown schematically in Figure 2. Lithium ions were detected with solid state p-i-n diodes and CR39 track recording film. A 1.25-mm-diameter pinhole was located 58.5 mm from the 0.5-μm-thick gold scattering target and gave a demagnification of 2.1 at the detection surface. A 4.5-mm-wide slit allowed a 5.7-mm-tall region of the target to be imaged on the CR39 track recording film. The film had holes drilled at the p-i-n locations to allow passage of the lithium ions. The p-i-n's allowed for time-resolved measurement of the beam voltage at the center line of the diode and at a nominal ± 4.6 mm from the center line. The line of sight of the off-axis rows varied from 4.5 to 4.7 mm as the beam energy dropped from 10 to 5 MeV because of the dependence of the spectrometer magnification on detected ion energy. The p-i-n's observed lithium ions at discrete energies depending on the deflection angle, which ranged from 30 to 56° depending on the p-i-n location, and on the final charge state, which was typically Li^{+3} early and Li^{+2} late in the pulse. Other ions such as carbon contributed less than 1% to the signals.

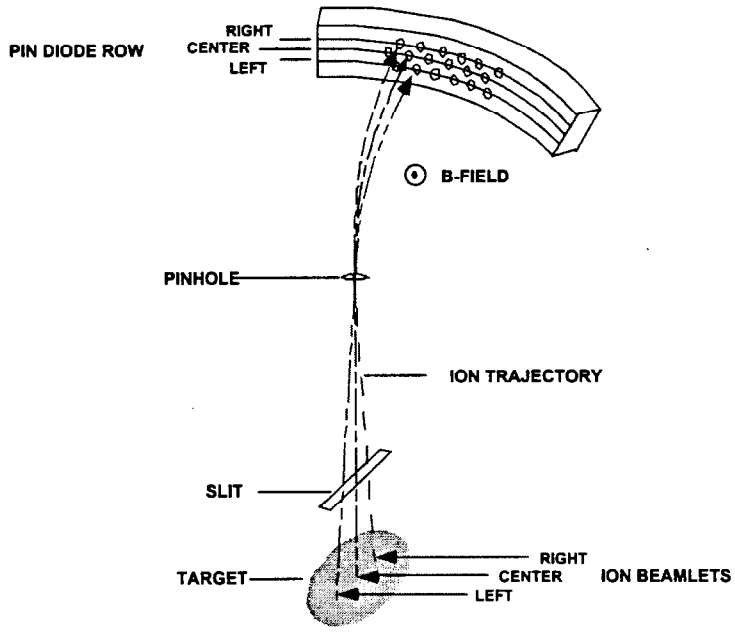

Figure 2. Artist's conception of the magnetic spectrometer.

The analysis of the spectrometer data began with the time synchronization of the p-i-n signals using the bremsstrahlung pulses from electron losses in the magnetically insulated transmission line feed before the ion diode began to produce a lithium beam. This generally involved shifting a few of the 30 signals by $\leq$1 ns. The signals were next time shifted to the anode time reference based on the time of flight as calculated with the SPU magnetic spectrometer unfold code.[6] Then, the Li^6 signal from the leading edge of each p-i-n signal was removed. This signal was nominally 7.5% of the Li^7 signal, as expected for the isotopic abundance ratio. The 2° spacing of the p-i-ns in the magnetic spectrometer facilitated this removal because the Li^6 was bent ~2° more than the Li^7. Calculations by the SPU code showed that the Li^7 energy of the pins agreed with the Li^6 energy of the p-i-n signal at 2° larger angle to within ± 50 keV. The removal of the Li^6 signal therefore consisted of multiplying the signal from PIN(θ - 2) by 0.075, correcting for the differences in Li^6 and Li^7 time of flight, and subtracting this from the signal from PIN(θ).

The lithium current density/beam energy versus beam energy and time, J/E(E,t), were then generated as shown in Figure 3 for shot 6379. This was done by dividing the p-i-n signals by the response functions for Li^7 detected by PIN(θ) in the +3 charge state. If +2 charge state Li^7 signals were available, the same procedure was followed to allow measurements at lower beam energies. The response functions allowed for the dispersion of the spectrometer, the Rutherford scattering probability, and the fraction of the lithium energy deposited in the active volume of the p-i-ns. The current densities at energies between the energy points defined by the p-i-n locations in the spectrometer were obtained by interpolation. This procedure was performed in 1 ns steps from the beginning of the lithium pulse.

Contours plots of the current density/energy value, such as the representative plot shown in Figure 3 for shot 6379, allowed identification of experimental errors in the data. This was necessary because at least one spurious signal was detected on nearly all shots. The errors were attributed to cable, attenuator, or oscilloscope problems. These errors were corrected by referencing signals from adjacent energy p-i-n's and the lithium tracks in the CR39 near p-i-ns with problem signals. The mean beam energy was taken to be the energy at the half value of the integral of the current density curves over beam energy.

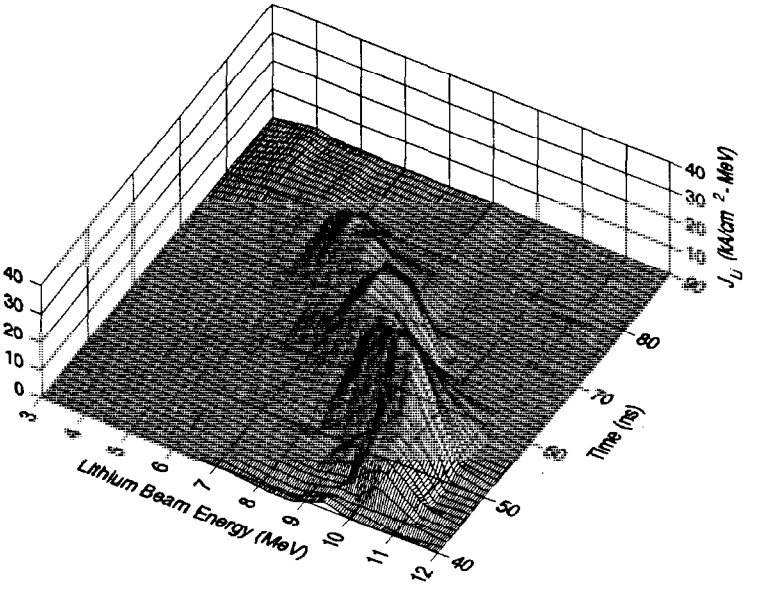

Figure 3. Contours of target current density versus time.

The energies determined by the unfold of the p-i-n signals from the three rows of the magnetic spectrometer for shot 6472 are shown in Figure 4. The absolute current densities measured by the three rows were obtained by normalizing the integrals over energy to the current densities obtained from the movie camera data on the 5800 series shots and were checked by forward simulation of the signals on a number of shots. The current densities determined with the spectrometer for shot 6472 are shown in Figure 5 together with the values determined with the movie camera, as described later in this section. The focused beam power density at the target calculated from the current density and beam voltage at the target, allowing for time of flight and energy loss in the gas cell window. The focused power was the product of the current density and beam energy at the target.

This analysis was augmented by performing forward simulations of the p-i-n signals using the unfolded voltages and trial current densities. These calculations were made on an absolute basis from the spectrometer and target geometry. The input current and voltage pulses were divided into 0.1 ns time steps with 9 voltage bins at each step to allow for a Gaussian energy spread. The spread was taken to be 1-MV FWHM to allow for ~ 0.8 MV spread from the target and some additional spread from the beam itself. The Rutherford scattering cross section was increased by 13% to allow for the spread in the angle of incidence caused by the 64° sector of the beam observed. This factor was determined with a computer program that calculated the increase in scattered ions caused by a beam with ±32° horizontal and ±15° vertical spread incident upon the target. The energy at which the ions Rutherford scattered was taken to be the lithium energy incident upon the target minus half of the dE/dx energy loss for a lithium ion penetrating the target.

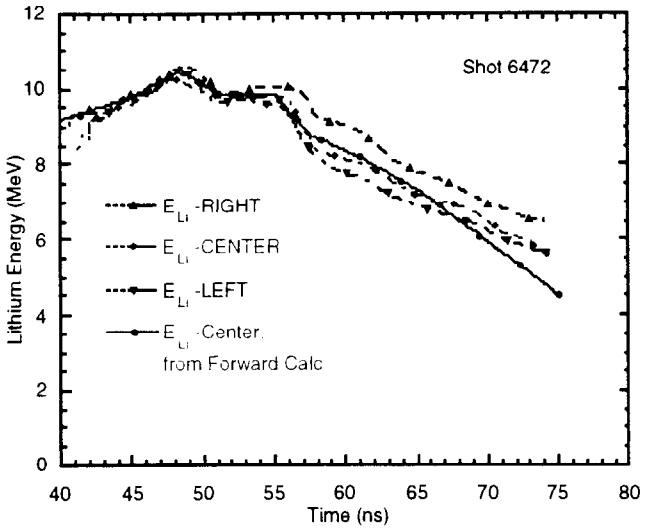

Figure 4. Lithium beam energy (voltage) for shot 6472 displayed at the time of acceleration. The dotted curves were obtained with reverse unfolds of the three rows of magnetic spectrometer p-i-n signals. The bold curve was obtained from a forward simulation of the p-i-n signals and is more accurate for times after 65 ns.

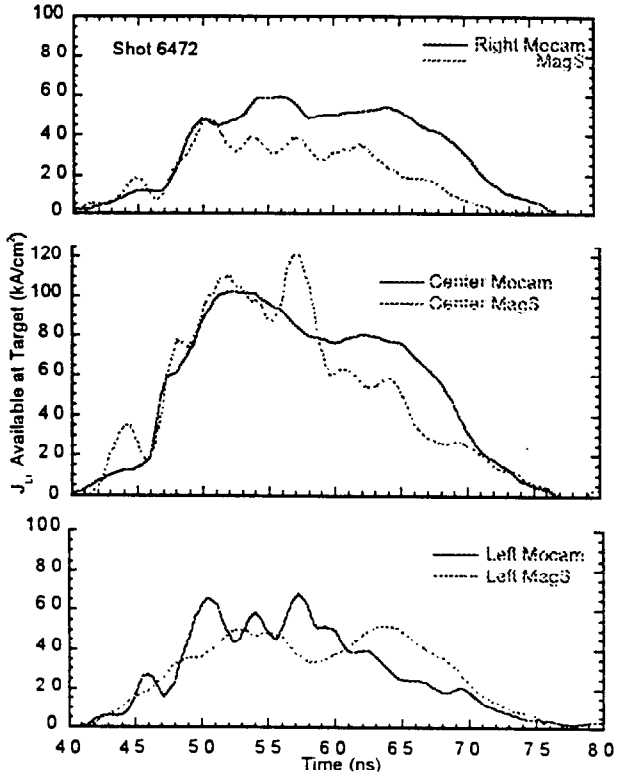

Figure 5. Lithium current densities from the spectrometer and ion movie camera for shot 6472 displayed at the time of acceleration.

The deposited energy was determined from the spectrometer-measured beam voltages allowing for energy loss in the gas cell, target, and p-i-n dead layer.

The target thickness was increased by 8% to allow for the spread in angles of incidence of the beam. The energies deposited in the p-i-n's were converted to signals, $S(t,\theta)$, with 0.5 ns and 0.5° steps, assuming one electron-hole pair/3.61 eV of deposited energy. The spectometer p-i-n signals, $S(t,\theta_{ms})$, were obtained by integrating the product of $S(t,\theta)$ and the angular response function $F(\theta - \theta_{ms})$, over θ. The function $F(\theta - \theta_{ms})$ is the angular spread of the beam at the p-i-n's due to the spectrometer and p-i-n diode apertures. This was determined from the geometry to be 1.1° FWHM with an approximately Gaussian shape. The simulated and experimental p-i-n signals for shot 6472 are shown in Figure 6 as continuous and dotted curves, respectively. The +3 and +2 exit charge states of the detected ions are labeled above the signal for the 30° p-i-n signal. The Li^6 and Li^7 components of the beam are labeled below the signal from the 44° p-i-n. These calculations gave current densities that agreed to the unfold values within ± 10%

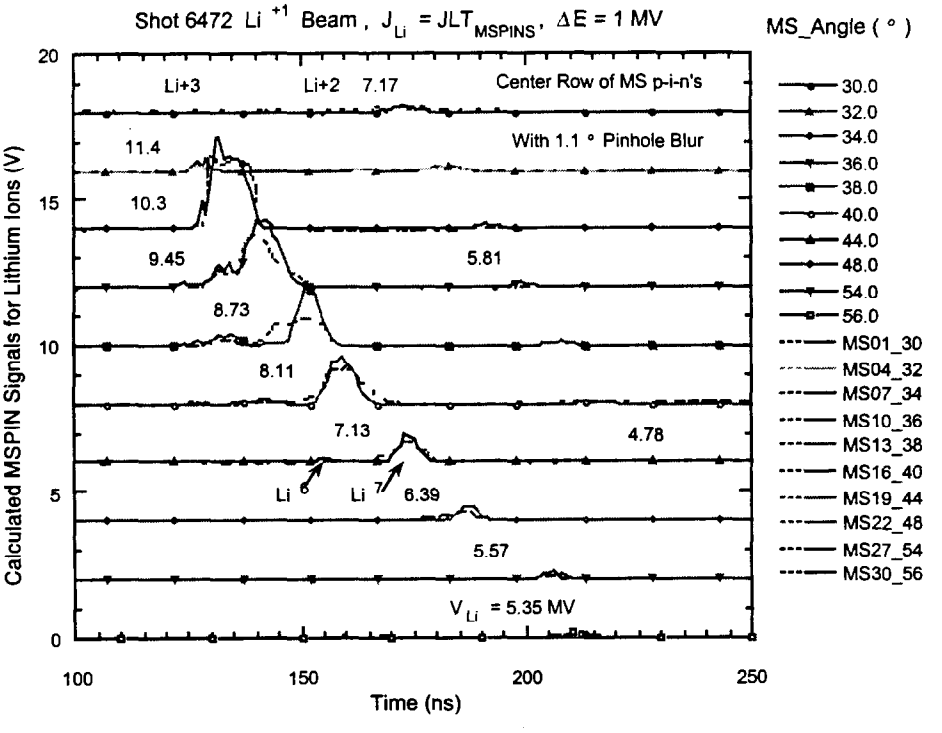

Figure 6. Calculated and experimental spectrometer signals for shot 6472. The calculated signals are labeled on the right by spectrometer observation angle and plotted as continuous curves. The experimental signals are labeled as MS##_ θ where ## is p-i-n number and θ is detection angle. The signals are offset by 2 volts to allow separation of the signals. The lithium beam voltage at the diode, V_{Li}, is indicated for a number of pulses in megavolts. The energy spread for the calculations was Gaussian with 1-MV FWHM.

and allowed a determination of the beam voltage about 2 MeV lower than could be obtained by the unfold method. The input beam voltage history for shot 6472 is shown in Figure 4. The voltage is believed to be more accurate than E_{Li}-Center after 65 ns because the determination of the voltage at late time from the forward simulation relies primarily on the timing of the very small signals of the spectrometer p-i-n's detecting lithium in the +2 charge state. The reverse simulation is apparently giving a voltage that is too large because the larger signals (due to increase sensitivity at higher lithium energy) above the mean voltage are more susceptible to spurious response tails.

Forward simulations of the spectrometer CR39 tracks/angle were also made to obtain the beam energy within the spectrometer field of view on the target defined by the CR39. The input voltage to this calculation was a voltage pulse referenced to the horizontal focus location noted on the CR39 and generally similar to the voltage pulse unfolded from the p-i-n row nearest the center of the beam. The input current was the beam current within the 5.7-mm-tall by 19-mm-wide target field of view. A good fit to the three charge states of lithium detected by the CR39 defined the mean voltage of the beam versus time and gave the specific beam energy on target. This diagnostic gave the most accurate measurement of the energy on the PBFA II target because of the transmission mounted target, simple geometry, and lack of filter foils or active detectors. The lithium beam energy deposited viewed were 11.5, 8.4, and 9.2 kJ for shots 5851, 6472, and 6476. The beam power density was estimated by converting the current on target to current density by dividing by the 5.7-mm-tall vertical field of view and horizontal FWHM obtained from the spectrometer or MOCAM. The factor $(\pi/4\ln 2)^{1/2}$ was included to convert to peak current density for a Gaussian horizontal beam profile. The beam energy on target was obtained also with the 6 frame ion pinhole camera (IPC). The IPC observed the beam in reflections and was filtered to allow energy measurement cuts between 4.3, 5.9, 7.3, 8.6, 9.7, and 11.6 MeV and above 11.6 MeV. The energies obtained with this camera could be compared to the values obtained with the magnetic spectrometer by including CR39 tracks within the same target field of view as the spectrometer. Power densities were obtained by allowing for the vertical and horizontal FWHM determined from the beam profiles. These measurements were prone to larger errors than the spectrometer measurements because, in reflection scattering geometry, the sensitivity to scattering angle varied by ~ 4 for beam initiating from the top and bottom of the anode.

The focal power on target was obtained also with the ion MOCAM, which is shown schematically in Figure 7. This device used a 0.7-mm-diameter pinhole located 13.2 cm from the target. The ions were detected with an array of 27 p-i-n diodes located 26.1 cm beyond the pinhole, where the scattered ion image was demagnified by 2 and the p-i-n's observed locations on the target separated by 2 mm. The beam energy histories determined from the spectrometer were used to calculate the energy of the ions incident upon the p-i-n's versus time. The deposited energy was determined from the spectrometer-measured beam voltages, allowing for energy loss in the gas cell, target, and p-i-n dead layer. The lithium voltage history for the center p-i-n, MC25, is shown in Figure 8 along with the p-i-n signal. The p-i-n signals were converted to detected ion rate

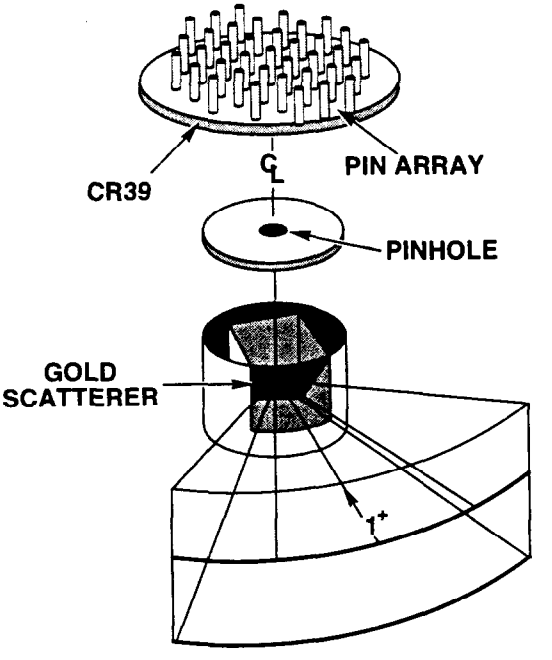

Figure 7. Artist's conception of the ion movie camera.

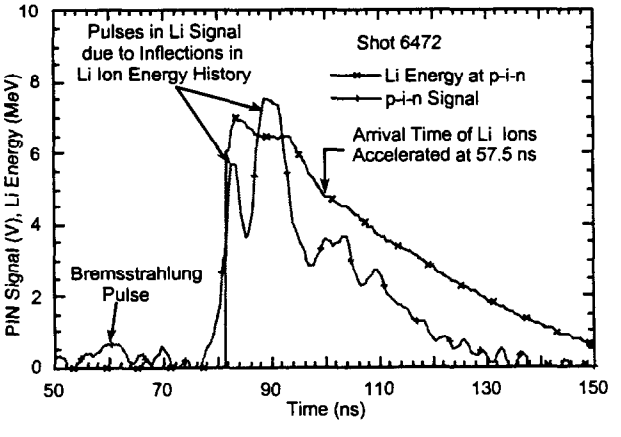

Figure 8. Lithium beam voltage history that arrives at the center MOCAM p-i-n and corresponding p-i-n signal for shot 6472. The arrival time of lithium ions accelerated at 57.5 ns is shown at 100 ns.

assuming one electron-hole pair/3.61 eV of deposited energy. The ion current density scattered from the target was determined from the detected ion rate via the p-i-n diode active area, solid angle of the pinhole, and camera magnification. The current density on a hypothetical target at the anode was determined from the classical Rutherford scattering probability in the same manner as the forward simulation of the spectrometer p-i-n's described above. The current density was then shifted back in time to the anode time reference based upon the lithium velocities before and after the target position.

The beam voltage history for the center p-i-n in the movie camera was taken from the center row of the magnetic spectrometer. The p-i-n's observing the focus at ≥4 mm to the left of center were given the beam voltage history measured by left row and those observing ≥4 mm to the right of the center were given the history measured by the right row. The voltages from the spectrometer rows bracketing the 2 mm positions were averaged to obtain voltages for the movie camera p-i-n's observing the focus 2 mm from the center line. The lithium current densities calculated from the three movie camera p-i-n's which observed the target near the positions viewed by the spectrometer are shown in Figure 4, referenced to the anode time base. The focused power densities at the on-axis target are shown in Figure 9 for shot 6472. These data are typical of the average values obtained on about 10 similar geometry shots. A number of shots showed higher focused power densities. This is attributed to a higher than average anode current from the 64° azimuthal beam sector observed by the on-axis gold target on these shots. Shot 5851 gave the highest power density of these shots and was ~ 30% above the mean value. The results from this shot are shown in Figure 10.

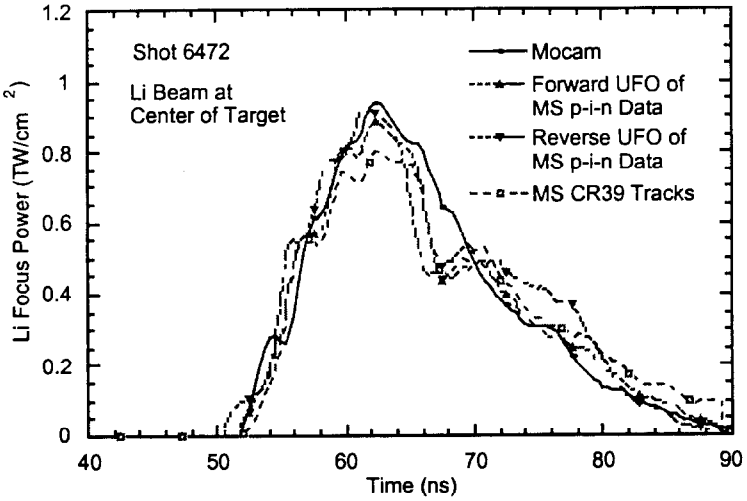

Figure 9. Focused power density for shot 6472.

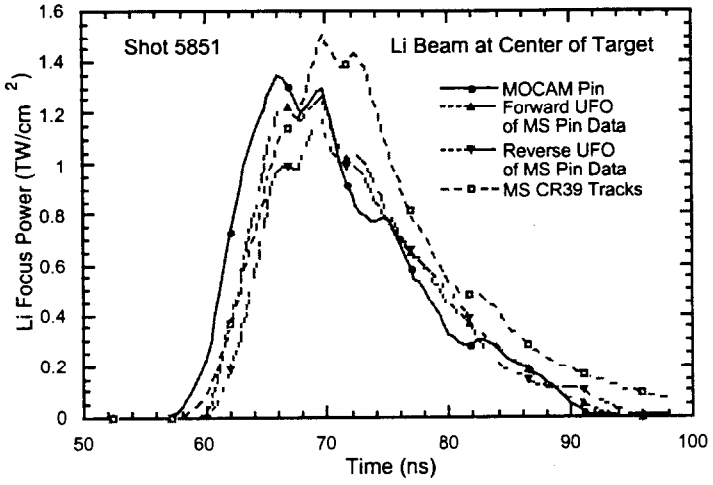

Figure 10. Focused power density for shot 5851.

References

[1] J. R. Freeman, J. Comput. Phys. 41, 142 (1981).
[2] R. J. Leeper, W. A. Stygar, R. P. Kensek, J. R. Lee, D. J. Johnson, T. R. Lockner, J. E. Maenchen, D. E. Hebron, and D. Wenger, Rev. Sci. Instrum. 59, 8 (1988).
[3] W. A. Stygar, L.P. Mix, R. J. Leeper, J. E. Maenchen, D. F. Wenger, C. R. Mattson, and D. J. Muron, Rev. Sci. Instrum. 59, 1860 (1988).
[4] W. A. Stygar, R. J. Leeper, L. P. Mix, E. R. Brock, J. E. Bailey, D. E. Hebron, D. J. Johnson, T. R. Lockner, and P. Reyes, Rev. Sci. Instrum. 59, 1865 (1988).
[5] J. P. Quintenz, M. P. Desjarlais, T. D. Pointon, S. A. Slutz, D. B. Seidel, T. A. Mehlhorn, R. S. Coats, M. L. Kiefer, N. A. Krall, and L. D. Bacon, Proc. IEEE 80, 971(1992).
[6] Private communications, J. E. Maenchen.

Intentionally Left Blank

4. Intensity Scaling on Different Geometric Targets - T. A. Haill

Several target geometries have been fielded on PBFA II. To compare the results for these different targets, how beam intensity scales on flat, spherical, and cylindrical targets must be understood so that accurate comparisons can be made between experimental temperature - intensity data and the radiation/hydrodynamic calculations.

A generalized formula for the beam intensity I on the PBFA II target is

$$I = \frac{P}{A}\eta F \tag{1}$$

where A is an appropriate target area, P is the diode power, and F is a beam focusing factor. The factor $\eta = \eta_v\, \eta_i\, \eta_s\, \eta_t$ is an overall efficiency that includes the beam-voltage to diode-voltage ratio η_v, the ion-efficiency η_i, source purity η_s, and the beam-transport efficiency η_t.[1] The following analysis does not take into account that η is known to be non-uniform in θ and z. It is assumed that the beam power per unit anode emission area is a two-dimensional Gaussian in y (the horizontal divergence) and z (the vertical divergence) on any target. Previous diagnostic data on PBFA-II shots (e.g., ion-pinhole-camera and ion-movie camera beam profiles[2]) have shown an approximately Gaussian beam on target. It is also assumed that the target, as viewed from a point on the anode, is a circular disk (for the spherical and flat-foil targets) or a rectangular area (for the cylindrical target) and that the fraction of the power on the target emitted from an infinitesimal area centered at the point is the integral of the Gaussian over the disk (or the rectangular area, as appropriate for the target geometry). The power balance formulas for the intensity on a sphere, cylinder, and foil may be written, respectively, as:[3]

$$I_{sphere} = \frac{f\,P}{4\pi r^2}\left[1 - 2^{-(r/b)^2}\right] \tag{2}$$

$$I_{cylinder} = \frac{f\,P}{(2\pi r)(2h)}\left[\mathrm{erf}\left(\frac{r\sqrt{\ln 2}}{b}\right)\right]^2 \tag{3}$$

$$I_{foil} = \frac{f\,P}{\pi r^2}\left[1 - 2^{-(r/b)^2}\right] \tag{4}$$

where r = target radius, h = cylindrical-target half-height, b = beam HWHM, and f = fraction of power passing through the target holder aperture. For the cylindrical hohlraum experiments and the spherical target calculations, we assume $f = 1$. Actually, as much as 20% of the incoming ion beam is blocked by nuclear diagnostic targets, target-holder posts, and other hardware fielded on all shots. But for the ratios we derive here, these "beam-blocks" can be folded into the overall efficiency. Furthermore, for these ratios, the efficiency factor cancels out and can be suppressed. For the flat-foil experiments used for cross-calibration of the absolute intensities (see Moats, Chapter 8), the target holder only allowed beam from a 60° sector to hit the target. The treatment of

the power on target as an energy flux, a vector quantity, is ignored and the integral is calculated as a surface integral. The cylinder half-height h is assumed to be equal to the cylinder radius r, the cylinder end-walls are not illuminated, and beam offsets are ignored. The factor f is ~ 1/6 for the 60° sector.

These formulas may be used to scale intensities between targets of different size and different geometries. For example, consider targets of equal radii and a sub-area of the foil of this same radius. The ratio of the cylindrical to spherical intensity is

$$\frac{I_{cylinder}}{I_{sphere}} = \frac{[\mathrm{erf}(\frac{r\sqrt{\ln 2}}{b})]^2}{[1-2^{-(r/b)^2}]} \cong \frac{4}{\pi} \quad when \ \frac{r}{b} << 1 \tag{5}$$

The ratio of the spherical to the foil intensity is

$$\frac{I_{sphere}}{I_{foil}} = \frac{1}{4f} \cong \frac{3}{2} \tag{6}$$

The ratio of the cylindrical to the foil intensity is

$$\frac{I_{cylinder}}{I_{foil}} = \frac{\frac{1}{4}[\mathrm{erf}(\frac{r\sqrt{\ln 2}}{b})]^2}{f[1-2^{-(r/b)^2}]} \cong \frac{6}{\pi} \quad when \ \frac{r}{b} << 1 \ and \ f = 1/6 \tag{7}$$

These analytic scalings agree well with results from a particle-in-cell code (SOPHIA) developed at Sandia National Laboratories according to the simulation of PBFA-II shot 6466 from the Power Coupling Series of June 1994. This shot is from the same series in which titanium strips in front of the flat gold foil were fielded to cross calibrate between beam intensity diagnostics. (See Figure 7 in Chapter 8).

Intensity calculations among different target geometries, but similar radii, were executed using the SOPHIA code. The comparison between the SOPHIA simulations of PBFA-II shot 6466 from the Power Coupling Series (executed immediately prior to the cylindrical target series) and the analytic theory are given in Table 1. These results verify the scaling of (EQ 2) to (EQ 4). Note that SOPHIA actually tallies the foil intensity on a target sub-area that is coincident with the scattering foil tlted at 45°. SOPHIA's foil intensity must therefore be scaled up by a factor of $\sqrt{2}$ to compare with the foil intensity perpendicular to the beam described in (EQ 4), thus the factor of 3/2 shown in (EQ 6) needs to be $\frac{3}{2}\sqrt{2} = 2.12$.

Table 1. Comparison of Intensity on Target.

Ratio	Theory	Simulation
6 mm cylinder to 6 mm sphere	1.27	1.29
5 mm cylinder to 5 mm sphere	1.27	1.32
4 mm cylinder to 4 mm sphere	1.27	1.31
6 mm sphere to 6 mm foil (scaled by $\sqrt{2}$)	2.12	2.00

In addition, the SOPHIA-simulated results of the magnetic spectrometer, CR39 image, total track profile, and FWHM beam profile compare favorably with the experimental results obtained on PBFA-II shot 6466.

Scaling the Sophia tally of the intensity on a 6-mm-diameter area of the target by $\sqrt{2}$ yields a spatially-averaged intensity of 1.04 TW/cm^2. Using magnetic spectrometer data from that shot,[4] a spatially-peaked intensity of 1.23 to 1.44 TW/cm^2 is obtained. These values differ by 18 to 38%. The intensity for Shot 6466 is uniquely high for this shot series. The five other shots in this series have tabulated intensities of 0.75 to 1.1 TW/cm^2. Thus, the SOPHIA tallied intensity is a reasonable value and is well within the range of azimuthal intensity variation that are seen on the "Titanium Bird Cage."

In summary, a scaling for targets of different geometries and sizes has been developed. In particular the scaling of flat foil intensities to spherical and cylindrical targets should be approximately, 1.5 and 1.9, respectively.

References

[1] W. A. Stygar, 1990, "A Simple - but Useful - Power-Conservation Equation For Ion Beam Experiments," memo of October 12, 1990.

[2] R. J. Leeper, et al., Rev. Sci. Instrum. 59, 1860(1988).

[3] T. A. Haill, "Extension of Power Balance Formulas to Include Beam Offsets," memo of February 9, 1994.

[4] D. J. Johnson, private communication, 1994.

Intentionally Left Blank

5. Radiation/Hydrodynamic Simulations of Cylindrical Hohlraums - R. J. Dukart

1- and 2-D simulations of a Li-ion-beam driven hohlraum

We have done a series of 1- and 2-D radiation/hydrodynamic simulations for pre-shot, design, and characterization of our ion-beam-driven hohlraum for PBFA II experiments. 1-D simulations were performed in spherical geometry and used to determine an optimum target configuration, e.g., material thicknesses and foam densities. 2-D simulations were performed for hohlraums, with and without radiation losses out a diagnostic aperture, for target performance scaling. Simulations were performed with a fully zoned diagnostic aperture to understand aperture motion and its effect on hohlraum performance.

For 2-D simulations the hohlraum was a 4-mm diameter, 4-mm high cylinder. The cylindrical wall was 1.5 μm of gold overlaid with a layer of 3.0-μm parylene-D ($C_2H_6Cl_2$). The top and bottom wall thickness in the 2-D simulations was 10 μm gold. The hohlraum was filled with 5-mg/cm^3 TPX (CH) foam. Radiation transport in the foam was treated with diffusion, corrected for the geometric mean free path. All materials were treated in local thermodynamic equilibrium (LTE), since their densities are expected to remain relatively high at moderate temperatures. In order to understand hohlraum performance with diagnostic apertures, some of the 2-D calculations simulated the effect of radiation losses out a diagnostic aperture but did not include any hydrodynamic motion of the aperture.

Hohlraum performance can be characterized by the radiation temperature achieved as a function of ion beam power or ion beam intensity. The former lends itself to direct comparison of targets with differing geometries, whereas the latter allows a comparison of performance with back-of-the-envelope and simple analytic modeling.

The ion beam model used in the simulations (Figure 1) was an 8-mm FWHM Gaussian beam with a 25-mrad divergence from a source 15.5 cm from the target axis. This waveform was derived from PBFA II shot 5721 by David

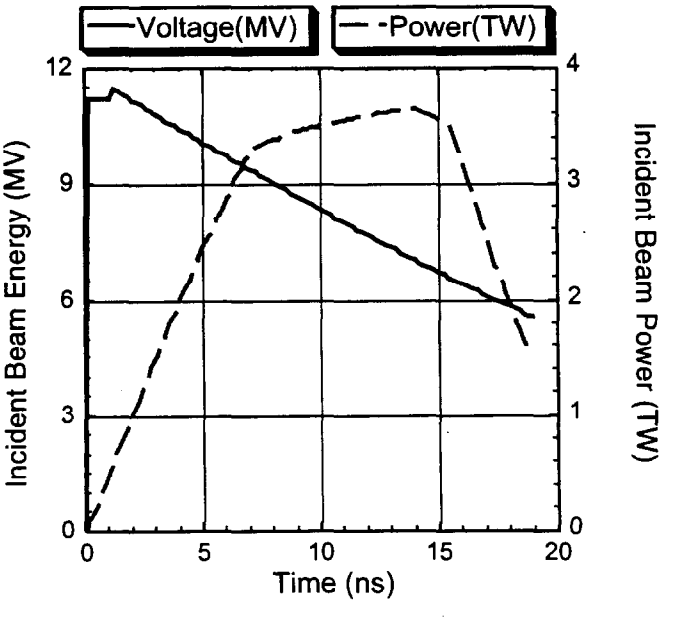

Figure 1. The Li-ion beam voltage and power used in the simulation.

J. Johnson, a waveform deemed adequate for hohlraum design and scaling. This shot was used because it was the best shot (highest power) at the time of the modeling.

For hohlraum scaling, we must be clear which temperature and which beam power or beam intensity we use. In the 2-D simulations, we can define the average radiation temperature achieved as (1) that of the inner surface of the hohlraum wall ($<T_r>$), (2) as the average radiation temperature of the hohlraum rear wall observed by the x-ray diagnostics ($<T_{r,w}>$), or (3) as the brightness temperature calculated from the radiation flux emitted out a diagnostic aperture (T_b). The average wall temperature, $<T_r>$, corresponds to the environment viewed by a capsule inside of a hohlraum. $<T_{r,w}>$ is the temperature of the rear wall viewed through the diagnostic aperture. The brightness temperature, T_b, corresponds to the temperature determined by diagnostics that measure flux emitted from the hohlraum interior. The average wall temperature can be a few eV higher than the rear wall temperature since the ion beam contributes to the heating of the cylindrical side walls but not the rear wall. The brightness temperature can also be higher than the wall temperature since the emitted flux includes radiation from the hohlraum walls and the foam fill.

In Figure 2, hohlraum scaling is presented as a function of total lithium-ion beam power emitted by the ion diode for cylindrical hohlraums with 1.5- and 3.0-mm-diameter diagnostic apertures. For these simulations, the aperture was modeled in the code as a loss of energy at a rate corresponding to the flux incident on the inner hohlraum wall times the area of the corresponding aperture.

We can also view the hohlraum performance as a function of the peak Li-ion-beam intensity incident on the target, as shown in Figure 3. We define this intensity to be the peak ion beam power absorbed by the target divided by the cylindrical wall area over which the beam is incident.

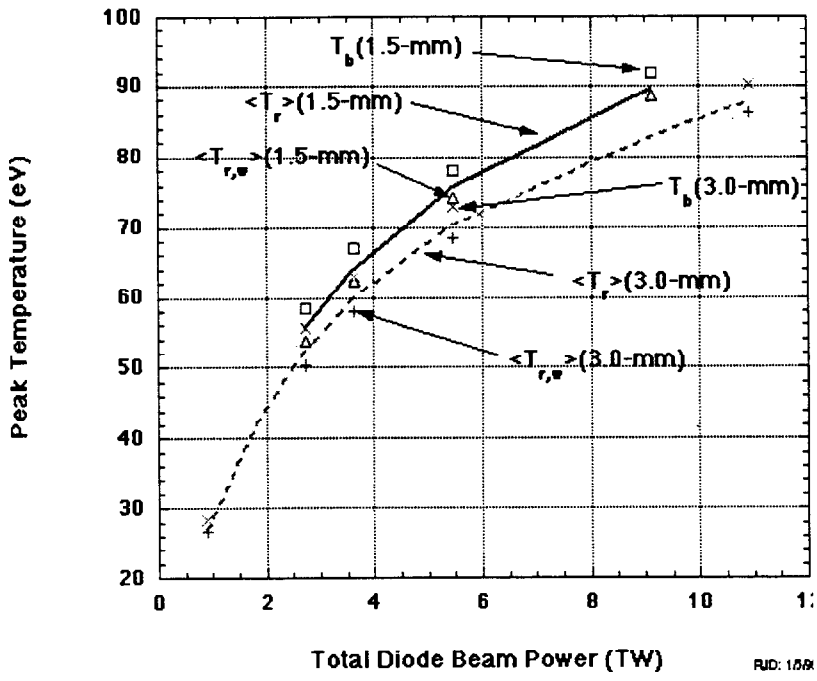

Figure 2. Hohlraum temperature scaling with total ion beam power.

The brightness temperature predicted here is higher than observed in the experiments for the same beam power. The ion beam accelerating voltage in the experiments was found to be lower than that assumed in these pre-shot calculations and the shot 5721.

2-D simulations with a real aperture.

We performed a series of 2-D radiation/ hydrodynamic simulations to study the response of the diagnostic aperture during the experiments. The diagnostic aperture was zoned to allow it to freely expand and the top end of the hohlraum was protected from the ion beam by a thick gold beam block, simulating the hohlraum configuration in the experiment.

The ion beam model in the simulations (Figure 1) was the same as that described above. We assumed an ion diode that generated a peak power of 3.6 TW, beam which then deposited 0.96 TW peak power in the hohlraum. The simulations terminated at 18.9 ns (about 3-ns past peak hohlraum radiation temperature), depositing 16.2 kJ in the target (3.6 kJ in the foam, 6.8 kJ in the wall, 3.8 kJ in the beam block, and the remaining 2 kJ in the parylene-D).

The peak radiation temperature averaged over the interior hohlraum wall, $\langle T_r \rangle$, was 62.5 eV. The peak temperature averaged over the wall viewed through the aperture ($\langle T_{r,w} \rangle$) was 63.4 eV (see Figure 4) and was uniform within $\pm$ 0.5 eV

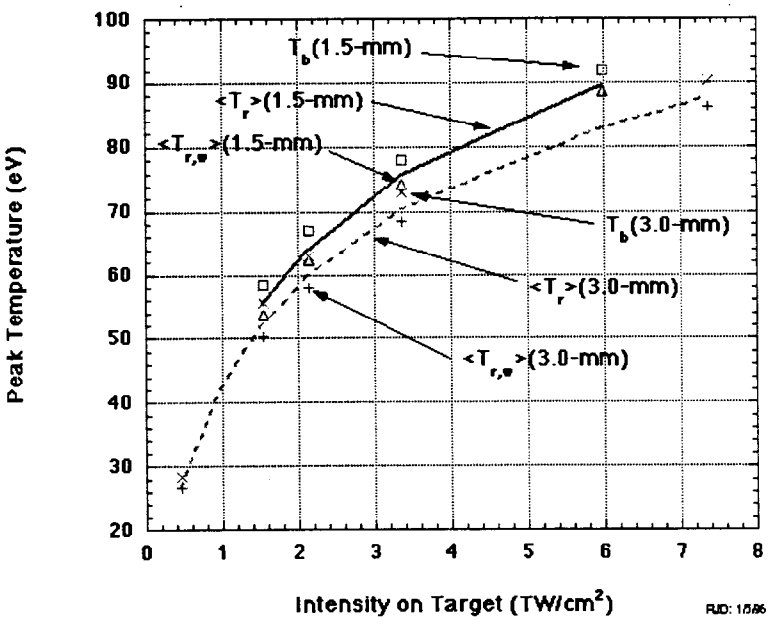

Figure 3. The hohlraum scaling with intensity on target.

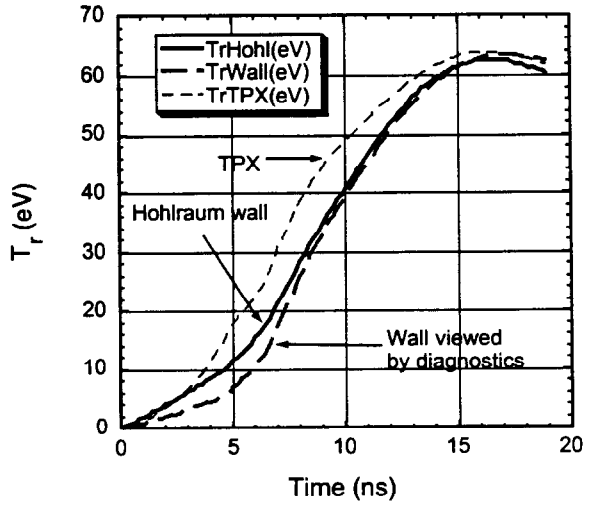

Figure 4. Radiation temperature of the TPX foam, the hohlraum wall, and the hohlraum wall viewed by the x-ray diagnostics.

at peak temperature. The temperature of the back wall lags behind the average wall temperature since the cylindrical walls are significantly heated by direct ion beam deposition. Note that $<T_{r,w}>$ is higher than $<T_r>$ in these calculations since $<T_r>$ is decreased by radiation losses of the wall near the apertures. The TPX-foam radiation temperature gets to 63.8 eV about 400 ps before the time of peak wall temperature, which corroborates the assumption that the foam deposition region is heating the hohlraum wall.

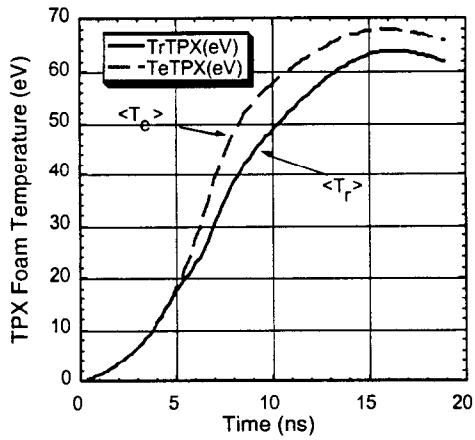

Figure 5. The calculated electron temperature of the TPX foam is higher than the calculated radiation temperature.

The foam electron temperature here is about 4-eV hotter than the radiation temperature at peak $<T_r>$, Figure 5, which is consistent with a system heated by Li-ion beam energy deposition primarily in the free electrons. The TPX foam in this hohlraum begins to fill and stream out the diagnostic aperture as the target is heated by the ion beam. As a result, foam filling the aperture tamps the aperture's motion, preventing it from closing during the experiment (Figure 6 and Figure 7). The TPX foam expands vertically 1.2 mm out of the aperture, reaching a velocity of 15 cm/μs in the center of the aperture. The foam density in this blow-off region correspondingly dropped from 5 mg/cm^3 to 1 mg/cm^3.

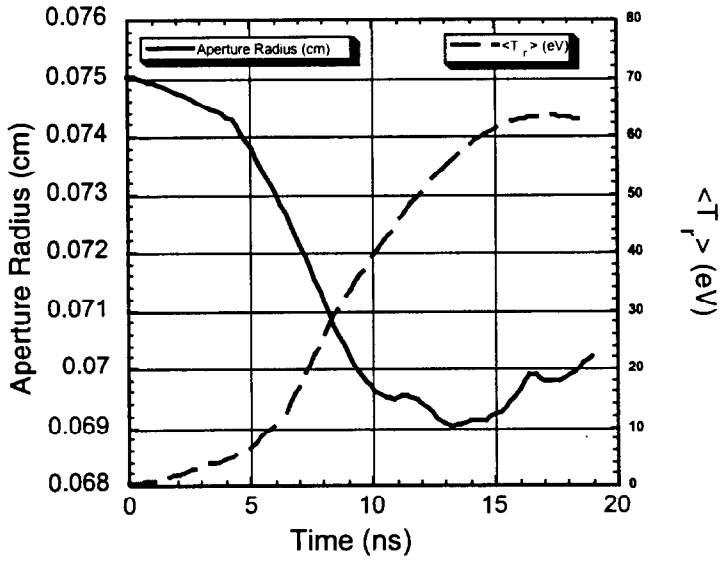

Figure 6. The aperture radius reaches a minimum (at 13.3 ns) before peak hohlraum wall temperature (at 17.2 ns).

The Rosseland mean free path in the hohlraum quickly reached an average value of 2.8 cm throughout the bulk of the hohlraum. In this low-density region close to the diagnostic

aperture, the x-ray mean free path in the foam was greater than 100 cm due to its reduced density. From an energetics point of view, the hohlraum interior was optically thin.

We considered three target geometries in order to understand the optimum response for a given Li-ion beam. These closed-geometry targets were a 4-mm-tall, 4-mm-diameter cylindrical hohlraum, a 6-mm-tall, 6-mm-diameter cylindrical hohlraum, and a 4-mm-small diameter by 6-mm-high by 8-mm-large diameter conic-section hohlraum. (See Figure 2 in section 6.) For this comparison we used a 9.1-TW Li-ion beam for all simulations. The results, shown in Figure 8, predict that the 4-mm diameter cylindrical hohlraum achieves the highest temperature for this ion beam even though it intercepts the least ion beam power. These results show that a 4-mm cylindrical hohlraum achieves higher radiation temperature than a 6-mm cylindrical hohlraum or a 4x6x8-mm conical hohlraum, assuming perfect beam aiming.

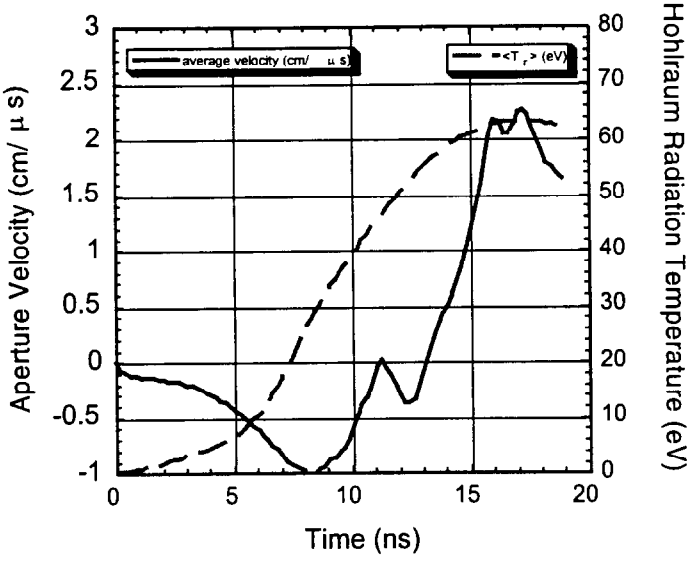

Figure 7. The aperture initially closes with a maximum velocity of -1.0 cm/μs and then begins to re-open as the hohlraum temperature rises.

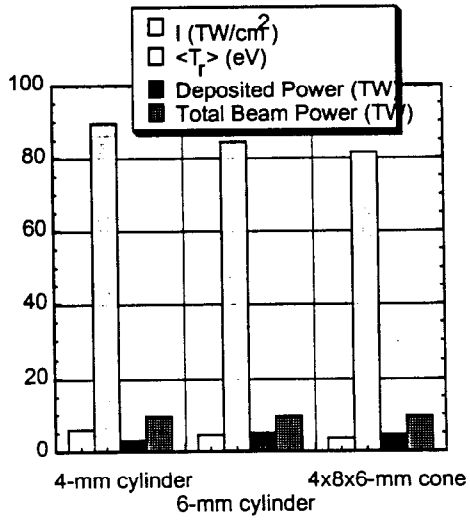

Figure 8. The simulations predict that a 4-mm cylindrical hohlraum achieves higher radiation temperature than a 6-mm-diameter cylindrical hohlraum or a 4x6x8 conical hohlraum.

Intentionally Left Blank

6. Target Fabrication and Characterization - J. Aubert

Introduction

The thermal x-ray target was designed as a hollow 4-mm-diameter right circular cylinder with 1.5 micrometer (μm) thick gold walls. The gold cylinder was supported by a thin polymer coating, parylene-D, and contained a low-density foam with a nominal composition of CH_2. The target is shown in Figure 1.

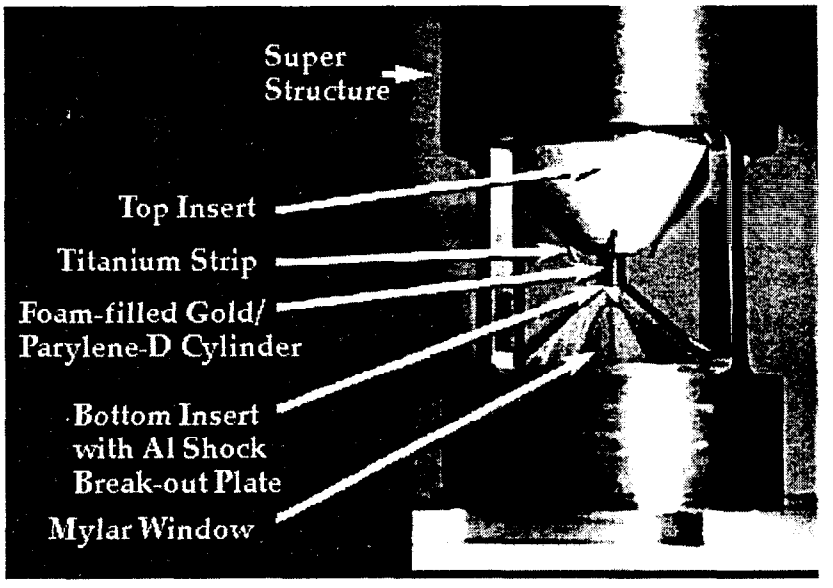

Figure 1. Photograph of the target showing the major components and the supporting super structure.

These targets were designed to absorb the energy of the ion beam within the foam, which converts the ion beam energy into x-rays.[1] X-ray radiation was observed from the top of the target through a circular diagnostic aperture with a diameter of either 1.5 or 3 mm. On the bottom of the target was a gold-coated aluminum witness plate, which was a component of an active, shock-breakout diagnostic. Surrounding the outside of the hohlraum were five titanium strips that produced ion-induced inner-shell x-rays (4.5 keV) to diagnose the lithium beam. At the top of the target, a large, conical, aluminum-coated, brass section (top insert) mechanically supported the hohlraum and intercepted any stray ion beam. At the bottom, another brass conical section (bottom insert), containing 3 μm mylar, poly(ethylene teraphthalate), windows, mechanically supported the hohlraum and provided a vacuum seal. The windows allowed x-ray emission from the titanium strips to be viewed from below. The target was supported in a super-structure machined from brass that meshed with the cathode hardware of the PBFA-II ion diode. The interior of the hohlraum and diagnostic pathways on the top and bottom were evacuated during the experiment and were designed to withstand a pressure differential of 2 torr.

Several different manufacturing processes were utilized in the preparation of these targets. Many of the components were mechanically weak because of density limitations (areal or volumetric). For example, the hohlraum walls were 4.5 μm thick; yet they had to be wrinkle free over the entire surface and be able to support a small differential pressure. The foam had a density of 5 mg/cm^3. For comparison, the density of dry air at 1 atmosphere of pressure is 1.19 mg/cm^3. Neither of these components could be handled

unless supported by another sacrificial structure. For the hohlraums, our handling philosophy was to prepare it on an extractable mandrel. After evaporating gold onto the mandrel, the gold and mandrel were attached to a robust part of the target support structure and only then was the mandrel removed by extraction (dissolution). In the case of the foams, they were prepared with a solvent-based process which used a solvent that is solid at room temperature. The solvent-filled foams were easily handled and machined. Only after placement within the hohlraum was the solvent removed by sublimation (freeze-drying). Thereby, the most delicate parts of the target endured no handling, but were supported until after their assembly into the target. Although these techniques made the assembly possible, they complicated characterization. More robust parts of the target were machined with traditional methods including electrical discharge machining. Films and coatings were prepared by chemical or physical vapor deposition and plasma spray.

Component Preparation

The major physics components of the target included the polymer-coated gold cylinder (hohlraum), the foam retainer (lid to the hohlraum) including its diagnostic aperture, the foam, the titanium beam diagnostic strips outside of the hohlraum ("titanium birdcage"), and the aluminum shock-breakout plate. These are shown in Figure 2.[2]

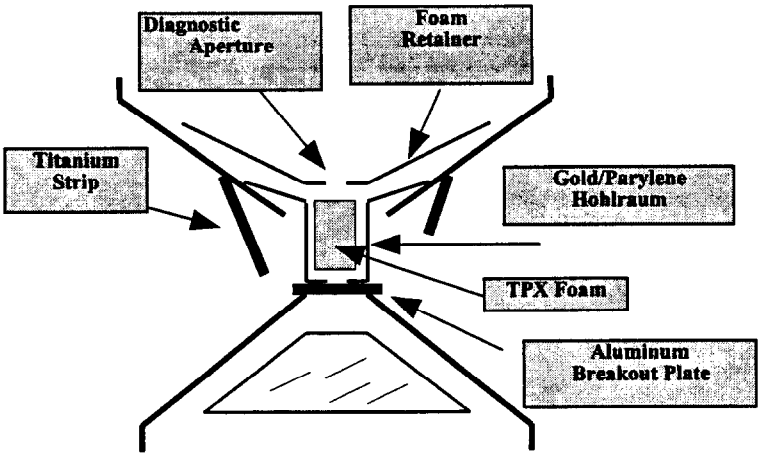

Figure 2. Illustration of the target's major components.

Hohlraum and Foam Retainer

The hohlraum consisted of a hollow polymer-coated gold 4-mm-diameter right circular cylinder. The foam retainer's purpose was twofold: to provide precise diagnostic apertures, and to form the lid for the hohlraum which held the foam in place. Both components were prepared in similar ways. First, a mandrel of extrusion grade acrylic, poly(methylmethacrylate), was machined and polished to the required shapes. Mandrels

were then coated with 1.5 μm (hohlraum) or 2 μm (foam retainer) of 99.999% purity gold in a physical vapor deposition coating chamber using an electron beam source. The mandrels were held in a 0.5 Hz rotating fixture and the angle of the mandrels with respect to the source was varied from 90° to 45° to ensure uniform coating on all surfaces. A witness slide was attached to each mandrel stem for subsequent profilometer measurement, and a surplus part of the mandrel coating was also used for direct measurement of the coating thickness. Coated mandrels were checked for pinholes by directing a fiber optic light into the acrylic and observing light emission through the gold coating. Only mandrels that had no pinholes were processed further.

The foam retainer had an extra 12 μm of gold electroplated to bring its thickness up to 14 μm. Gold-coated hohlraum mandrels were coated with 3 μm of parylene-D, poly(di-chloro-para-xylylene),[3] $\{-C_8H_6Cl_2-\}_n$. These mandrels were mounted horizontally onto a rotating fixture inside the parylene coater. Witness slides were mounted with the mandrels and profilometer measurements were later used to obtain the thickness of the coated parylene-D.

Mandrels for the hohlraum and foam retainer were designed with a stem, to hold and rotate the part, and with sharp edges wherever a cut in the coating was required. These edges were trimmed with a sharp razor at the location of the apertures and the edge of the part. The hohlraum mandrel is shown below (Figure 3) with these extra features indicated. The foam retainer mandrel looked similar. Foam retainer mandrels were extracted with acetone and stored until assembly. Hohlraum mandrels were not extracted until after assembly into the top insert because of their delicate structure.

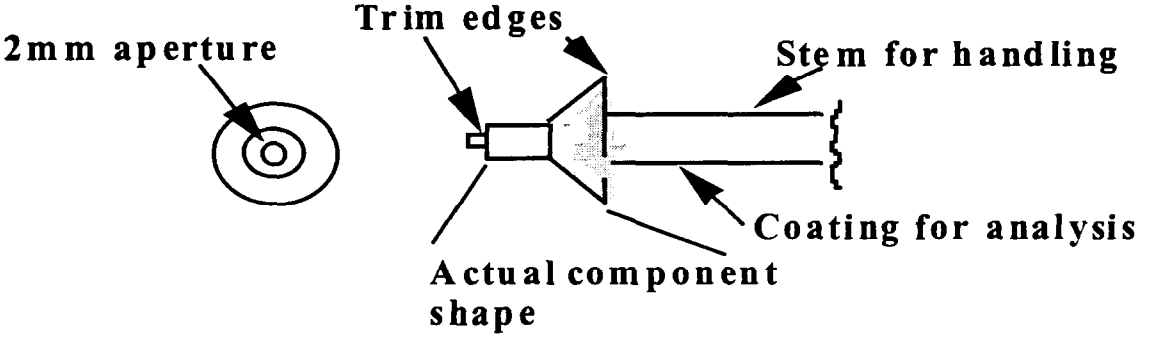

Figure 3. Hohlraum mandrel design.

Foam

Poly(4-methyl-1-pentene), TPX, foams were obtained from Oak Ridge National Laboratories[4] (ORNL). The foams had a nominal composition of CH_2 and density of 5 mg/cm^3. The foams were prepared with a solvent-based phase separation process whose general features are described elsewhere.[5] In the particular process employed by ORNL, the solvent used was a solid at room temperature with a low vapor pressure (51% naphthalene and 49% durene). The foams were machined at ORNL to the hohlraum dimension (4-mm right circular cylinder) with the solvent filling the porous regions of the foams (approximately 99.5 volume %). These machined solvent-filled foams were then shipped to us under a vapor pressure of the solvents and upon arrival were stored in a freezer. This procedure prevented solvent loss and the probable structural damage that would occur in the resulting weak foams.

Titanium Strips

Titanium beam characterization strips were produced using a wire-EDM (electrical discharge machining) process. Square strips (0.02 inch on a side) were arranged around the hohlraum by bonding one end of each strip into machined holes in the top insert. The strips were angled at 65° from horizontal toward the bottom of the hohlraum in a skeletal cone shape. They were arranged in either of two configurations: (1) three longer (0.445 inch) and two shorter (.255 inch) strips or (2) all long strips.

Shock-Breakout Plate

Aluminum shock-breakout plates were prepared by Texas Instruments Custom Optics Division[6] by diamond point machining of Al-6061 alloy (0.15% Ti, 0.25% Zn, 0.35% Cr, 1.2% Mg, 0.15% Mn, 0.4% Cu, 0.7% Fe, and 0.8% Si). The aluminum was machined to a 5-mm-diameter disk with an initial thickness of 150 μm. One surface of the disk was machined to a flat mirror finish. Then a step of 50 μm covering half of the plate was machined into the other side. The total plate thickness was then 150 μm over half of the plate and 100 μm over the other half. The flat side of the plate was coated with chromium (150-200 Å for adhesion) and then with 1.5 μm of gold by e-beam evaporative coating. After assembly, the gold coated side formed a part of the bottom of the hohlraum.

Assembly Procedure

Targets were built from two subassemblies, the bottom insert and the top insert, which were positioned and aligned within the supporting super structure, i.e., the target body. The bottom insert was composed of a brass structure covered (on the side toward

the beam) with 25.4 μm of plasma-sprayed aluminum, with windows in four quadrants. Each window was covered with 3 μm of Mylar. An aluminum shock-breakout plate was attached to the top. Both the shock-breakout plate and the Mylar-covered windows formed vacuum seals.

Once completed, the bottom insert was installed into the target body. After curing the adhesive, the target body containing this subassembly was placed into a leak check fixture, pressurized to 3 torr with argon, and monitored for 30 minutes. Only assemblies with a leak rate of less than 0.02 torr/min were accepted and processed further.

The top insert was composed of a brass conical-shaped piece coated on its outer surface (facing the incoming beam) with 25.4 μm of aluminum by a plasma spray process. Five pilot holes were placed in the top insert; these were used to locate and secure the titanium strips. A single strip was placed in quadrants one, two, and four, and two strips were placed in quadrant three. The appropriate strips (short or long) were oriented in the top insert by an assembly fixture and bonded in place with a fluorescent-tagged epoxy (N-methyl pyrolidone added to fluoresce between 360-400 nm). After curing, the assembly was examined under ultraviolet (UV) light to detect fluorescence from vagrant epoxy. If vagrant epoxy was observed, the strips were removed and bonded again. Once the strips were secured, a hohlraum mandrel was bonded into the top insert using a solvent-resistant epoxy, and then the entire top insert was placed into an acetone bath for extraction of the hohlraum mandrel. A completed top-insert is shown in Figure 4.

Next, the top insert was attached to the target body with the use of another bonding fixture and telescope coupled to a video monitor. The top-insert was mounted on a shaft with the titanium strips positioned in the proper quandrants. The top-insert was then lowered by micrometer adjustment into the target body to enable the bottom of the hohlraum to be secured to the shock break-out plate. The epoxy used also contained a UV tracer. The three bond lines at the hohlraum/shock-breakout plate, the hohlraum/top-insert interface, and the top-insert/target body interface formed vacuum seals. These were checked by leak testing the entire target at this time to the same criteria as the bottom insert, i.e., a maximum leak rate of 0.02 torr/min at 3 torr of argon for 30 minutes.

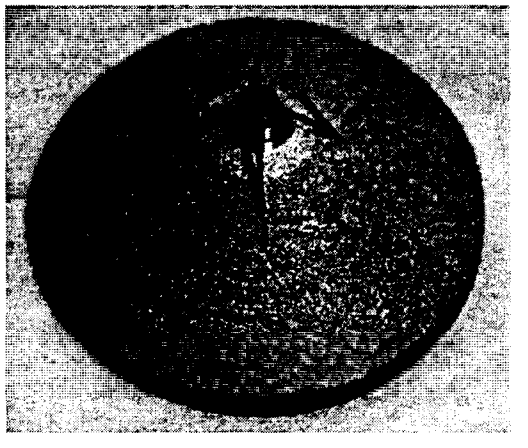

Figure 4. Completed top insert consisting of an aluminum-coated brass conical support structure, titanium strips, and a parylene-D/gold hohlraum.

Finally, a solvent-filled foam cylinder was installed into the hohlraum, and then

freeze-dried at 15 °C and a vacuum of 25 torr for 30 hours. A foam retainer was bonded into the top-insert to hold the foam in the hohlraum and to provide the diagnostic aperture. A brass debris block completed the target fabrication.[2]

Characterization

A variety of analytical techniques were used to characterize the hohlraum, foam retainer, titanium strips, and the foam. These included optical measurements, microphotography, scanning electron microscopy, radiography, profilometry, and Rutherford backscattering. Many of the characterizations were destructive and could only be performed on statistically representative samples. The specifications for delivered targets were then inferred from the measurements destructively performed on similar samples. Photographs were taken of all the components, assemblies, and completed targets and were used to document positioning, concentricity, and foil quality.

Foam

Foam density was calculated from volume and weight measurements of foam bricks. (The cylindrical solvent-filled foam pieces were machined from these same solvent-filled bricks prior to solvent removal.) Volume was determined from optical comparator measurements of the bricks after solvent removal. The bricks were then weighed. Although the volume of these bricks was two orders of magnitude greater than an individual hohlraum foam, we estimate that the accuracy of this technique to obtain density is approximately five percent due to a lack of parallelism and a rough surface finish. The densities of two bricks were found to be 4.1 mg/cm^3 and 4.9 mg/cm^3 (average of 4.5 mg/cm^3; requested density 5 mg/cm^3). This variation may be partly due to variability in the shrinkage of the foams during solvent removal. Typical shrinkage was found to average about 7%. Scanning electron microscopy (SEM) was performed on a foam sample which was freeze-fractured to preserve its morphology. The foam surfaces were sputtered with a thin gold/palladium layer to reduce charging in the 3-kV electron beam. Cell sizes between five and one hundred μm were observed as shown in the SEM images of Figure 5.

Photographs were taken of the top of the foam after insertion into the hohlraum and removal of the solvent in order to verify the absence of dirt or visible contaminants and to ensure that the shrinkage of the foam was uniform and not excessive. No other characterization could be performed on the actual foams used in the experiments because of their delicate nature. The possibility of using ion microtomography to characterize the density variation within a cylindrical foam sample was investigated. However, this process proved destructive to these particular foams because of the mounting, handling, and transportation required. Solvent-filled foam cylinders were first mounted on a suitable substrate for analysis, the solvent removed, and then transported to the ion tomography equipment. Data was successfully taken for purposes of demonstrating the capability of ion tomography on foams of this density. The data showed that density variations as small as 1% could be determined with a spatial resolution of 10 μm.

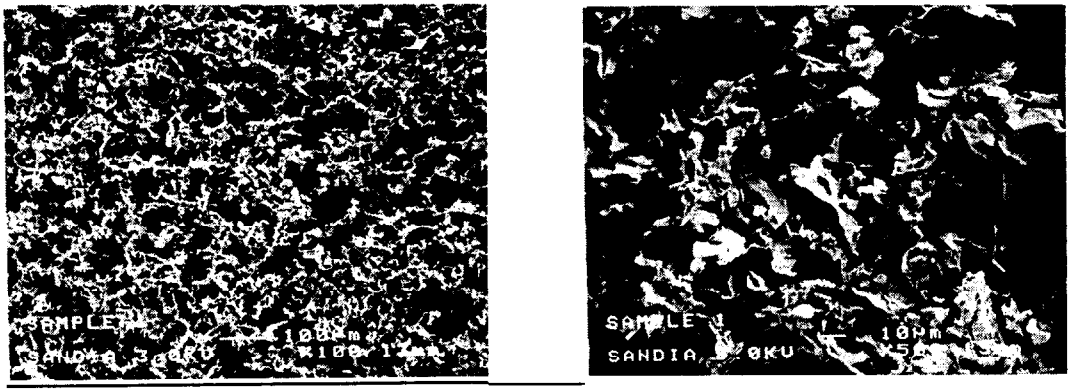

Figure 5. Scanning electron photomicrographs of nominal 5mg/cm^3 TPX foam.

Hohlraum Wall Thickness

Hohlraum walls were composed of vapor deposited gold and parylene-D. Thicknesses were determined using a Dektak® profilometer on witness slides located very close to the actual parts in the coating chamber. The measurements were made separately; one for the gold coating and one for the parylene-D. The accuracy of this data is considered to be within ten percent. Rutherford Backscattering Spectroscopy (RBS) was performed on the coating deposited on an excess part of the mandrels (as seen in Figure 3). Accuracy for the RBS technique is approximately five percent. Table 1 contains both profilometry and RBS measurements for each hohlraum. Both the gold and parylene-D coatings were very close to the design values. The average parylene-D coating was within 2.7% of the design value and the greatest deviation from the design value was under 11%. The gold thicknesses, as judged by RBS, were also very close to the design value. The greatest deviation was under 15%, while the average gold thickness was within 5% of the design value. The gold thickness deposited on 75% of the targets was within 5% of the design value and 87.5% was within 10%.

Table 1. Hohlraum thickness data for parylene-D and gold. Design thicknesses were 3 μm parylene-D and 1.5 μm gold. Deviations (in %) from design thicknesses are also shown.

Target Number	Dektak® Thickness μm Gold	Dektak® Thickness μm Parylene-D	RBS Thickness μm Gold
LT794-4ITF (ITF TEST)	1.52 (+1.3%)	2.83 (-5.7%)	1.55 (+3.3%)
LT794-5	1.52 (+1.3%)	2.83 (-5.7%)	1.55 (+3.3%)
LT794-6	1.54 (+2.7%)	3.32 (+10.7%)	na
LT794-8	1.49 (-0.7%)	3.13 (+4.3%)	na
LT794-9	1.60 (+6.6%)	3.14 (+4.7%)	1.29 (-14%)
LT794-10	1.52 (+1.3%)	3.13 (+4.3%)	1.41 (-6%)
LT794-11	1.51 (+0.7%)	3.13 (+4.3%)	1.49 (-0.7%)
LT794-12	1.53 (+2.0%)	3.13 (+4.3%)	1.47 (-2%)
LT794-13	1.48 (-1.3%)	2.98 (-0.7%)	1.51 (+0.7%)
LT794-14	1.51 (+0.7%)	2.98 (-0.7%)	1.44 (-4%)
LT794-16 (RADIOGRAPHY TARGET)	1.52 (+1.3%)	3.23 (+7.7%)	na
Mean	1.52 (+1.3%)	3.08 (+2.7%)	1.46 (-2.7%)

na= not available

Target Centering and Positioning

Optical comparator measurements (Gage Master, Series 20) were made on targets to determine the hohlraum height and diameter, the aperture diameter, the vertical and horizontal centering of the hohlraum with respect to the target body, the centering of the aperture with respect to the target body, the angles of the titanium strips, and their length and width. The optical comparator works by projecting a shadow image of the target onto a screen. Dimensions are then determined by a computer-controlled positioning program that measures distances and angles to an accuracy of 2 μm. Some of these measurements are summarized in Table 2.

Hohlraum diameters closely approximated the designed diameter of 4 mm. Hohlraum height showed more variability because both the top and bottom were bonded with epoxy to other components, and the thickness and other factors of the adhesive could change the overall height. The titanium strips were aligned very accurately due to the

fixture that was used to secure them. The angle of the strips with respect to horizontal in two viewed directions (viewed by looking toward the center of the hohlraum and at 90° to this view) was always within 3° of the designed angle and in the majority of cases was within 1°.

Hohlraum centering was calculated from optical comparator measurements of distances from the target body to the hohlraum edge at two positions (90° apart). Hence, the off-center number is only an estimate based upon these two data points. In general, the hohlraum was centered horizontally almost perfectly. The average deviation was less than 0.1 mm. Variation in the vertical centering in the cathode hardware was totally due to the size of the spacer used. Based upon optical comparator positioning information, we chose a spacer size which yielded an average deviation in the vertical centering of less than 0.04 mm. This was well within our diagnostic resolution.

Table 2. Target Component Concentricity.

Target Number	Hohlraum Diameter	Hohlraum off-Center Horizontal	Hohlraum off-Center Vertical	Foam Retainer Aperture	Aperture off-Center
Design Value	4 mm	0.0 mm	0.0 mm	3.0mm or 1.5 mm	0.0 mm
LT794-5	4.002	0.1264	-0.068	3.022	0.492
LT794-6	3.926	0.0365	-0.039	3.020	0.292
LT794-8	3.968	0.1723	-0.073	2.998	0.178
LT794-9	4.002	0.0480	+0.032	3.054	0.316
LT794-10	3.996	0.1253	0.000	3.030	0.079
LT794-11	4.004	0.0921	-0.001	1.610	0.040
LT794-12	3.954	0.0510	-0.061	1.560	0.242
LT794-13	3.964	0.0100	-0.005	1.668	0.175
LT794-14	3.958	0.0500	+0.046	2.984	0.030
LT794-16	3.968	0.2233	-----	1.498	0.171
MEAN	3.974	0.093	0.036	3.018 (3 mm) or 1.584 (1.5 mm)	0.202

Aperture diameters and centering were measured in a similar way. Only two measurements (at 90° apart) were used to estimate the centering of the apertures. The diameters were very close to the desired design values. For the 3 mm diameter aperture the average deviation from this design was only 0.6%. For the 1.5 mm diameter apertures the average deviation from this design was significantly greater but still under 6%. The apertures were off-center by an average of 0.2 mm, with significant variability.

Radiography

Radiography, digitization, and colorization were performed on a single target, #LT794-16, that was fabricated specifically for this purpose. It was considered representative of all delivered targets. In Figure 6, one of the radiographs shows a distance from the titanium strips to the gold foil.

Documentation

Documentation occurred at all stages of the assembly process in order to provide both archivial information and quality control measures on the process. The components and the subassemblies had associated documentation; details of preparation and characterization were recorded and this "traveler" remained with its component throughout the assembly process. The target assembly was also documented on an "assembly sheet," which verified that every step was completed, all characterizations were performed, and all data recorded. Some methods of characterization were documented separately. With each delivered target, a "delivery sheet," containing some of the most important target specifications, was included. Table 3 summarizes the sequence of targets shot on PBFA II and their most pertinent configurational information. Finally, a target assembly procedure was written at the end of the target assembly process to document, for archival purposes, the details of the assembly process and all of the characterization results.[2] All travelers, characterization results, and delivery sheets are archived in folders for future reference. In addition, numerous parts have been archived, including the witness slides from all coatings and the radiography target. These parts are available to answer any materials questions which could arise when data are analyzed in the future.

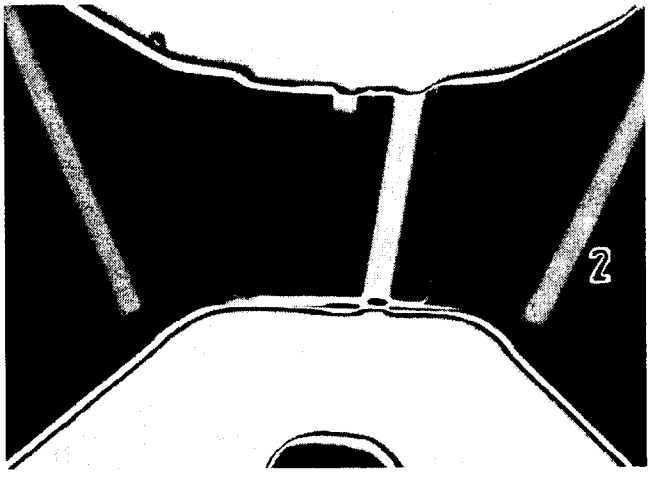

Figure 6. Technique used to image the distance from the strips to the gold foil: 35 kV, 500 μA, 165-second exposure time; source-to-object distance: 2-1/8″; source-to-film: 27″. A hard cassette was used with Kodak AA film sandwiched between .001″ of lead foil with 0.010″ of lead screen behind the foil to reduce scatter.

Table 3. The sequence of targets shot on PBFA II.

Shot Sequence	DAS Shot Number	Pre-Shot Number	Target Number	Aperture Diameter (mm)	Strip Configuration	Delivery or Shot Date
1	6501	2025	LT794-5	3.0	all long	delivered 7-13-94
2	6517	2026	LT794-6	3.0	2 short; 3 long	delivered 7-21-94
3	6529	2027	LT794-8	3.0	2 short; 3 long	delivered 7-27-94
4	6542	2028	LT794-9	3.0	2 short; 3 long	shot 8-9-94
5	6547	2029	LT794-10	3.0	2 short; 3 long	shot 8-11-94
6	6551	2030	LT794-11	1.5	2 short; 3 long	shot 8-12-94
7	6554	2031	LT794-12	1.5	2 short; 3 long	delivered 8-12-94
8	6560	2032	LT794-13	1.5	2 short; 3 long	delivered 8-16-94
9	6569	2033	LT794-14	3.0	2 short; 3 long	delivered 8-18-94

Conclusions

Due to the delicate nature of the hohlraum's foil and foam and the available analytic techniques, these components could not be directly characterized without destroying them. Instead, components were characterized by gathering data on similar materials, and extrapolating these results to the actual target components. Other aspects of the targets were characterized nondestructively. A total of nine targets were delivered and shot for this series.

We had excellent data on the vertical and horizontal positioning of the hohlraums. Deviations of horizontal positioning from the design were, at most, tenths of a millimeter, and deviation from vertical were negligible. From a fabrication standpoint, the targets were perfectly centered. The parylene-D/gold hohlraums were the correct size and had no visible flaws such as wrinkles or discoloration. Wall thicknesses of the hohlraums were very close to the design specifications in all cases. Maximum deviations of paylyene-D thickness from design thickness were under 10% and for gold, under 15%, but the majority were much closer. Titanium strips were the correct size and had near-perfect alignment due to the bonding fixture which was used.

One weak area in our characterization was in the measurement of the top aperture size and circularity. We measured two diameters of the top aperture at 90° from each other and then averaged these to compare to the desired value. This gave us no information on the uniformity of the diameter (i.e., circularity), although photography allowed us to keep a permanent visual record. If targets of this type are used in the future, a system to completely evaluate the shape of the aperture, the quality of its edge, and the area that it circumscribes will be important. These apertures were formed by cutting a gold foil with a scalpel. This worked quite well for the 3-mm diameter apertures, but was less accurate for the 1.5-mm diameter apertures. For the future, we

need to develop a more accurate method of cutting the foil. Possible candidates are laser or e-beam machining.

The low-density foam may be the most important physics component of this target. But by far the weakest area of this target assembly was the foam preparation and characterization, including its density, density uniformity, and even volume. We should spend more effort to develop the technology to prepare these low-density foams. (Another problem not be discussed here, but with very serious repercussions, was the occasional contamination of targets by foreign materials during insertion into PBFA II.)

Characterization of the foams was limited. Better preparation of foam blocks for density analysis is required. These blocks were removed from the main foam brick and were shaped by hand to form a parallelepiped. A more accurate method would be to have several extra target pellets machined, accurately measured, and weighed. In addition, a statistical evaluation should be made of the foam sampling technique to obtain the best specimens for analysis.

No information on density uniformity was obtained, although ion microtomography appears promising. This technique should be developed, optimally as a nondestructive test, to obtain direct information about density and density uniformity. For example, if the foam could be permanently attached to a rigid base, it could be transported to the ion microtomography beam and then returned for use as a characterized target if the base were a part of the target design.

Acknowledgements

Patti Sawyer and Paul Baca contributed to the development of the procedures and documentation described in this chapter. We sincerely appreciate the efforts of Bonnie McKenzie and Gary Zender for the SEM photos, Art Pontau and Arlyn Antolak for their work demonstrating ion microtomography, Deanna Sevier and Kyle Thompson for radiography, George Arnold for RBS, Bob Henning for plasma spray, and the projects machining department. All of their dedicated efforts were needed for the success of this target series.

References

[1] T. A. Mehlhorn, Ion Beam Coupling and Target Physics Experiments at Sandia National Laboratories," in "Laser Interaction & Related Plasma Phenomena," ed by G. H. Miley & H. Hora, 10 (1992).
[2] P. S. Sawyer, P. M. Baca, M. Smith, and J. H. Aubert, "1994 Lithium Thermal Target Assembly Procedure," communication of Sandia National Laboratories, internal memo, 1994.
[3] M. Szwarc, Polym. Eng. and Sci., 16 (7), 473 (1976).
[4] Manufactured by Ron Simandl, Oak Ridge National Laboratories, Oak Ridge, Tennessee.
[5] J. H. Aubert and A. P. Sylwester, "Microcellular foams? Here's How!," CHEMTECH, 21, 290 (1991).
[6] Manufactured by George Platt, Texas Instruments Custom Optics Division, Dallas, Texas.

7. Diagnostics

7.1 Diagnostic overview - M. S. Derzon

The ion beam properties have been shown to vary greatly from one PBFA- II shot to the next,[1] and to have variations in intensity with azimuth and height.[2] This means that it is important to measure temporal and spatial characteristics of the ion beam on each shot. Because of this a great deal of effort has gone into characterization of the beam as well as thermal emission from the target. Section 7.4 contains discussion of the beam intensity measurements near the target. This important new capability is demonstrated in these experiments. The purpose of this diagnostic chapter is to document the instruments used and the initial analysis.

Figure 1 illustrates the cylindrical hohlraum target. The diagnostic aperture and all the soft x-ray diagnostics are located above of the target. Bottom x-ray diagnostics view inner-shell emission from the Ti-strips. A laser beam that is part of the active shock breakout diagnostic is also incident upon and reflected from the stepped witness plate at the bottom of the target.

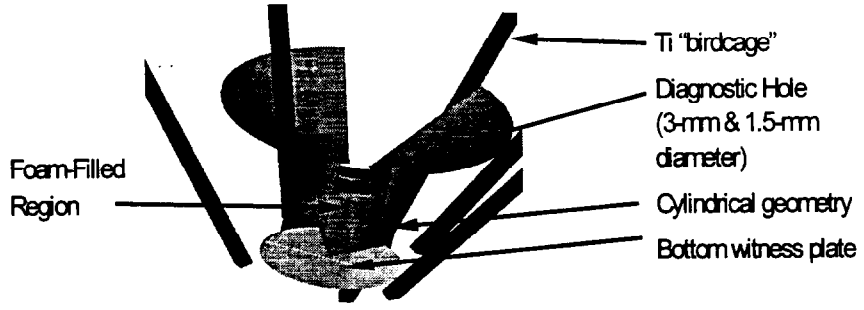

Figure 1. Cutaway Target Schematic.

Figure 2 shows the hohlraum target inside the ion beam transport region, called the gas cell show. The figure shows the relative locations of the target, top and bottom lines-of-sight (LOS), the neutron source target (CD_2) is located on one of the four gas cell post that maintain the anode to cathode separation, and

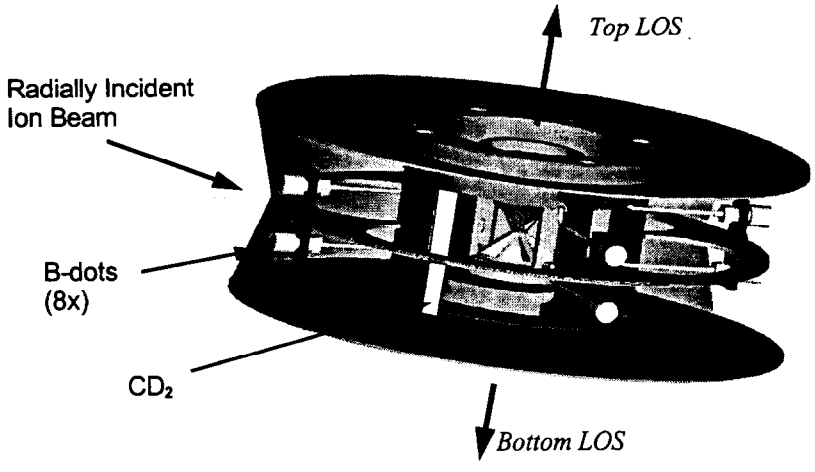

Figure 2. Target inside Gas Cell.

the mechanical hardware surrounding the target. The neutrons travel near the equatorial plane of PBFA II through an evacuated tube to a scintillation detector (n-TOF).

With the target placed between the upper and lower diagnostic packages, the locations of the rest of the diagnostics are indicated in Figure 3. The uppermost region, the top re-entrant diagnostic package, contains x-ray diodes (XRD), bolometers, x-ray spectrometers, and the time-resolved framing camera. The energy-, space- and time-resolved (EST) and the upper time-integrated pinhole cameras (U-TIXRPHC) are located just above the target within a large tungsten shield. Below the target are the time-integrated soft x-ray cameras (on-axis TIXRPHC), the fiber-based beam intensity (FBI) diagnostic, the on-axis three-frame time-integrated x-ray pinhole camera, and the active shock breakout (ASB) camera. Table 1 lists the location, parameters, and purpose of each diagnostic that views the target.

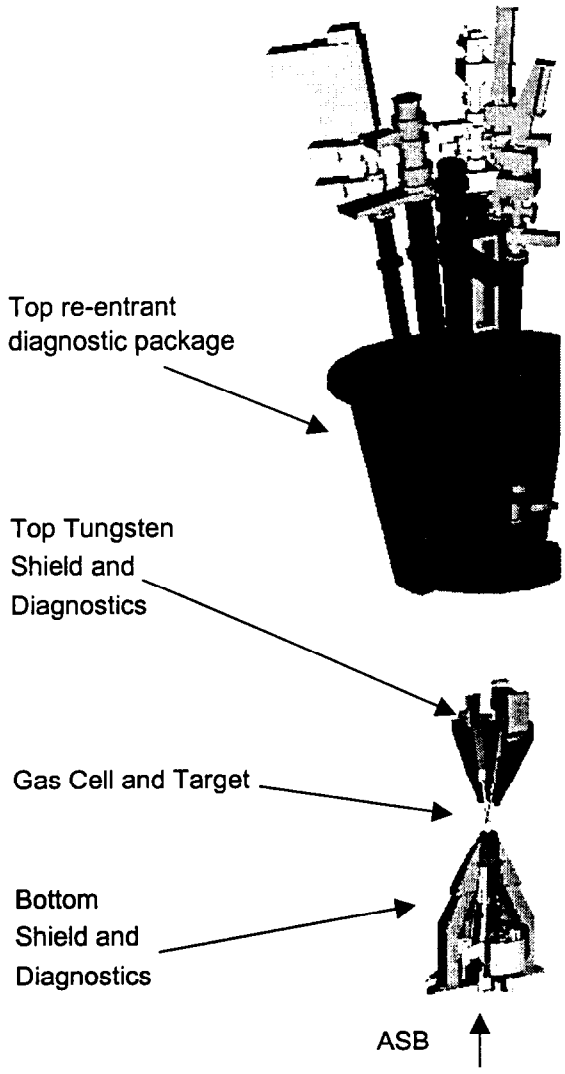

Figure 3. Target and diagnostic locations.

The individual sections in this chapter discuss the instruments, efforts, and lessons learned in fielding these instruments so that future efforts can build upon the successes and failures. Where reasonable, individual sections are being prepared in appropriate detail for outside publication. The first diagnostic section describes the inner-shell x-ray cameras used for diagnosis of beam performance, and the next three contain detailed information related to the analysis of this data. Section 7.6 contains the analysis of the upper soft x-ray cameras. Sections 7.7-7.9 contain information germane to the analysis of the streaked fiber-based diagnostics. A description of the instrument and the analysis of the active shock breakout diagnostic is given in Section 7.10. The neutron time-of-flight results are presented in Section 7.11, a description of the bolometers is in 7.12, and a comparison of the characterization methods for x-ray filters that are employed in many of the x-ray diagnostics is in 7.13.

Table 1. Listing and description of diagnostics.

Diagnostic	Location	Purpose-quantity measured	* Did it meet objectives?
XRDs/p-i-ns	Top Re-entrant	broadband spectra, calibrated	Y
Bolometers	Top Re-entrant	integrated emission	Y
Grazing Incidence Spectrometer	Top Re-entrant	Time-resolved and time-integrated high-resolution spectra	N
Transmission Grating Spectrometer	Top Re-entrant	1-D, time-resolved, moderate-resolution energy spectra	N
Time-resolved framing camera	Top Re-entrant	hole closure and time-resolved emission profile, 3-time and 4-energy band camera	N
energy-,space-, and time-resolved (EST) soft x-ray instrument	Inside upper shield	hole closure velocity, crude energy resolution, 1-D Spatial, continuous time	Y
Upper time-integrated pinhole camera (TIXRPHC)	Inside upper shield	high-resolution, 2-D image of measure time-integrated emission profile, and Ti emission	Y
time-integrated x-ray cameras	Inside bottom shield	time-integrated emission, serves as backup for on-axis cameras	Y
On-axis TIXRPHC	Inside bottom shield	beam energy uniformity based on Ti emission	N
FBI	inside bottom shield	pulse width on-target	partially
n-TOF	TOF tube out side of machine	estimate of beam energy at a single azimuth	Y
Active Shock Breakout (ASB)	laser passes through bottom shield	test of active shock breakout concept in ion-driven target	partially

* data and analysis adequate to contribute to publication.

References

[1] M. S. Derzon, G. E. Rochau, G. A. Chandler, A. R. Moats, R. J. Leeper, Rev. Sci. Instr. **66**, 740(1995)
[2] M. S. Derzon, et al., *Phys. Rev. Letters*, Jan. 15 (1996).

7.2 Inner Shell X-Ray Cameras - A. R. Moats

Two time-integrated x-ray pinhole cameras (TIXRPHCs) were fielded below the cylindrical target for the 1994 Target Series. As discussed in Chapter 6, the hohlraum target is a 4-mm-diameter, 4-mm-high cylinder with thin gold walls and an interior filled with foam. A brass cone insert with 4 windows covered by 3-micron-thick mylar supports the cylindrical target from below. These windows act as the argon gas-vacuum interface and allow several diagnostics, including the TIXRPHCs, to view the target from below. These x-ray pinhole cameras viewed the ion-beam-induced Ti K_α and Al K_α characteristic line radiation from the target.

The TIXRPHCs were simple pinhole cameras that included tungsten pinholes, filters to selectively separate the different characteristic line energies, and layers of KODAK SB5 and DEF film to record the x-ray images of the target.[1] Images at 4.5 keV (Ti K_α), 1.5 keV (Al K_α), and greater than 6 keV (higher energy contamination) were taken during each PBFA-II shot. A magnet assembly eliminated ion contamination of the x-ray film from Rutherford-scattered ions.[2] Extensive shielding eliminated the majority of the bremsstrahlung created from the electron loss near the diode region. The remaining bremsstrahlung formed a uniform background on the film images that was well below film saturation. Both cameras had a demagnification factor of 0.67 and were inclined at 8° from vertical.[3]

The line of sight of the TIXRPHCs viewed the array of five titanium strips (the Ti "Bird Cage") placed at five different azimuthal locations around the target and, to a lesser extent, the aluminum-covered cone insert above the cylindrical hohlraum. The beam-induced Ti K_α characteristic radiation from the Ti Bird Cage measured the incoming lithium beam parameters. The Al K_α characteristic radiation from the larger cone above the target was used for qualitative information on beam symmetry. The analysis of this data is discussed more fully in Chapter 8.

References

[1] W. C. Phillips and G. N. Phillips, Jr., 1985, J. Aderzon, M. S., Sweeney, M. S., P. Grandon, H. C. Ives, R. P. Kensek, L. P. Mix, and W. A. Stygar, 1988, Rev. Sci. Instrum. 59(8), 1834.ppl. Crystallogr. 18, 3.

[2] M. S. Derzon, M. A. Sweeney, P. Grandon, H. C. Ives, R. P. Kensek, L. P. Mix, and W. A. Stygar, 1988, Rev. Sci. Instrum. 59(8), 1834.

[3] A. R. Moats, M. S. Derzon, G. A. Chandler, R. J. Dukart, and T. A. Haill, 1995, Rev. Sci. Instrum. 66(1), 743.

7.3 Systematic Ion-atom Interaction Cross Sections and Stopping Powers in the Plane Wave Born Approximation - E. J. McGuire

To infer current from inner-shell x-ray emission measurements and energy deposition accurate estimation of the stopping power is necessary. Description of the stopping power estimates is provided in this section. In Chapter 14 of "Atomic and Molecular Processes",[1] Bates outlines a procedure for calculating ion-atom cross sections in the plane-wave Born approximation (pwBa). The procedure involves integration over the product of elastic scattering factors or generalized oscillator strengths for excitation or ionization from both projectile and target. We have programmed this procedure to use our large data base of excitation and ionization generalized oscillator strengths (GOS). The program calculates both cross section and stopping power (SP) on a subshell basis. The calculations are done in the center of mass system, where the distinction between projectile and target is lost. Thus the SP in either lab frame is symmetric in target and projectile nuclear and net charges. The traditional simple modeling of SP, using scaled proton SP and an effective projectile charge, is unsymmetrical and therefore problematic. At high projectile energy the SP curves, as a function of increasing projectile charge, approach the scaled protonic result from above, indicating that lowering the effective charge raises the SP. A survey of Li ion cross section and stopping power results is given in Reference 2.

It has been known for at least 30 years that the pwBa overestimates the calculated ionization and stripping cross sections for ion-atom interactions at low energy. The question is by how much, and at what energy does the pwBa become accurate. My calculations show that a similar situation occurs for the case of SP. In Figure 1, I compare the calculated SP for Li ions on atomic nitrogen with one-half the measured molecular SP.[3,4] The two sets of measurements are in reasonable agreement and agree with the calculated results above 1 MeV. Thus, for 1-10 MeV Li ion beams we can calculate SP in carbon, nitrogen, and oxygen with

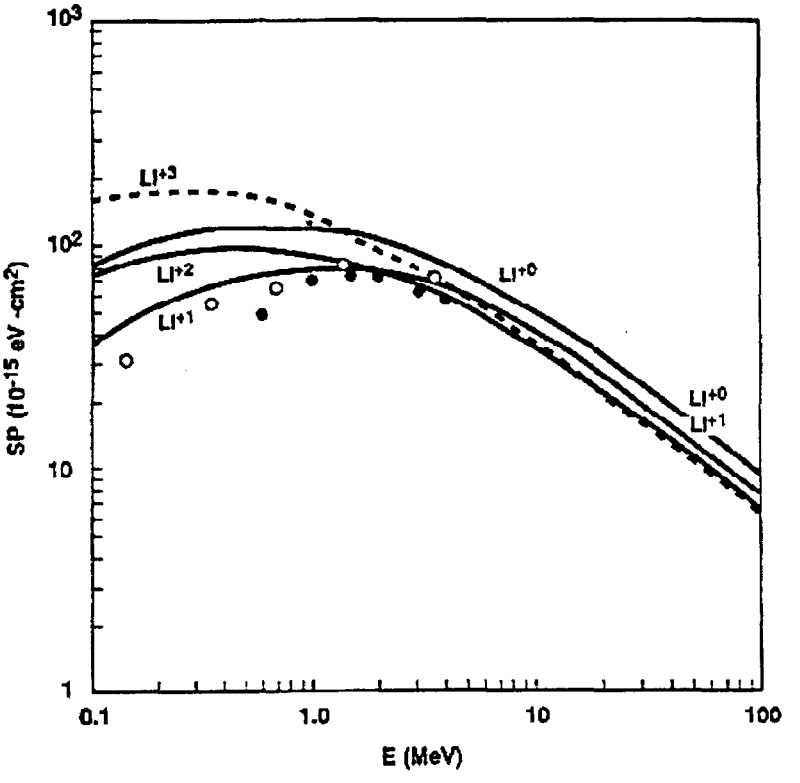

Figure 1. Comparison of calculated SP for Li on nitrogen with the measurements of Allison, et al.[3] (solid circles) and Teplova et al.[4] (open circles).

confidence. In Figure 2, the calculations for the SP of Li ions on gold are shown along with the measurement. The agreement is poor below 10 MeV. One may question the accuracy of the measurements in Reference 4 since the measured SP maximum is approximately 10^{-13} eV-cm^2, independent of the target Z. This is based on the Bethe theory, where one expects the maximum to increase linearly with Z. However, as shown in Figure 1, the measurements of References 3 and 4 are in agreement for nitrogen. As a result, our treatment of Li ion SP in materials with $Z \geq 10$ uses the measurements where possible (i.e., cold SP), with a smooth connection to the cold SP calculations at high energy. Also we are trying to develop a computational approach that goes beyond the pwBa.

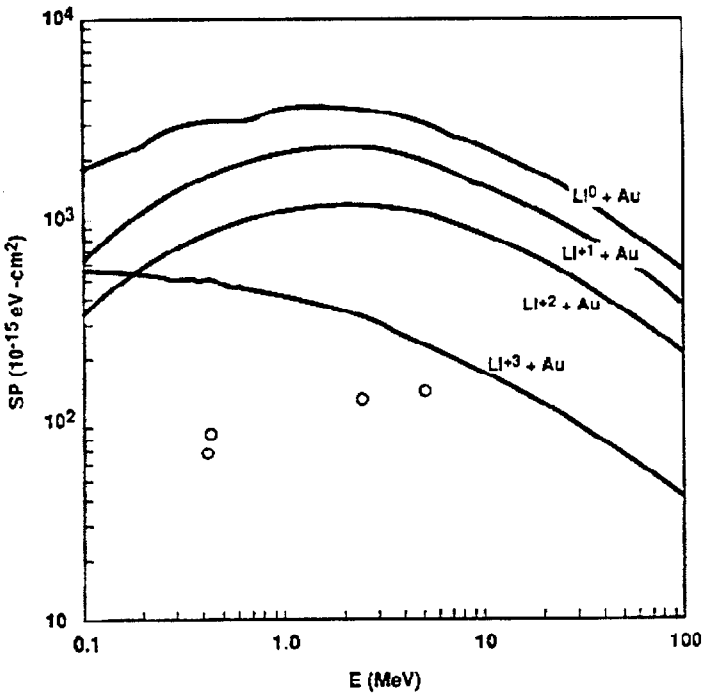

Figure 2. Comparison of calculated SP for Li on gold with the measurements of Teplova et al.[4] (open circles).

References

[1] D. R. Bates, in "Atomic and Molecular Processes," D. R. Bates, ed., (Academic Press, New York, 1962).
[2] E. J. McGuire, Laser and Particle Beams, 13, 321 (1995).
[3] S. K. Allison, D. Auton, and R. A. Morrison, Phys. Rev. 138, A688(1965).
[4] Ya. A. Teplova, V. S. Nikolaev, I. S. Dmitriev, and I.N. Fateeva, Zh. Eksp. Teor. Fiz. 42, 44(1962)[Sov. Phys.-JETP 15, 31(1962)].

7.4 Titanium Strip K- and L- shell Emission from MeV Li Ion Irradiation - E. J. McGuire

An analysis was performed for the Ti strips ("birdcage") used to monitor Li ion beam intensity and isotropy. The analysis, present in this section, is necessary for the characterization of the beam. Because of the possibility of significant energy loss in the Ti foil, a thick target analysis was required. The foil could be "optically thick" especially for the L-shell emission, and the analysis was done including the possibility of photon attenuation. A number of simplifying assumptions were made. First, it was assumed that the detector was on the z axis. Then, the intersection of the extrapolated foils and the z axis defined the origin of coordinates; the extrapolated foils made an angle θ with respect to the z axis. In reality, the detector was not on the axis, but it was assumed that the detector angle relative to the z axis was small compared to the cone angle, θ. The next section describes a procedure that can be used to analyze off-axis detectors. With this coordinate system the beam is incident from the x direction and the detector is located at (0, 0, z_0). The geometry is shown in Figure 1. It is assumed that the beam uniformly irradiates the Ti foil. The length of the Ti strip is L, its width transverse to the beam is W, and its thickness is T. The calculation was done in a coordinate system (X, Y, Z) centered on the foil. The distance from the origin of the old coordinate system to the new one is H + L/2. In the absence of attenuation the total number of K-shell fluorescence photons per unit area of the detector is

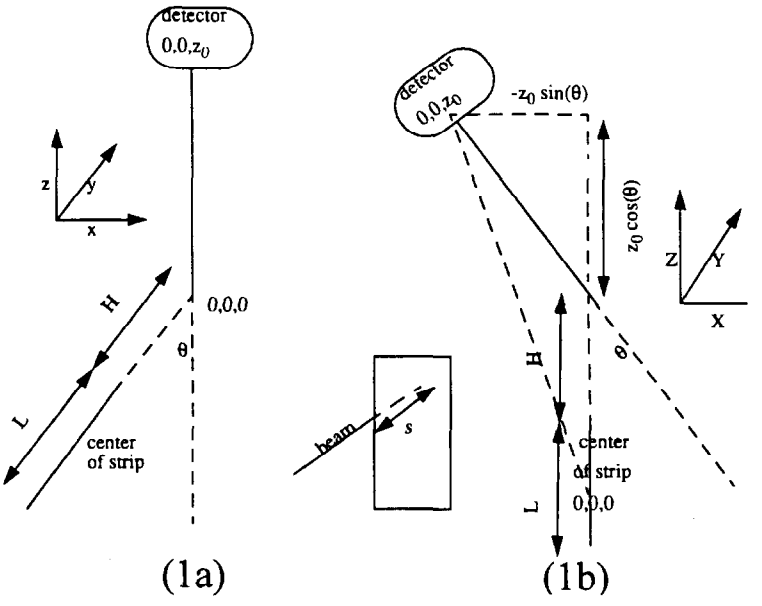

Figure 1. Coordinate systems used for the calculation inner-shell x-ray yields. (1a) Location of Ti strip with detector on-axis at (0, 0, Z_0). (1b) Off-axis detector.

$$J_d(z_0, \theta) = (\omega_k/4\pi)\, G, \tag{1a}$$

where

$$G = \int_{-L/2}^{L/2} dZ \int_{-W/2}^{W/2} dY \int_{-T/2}^{T/2} dX\, S(X, Y, Z)\,[z_0 \cos(\theta) + (H + L/2) - Z]\,/\,[D(X, Y, Z)]^3 \tag{1b}$$

$$D(X,Y,Z) = \{[z_0 \sin(\theta) + X]^2 + Y^2 + [z_0 \cos(\theta) + (H + L/2) - Z]^2\}^{1/2} \qquad (2)$$

Here, ω_K is the K-shell fluorescence yield, and the source function S(X,Y,Z), the rate of K-shell vacancy production, is given by

$$S(X,Y,Z) = \frac{dn_K}{dt} = \cos(\theta)\, I\,[E(X)]\, \sigma_K[E(X)] = S(X) \qquad (3)$$

where I is the flux of Li ions in number/cm^2-sec, and σ_K is the cross section for ionization and excitation of the Ti K-shell by a single Li ion of energy E(X). The problem becomes more complicated when attenuation must be taken into account.

To determine the source function we first determine the energy of the projectile as a function of its initial energy, E(0), on entering the foil, and its position in the foil, X. To determine this we need the stopping power (SP) for Li ions on Ti. Figure 2 shows calculations of the SP for various Li ions in Ti (see Section 7.3 on systematic ion-atom interactions) and the measurements of Teplova et al.[1] for Li ions on argon (open squares) and nickel (open circles). The surprising result is that the SP for argon appears to be higher although the Bethe formula suggests that SP is proportional to the number of electrons on the atom. Fortunately, as shall be shown, only the SP at high energy is important. A good fit to the Li^{+3} calculated SP is found with the function SP = $2.53 \times 10^{-13}/[E(MeV)]^{1/2}$ eV-cm^2. In this case, from the relation

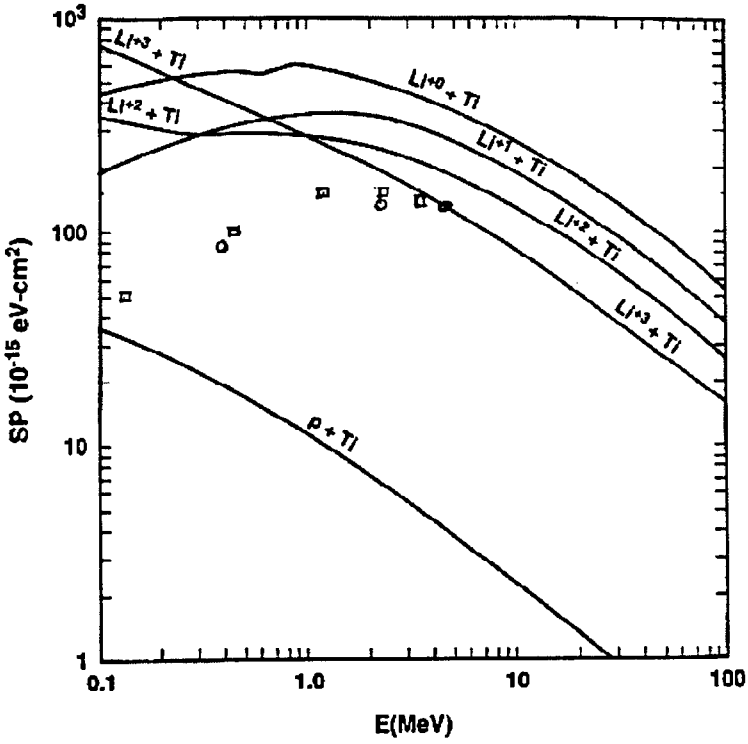

Figure 2. Comparison of calculated SP for Li on Titanium with the measurements of Teplova et al.[1] on argon (open squares) and nickel (open circles).

$$s\,n = \int_{E(s}^{E(0)} \frac{dE}{S(E)} \qquad (4)$$

where n is the target atom number density and s is the distance traveled by the projectile in the target, one has a relationship between projectile energy, E(s), and distance traveled,

$$E(s) = \{E^{3/2}(0) - 3C\,S\,n/2\}^{2/3}, \qquad (5)$$

where in this case, $C = 2.53 \times 10^{-13}$ eV-cm^2-MeV$^{1/2}$. The range energy relation is $R = 2\,E^{3/2}(0)/(3C\,n)$ found by setting E(s) = 0 in eq.(5).

Knowing the ion energy as a function of distance into the foil we next need the Ti K- shell ionization cross section as a function of Li ion beam energy. Figure 3 shows the K- and L- shell ionization cross sections for neutral Li (solid line) and Li^{+3} (dashed line), with open circles for Li^{+1} and open triangles for Li^{+2}. The figure illustrates several points: (1) the Ti L shell cross sections depend on the choice of ion charge state, while the K shell cross section is relatively insensitive to charge state; (2) the K- shell cross section is rising rapidly in the 1-10 MeV regime, so that if one is concerned with K-shell emission only, then only the high energy SP is significant; and (3) if one were using Ti L- shell emission, one would need a better model for SP. I approximate the K- shell ionization cross section out to 10 MeV by $\sigma_K(E) = 7\text{x}10^{-21}\,[E(\text{MeV})/10]^{2.5}$. Then, with J(0,t) the time-dependent incident ion current density and n the target atom number density, the source function becomes

$$\frac{dn_K}{dt} = n\,7\,10^{-21}[E\,(MeV)\,/\,(10\,MeV)]^{5/2}\,\{J(0,t)\,/\,[ev(0,t)]\}\,4.03\times10^{8}\,E(MeV)^{1/2} \tag{5a}$$

$$= (1.61\times10^{11}\{J(0,t)/[ev(0,t)]\}/(10\,MeV)^{5/2})\,[E(0,t)^{3/2} - 3C[(T/2 + X)/\cos(t)]n\,/\,2]^2 \tag{5b}$$

$$= (1.61\times10^{11}\{J(0,t)/[ev(0,t)]\}/(10\,MeV)^{5/2})\,[E(0,t)^{3/2} - 2.16\times10^{4}\,[(T/2 + X)/\cos(t)]]^2 \tag{5c}$$

$$= (1.61\times10^{11}\{J(0,t)/[ev(0,t)]\}/(10\,MeV)^{5/2})\,[A - BX]^2 \tag{5d}$$

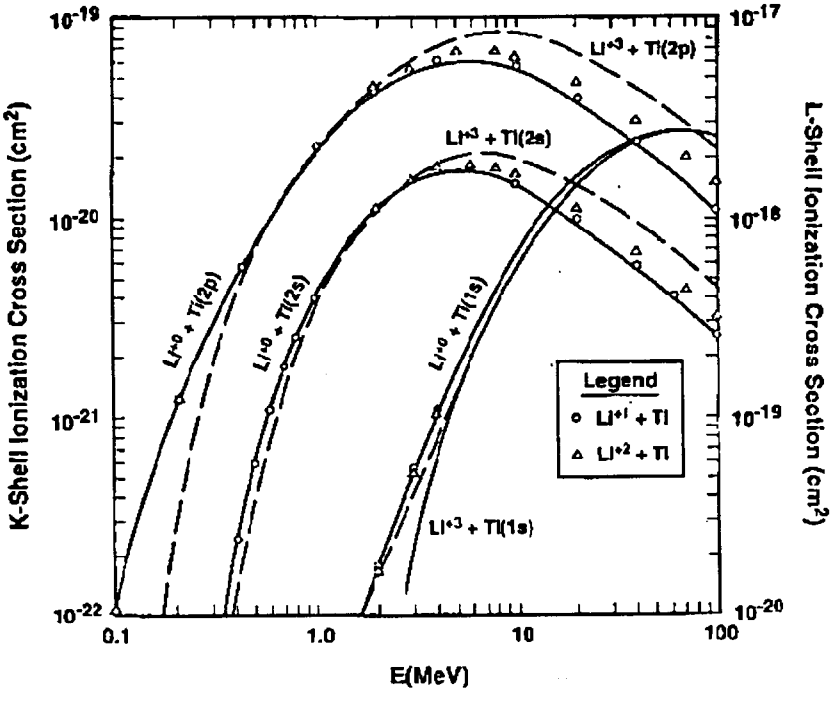

Figure 3. Calculated K- and L-shell ionization cross sections in Ti.

The calculation of attenuation of the emitted K shell x-rays is an exercise in conic sections if one assumes a straight line propagation path and neglects reemission of absorbed K-shell x-rays. That is, for a point detector the conic section divides the titanium foil into two regions: for one, all emitted x-rays emerge from the front of the foil, while for the other region all emitted x-rays emerge from the top of the foil. The conic section analysis can be found elsewhere[2]. The final result is

$$J_d(z_0, \theta) = F\,[H_3(z_0, \theta) + H_4(z_0, \theta)]\,, \tag{6a}$$

where

$$F = \{(\omega_K / 4\pi)\, W / [\alpha\, z_0^2]\}\; [1.90 \times 10^{22}\, J(0,t) / (10\ MeV)^{5/2}]\; [E(0,t)^4 / B] \tag{6b}$$

and

$$H_3(z_0, \theta) = (\cos(\theta))^2\,[1/3 - H] \tag{6c}$$

$$H_4(z_0, \theta) = \cos(\theta)\,\{\cos(\theta) + \alpha H[L - E(0,t)^{3/2}\cot(\theta)/B - (3/\alpha)\sin(\theta)]\} \tag{6d}$$

with

$$H = U[1 - 2U + 2U^2 - 2U^2 e^{(-1/U)}] \tag{6e}$$

and

$$U = B \sin(\theta) / [\alpha E(0,t)^{3/2}] = 2.16 \times 10^4 \tan(\theta) / [\alpha E(0,t)^{3/2}] \tag{6f}$$

Here, W is the width of the Ti foil, $B = 2.16 \times 10^4 / \cos(\theta)$, and $1/\alpha$ is the photon attenuation length.

Note the fourth power dependence of the signal on the Li beam kinetic energy. The signal will be very sensitive to the beam energy. Since the signal involves the product of current density and the fourth power of beam energy, the Ti strip K-shell emitter can be a sensitive detector of Li beam kinetic energy if there were an independent measurement of current density.

Note the complex dependence of the result on angle, incident energy, and the photon attenuation length, $1/\alpha$. For K-shell emission from Ti at 2.75 angstroms, I estimate the photoabsorption cross section as 9×10^{-21} cm^2. Then $\alpha = \sigma n = 513$/cm, and from eq. (6f) $U = 42.1 \tan(\theta)/E(0,t)^{3/2}$.

In Figure 4, I show the distribution in angle of $H_4(z_0,\theta)$ ($H_3(z_0,\theta)$ is negligible) for fixed energy with T = 0.05 cm, L = 0.6 cm, and z_0 = 500 cm (z_0 = is not relevant to the angular distribution). For the most part the structure of the curves can be accounted for by the limiting behavior of the parameter U. For θ approaching $\pi/2$, U is large, and H approaches 1/3, so that $H_4(z_0,\theta) = \alpha$ L cos(θ)/3 which is independent of the incident energy. This expression is plotted as the open circles in Figure 4. In the opposite limit θ approaches 0, U is small, H approaches U and $H_4(z_0,\theta)$ = B Lsin(q)/E(0,t)$^{3/2}$. Values of this expression at 6, 8, and 10 MeV are shown as triangles in Figure 4. As E(0,t) decreases at θ = 2.5 degrees, the approximation that U is small breaks down.

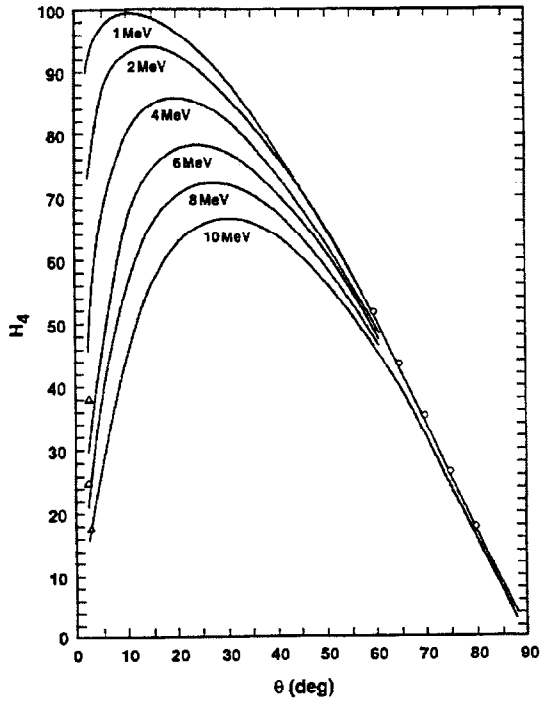

Figure 4. H_4 as a function of angle for various initial Li beam energies.

References

[1] Ya. A. Teplova, V. S. Nikolaev, I. S. Dmitriev, and I. N. Fateeva, Zh. Eksp. Teor. Fiz. 42, 44(1962)[Sov. Phys.-JETP 15, 31(1962)].

[2] E. J. McGuire (to be published).

7.5 L- and M- Shell Emission from Li Ion Beams Incident on Gold Cones - E. J. McGuire

The angular distribution of intensity of the Li ion beam in the PBFA-II barrel diode target experiments can be determined from the K-shell emission of thin Ti strips (preceding section).[1] For Li ions with energy below 10 MeV, the Ti K-shell emission depends on the fourth power of the Li ion energy. The simultaneous measurement of L- and M-shell emission from a gold cone measures Li ion energy and current density (averaged over angles). An iterative least squares fit to both the Ti and Au measurements provides an *in situ* measurement of incident beam intensity and angular distribution. The problem is complicated in that both detectors are displaced from the cone axis. Here I report on calculations of the L- and M- shell fluorescence emission from the gold cone, both numerically (integrating over ρ, ϕ, and z), and semi-analytically (integrating analytically over ρ and z, but numerically over ϕ). The consistency of the two approaches provides some confidence in the calculated accuracy. As the system is not yet experimentally calibrated the calculations provide a calibration. In addition, the reduction in computer time for the semi-analytical calculation will reduce, in the future, the computer time for generating the above-mentioned best fits.

The calculations would be relatively simple if, in addition to the gold cones being thin relative to the range of the Li beams, they were thin to the emitted L- and M-shell photons. This is not the case, and the calculation is done for arbitrary thickness. I do make the assumption that the cone angle relative to the vertical is large and the detector angle relative to the vertical is small so that the radiation detected comes through either the outer side or the top of the cone and, on a straight line path, does not cross an inner surface. Even with the straight line path approximation, the boundaries, separating the emission regions whose photons pass through the sides from regions whose photons pass through the top are complicated conic sections. Furthermore, the L and M-shell ionization cross sections and stopping powers are functions of the Li ion beam energy. In practice the beam is also not mono-energetic. This expression must be transformed into an expression for cross section and stopping power as a function of position to determine an emission source function. Finally, for tractable analytic calculations the cross sections and stopping power are approximated as polynomials over various energy intervals.

The geometry is shown in the sketch of Figure 1. In coordinates centered on the apex of the cone, the detector is located at $(x, y, z) = (x_d, y_d, z_d)$. In the sketch an ion that enters the cone with energy E_0 and has traveled a distance s has energy E(s) where E(s), is the solution to the integral equation

$$sn = \int_{E(s)}^{E_0} dE \,/\, S(E) \quad , \tag{1}$$

where n is the number density of Au atoms, and S(E) is the stopping power of Au for the appropriate Li ion. Assuming that the Li beam is incident radially, s is measured in the radial direction in cylindrical coordinates assuming an angular distribution which is time-

independent. Because we are using a conic annulus the boundaries are not separable in cylindrical coordinates; that is, in cylindrical coordinates a point in the cone may be labeled by (ρ, ϕ, z), where $0 \le \phi \le 2\pi$, but, with θ_0 the cone angle in the figure, the minimum z value, z_s, and the maximum z value, z_b, are given by

$$z_s = -(H + L)\cos(\theta_0) \le z \le -H\cos(\theta_0) = z_b, \qquad (2a)$$

while the inner and outer radial boundaries of the cone depend on z and are given by

$$\rho_s(z) = |z|\tan(\theta_0) - (t/2)/\cos(\theta_0) \le \rho \le |z|\tan(\theta_0) + (t/2)/\cos(\theta_0) = \rho_b(z) \qquad (2b)$$

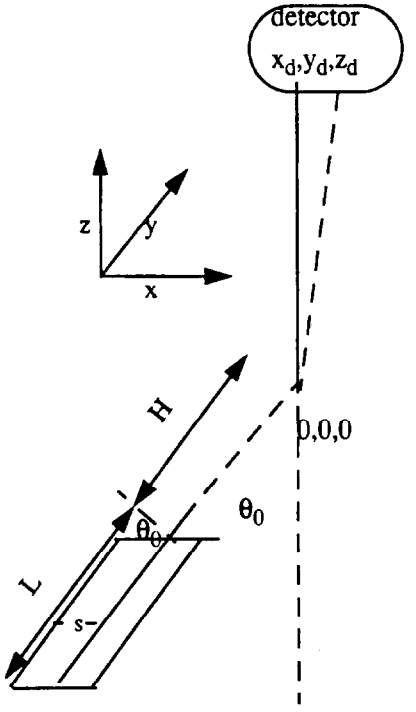

Figure 1. Geometry of the calculation.

Then E(s) = E[ρ_b (z) - ρ]. The rate of subshell vacancy production is

$$S_i(\rho, \phi, z) = \frac{dn}{dt} = \cos(\theta) / \{E[\rho_b - \rho]\}\ \sigma_i\{E[\rho_b - \rho]\} = S_i[\rho_b - \rho], \qquad (3)$$

where I is the flux of Li ions in number/cm^2-sec, and σ_i is the cross section for ionization and excitation of the ith subshell of Au by a single Li ion of energy E(X). In the absence of attenuation the fraction of the emitted intensity produced in the cone at (ρ, ϕ, z) reaching the detector, per unit area of the detector, is

$$(\omega_i / 4\pi)\, S\, (\rho_b - \rho)\, (z_d - z)/[D(\rho,\varphi,z)]^3, \qquad (4a)$$

where ω_i is the ith subshell fluorescence yield, and

$$D(\rho, \phi, z) = \{(x_d - x)^2 + y_d - y)^2 + (z_d - z)^2\}^{1/2} \qquad (4b)$$

with $x = \rho\cos(\phi)$ and $y = \rho\sin(\phi)$. In the absence of attenuation of the emitted x rays, the total number of fluorescence photons per unit area of the detector is

$$J_i(z_0, \theta) = (\omega_i/4\pi) \int_{z_s}^{z} dz \int_{\rho_s(z)}^{\rho_b(z)} \rho d\rho \int_0^{2\pi} d\varphi S(\rho_b - \rho)(z_d - z)/[D(\rho,\varphi,z)]^3 \qquad (5)$$

As was discussed for the case of the Ti strips, including photon attenuation introduces a complicated discussion of conic sections. The conic sections divide the cone into regions whose emitted x-rays emerge through the side or the top of the cone. This can be found elsewhere.[2] In determining the source function one needs the stopping power of Au for Li ions. In Figure 2 in Section 7.3 it was shown that the calculated SP for Li ions on Au did not agree with the measurements of Teplova et al.[3] Since the results are very different, I use the experimental values, and approximate the stopping power by,

$$SP(eV - cm^2) = A\,E^{1/4} \tag{6}$$

where $A = 0.956 \times 10^{-13}$ eV-cm^2 /(MeV)$^{1/4}$ = 0.956×10^{-19} MeV-cm^2 /(MeV)$^{1/4}$. Since an Au density of 19.3 g/cm^3 corresponds to a number density of 5.9×10^{22} atoms/cm^3, then with the approximate SP of 10^{-13} eV-cm^2/atom the energy lost is 5900 MeV/cm. In this crude picture a Li ion of energy E(MeV) has an approximate range of E(MeV)/5900 cm. A 10 MeV Li ion will be stopped in 17.0 microns of Au. One can show, for the above SP expression proportional to $E^{1/4}$, that the range R is given by

$$R = [E(o)]^{3/4} / [3An_0 / 4], \tag{7a}$$

which for a 1-MeV Li beam is

$$R = (10)^{3/4} / [(5.9 \times 10^{22})(0.956 \times 10^{-19})(3/4)] = 1.33 \times 10^{-3}\,cm = 13.3\ microns \tag{7b}$$

which is in good agreement with the crude estimate. The time required to stop an ion is found to be 11 picoseconds, so that the stopping is instantaneous. To model the gold target emission we need a space-dependent source function. For the above SP, the relationship between projectile energy, E(s), and distance traveled is

$$E(s) = [(E(0)^{3/4} - (3/4)An_o s]^{4/3} = [(3/4)An_o]^{4/3}\,[R-s]^{4/3} = [E(0) / R^{4/3}][R - s]^{4/3}, \tag{8}$$

where $s = \rho_b - \rho$. The projectile velocity in the target is

$$v(s) = [2E(s) / M]^{1/2} = [2 / M]^{1/2}\,[E(0)^{3/4} - (3/4)An_o s]^{2/3} \tag{9}$$

and the rate of production of ith-shell vacancies is

$$\frac{dn_i}{dt} = n\,\sigma_i[E(\rho_b - \rho,t)]\,[J(0,t) / e]\,[v(\rho_b - \rho,t) / v(0,t)], \tag{10}$$

where J(0,t) is the ion current incident on the Au foil, v(0,t) is the incident ion velocity, $E(\rho_b - \rho,t)$ is given by Eq.(8), $v(\rho_b - \rho,t)$ is given by Eq.(9), and σ_i is the sum of i^{th}-shell ionization and excitation cross sections. In Figures 2 and 3, I show calculated Au L- and M- shell ionization cross sections for various Li ions. For ionization of any of the subshells the Li^{+0}, Li^{+1}, Li^{+2}, and Li^{+3} results are almost identical.

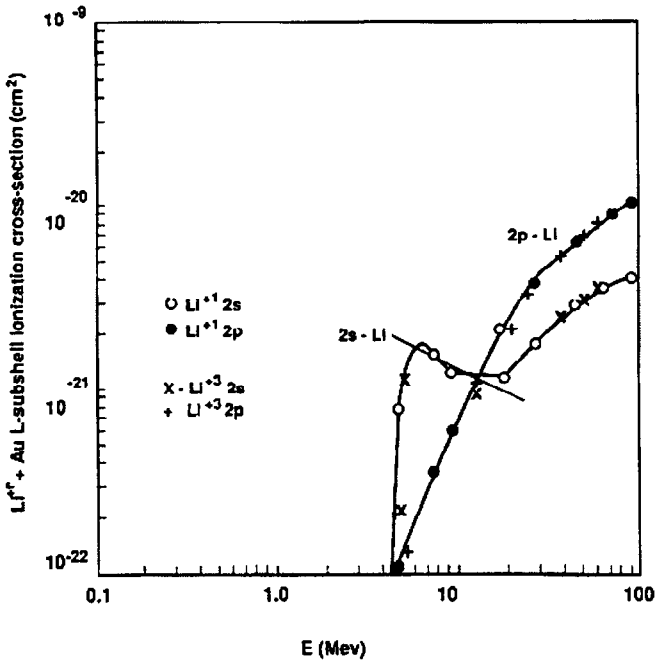

Figure 2. Calculated L-shell ionization cross sections in Au. The solid curves are for neutral Li.

For the L shell the L_1-M_2 and L_1-M_3 transitions are 11203 eV and 11610 eV, respectively; the L_2-M_4 transition is at 11443 eV; while the L_3-M_4 and L_3-M_5 transitions are at 9533 and 9623 eV, respectively.[4] Henke et al.[5] lists the L_{III} absorption edge as 11919 eV, so all these vacancies should fluoresce with a low attenuation coefficient; Henke et al.[5] list an attenuation coefficient of about 120 cm^2/g at 9600 eV, which corresponds to an attenuation of 2364/cm. For Au foils less than a micron in thickness, this is a small attenuation. The difficulty is the shape of the ionization cross section for the 2s subshell. The low energy structure is real. I approximate the 2s ionization cross section between 5 and 20 MeV by $\sigma_{2s} = 1.5 \times 10^{-21}\ \Theta(E-5)\ \Theta\ (20-E)\ (10MeV/E)^{1/2}\ cm^2$. I approximate the 2p ionization cross section by $\sigma_{2p} = 6.5 \times 10^{-22}\ [E(MeV)/10]^{5/2}\ cm^2$. The choice of exponents provides a reasonable fit to the data and is convenient for evaluating the integrals. It is clear that the 2s cross section is dominant, which is a surprise.

My calculations[7] of Auger and Coster-Kronig yields indicate $\omega_1 = 0.105$, $\omega_2 = 0.357$, $\omega_3 = 0.327$, $f_{12} = 0.083$, $f_{13} = 0.644$, and $f_{23} = 0.132$. Thus each L_1 subshell vacancy will produce $0.105 + 0.083 \times 0.357 + 0.644 \times 0.327 + 0.083 \times 0.132 \times 0.327 = 0.350$ L-shell x-ray photons. For both the 2s and 2p subshells I use a fluorescence yield of 0.350. Then, the L-shell source function as follows:

$$\frac{dn_L}{dt} = n_0[J(0,t)/e]\{E(s)/E(0)\}^{1/2}$$
$$(1.5\times10^{-21}\,\Theta[E(s)-5]\,[10/E(s)]^{1/2} + 6.5\times10^{-22}\,[E(s)/10]^{5/2}\Theta[E(s)])$$
$$= [J(0,t)/e]n_0$$
$$(1.5\times10^{-21}\Theta[E(s)-5]\,[10/E(0)]^{1/2} + 6.5\times10^{-22}E(s)^3\Theta[E(s)]/[E(0)^{1/2}10^{5/2}]) \quad (11a)$$

which is a polynomial integrand since

$$E(s)^3 = [E(0)^{3/4} - (3/4)An_0 s]^4 \quad (11b)$$

where

$$\rho[E(0)] = [E(0)^{3/4} - 5^{3/4}]/(3An_0/4) \quad (11c)$$

Explicitly, for the Au L-shell emission

$$\frac{dn_i}{dt} = n_0[J(0,t)/e](1.5\times10^{-21}\,[10/E(0)]^{1/2}\,\Theta\{\rho-\rho_b+\rho[E(0)]\}\,\Theta\,[E(0)-5]$$
$$+ 6.5\times10^{-22}[(3/4)\,An_0]^4\,[\rho-\rho_T]^4\,\Theta(\rho-\rho_T)/[E(0)^{1/2}10^{5/2}]) \quad (12a)$$

with

$$\rho_T = \rho - R \quad (12b)$$

where R is the range.

For the M shell the M_1-N_2 and M_1-N_3 transitions are 2781 eV and 2879 eV, respectively; the M_2-N_4 transition is at 2798 eV; the M_3-N_4 and M_3-N_5 transitions are at 2391 and 2409 eV; the M_4-N_6 transition is at 2204 eV; while the M_5-$N_{6,7}$ transition is at 2121 eV[4]. Henke et al.[5] lists the M_V absorption edge as 2205 eV, indicating that all the above transitions except the M_5-$N_{6,7}$ transition would be significantly attenuated. The M_4-N_6 transition, at 2204 eV is 1 eV lower than the Mv absorption edge. My calculations indicate that the M_{IV} width is 2.80 eV, which suggests that less than half the line would be attenuated. This is clearly a complex problem. I make the assumption that the M_4-N_6 line suffers no edge effect attenuation. For both the M_4-N_6 and M_5-$N_{6,7}$ lines I use an attenuation factor of 1000 cm^2/gm, which corresponds to an attenuation of 19700/cm. This is significant for foils greater than 1 micron in thickness. The fluorescence yield used is 0.0269. From Figure 3 I approximate the cross section by

$$\sigma M_{4,5} = 1.83\times10^{-20}\,[E(MeV)/1.3]^{5/2}\,\Theta(1.3-E) + \Theta[E-1.3]\,\Theta[3.7-E]$$
$$= 1.83\times10^{-20}\,[E(MeV)/1.3]^{7/4} + 11.4\times10^{-20}\,[E(MeV)/3.7]\,\theta\,(E-3.7) \quad (13)$$

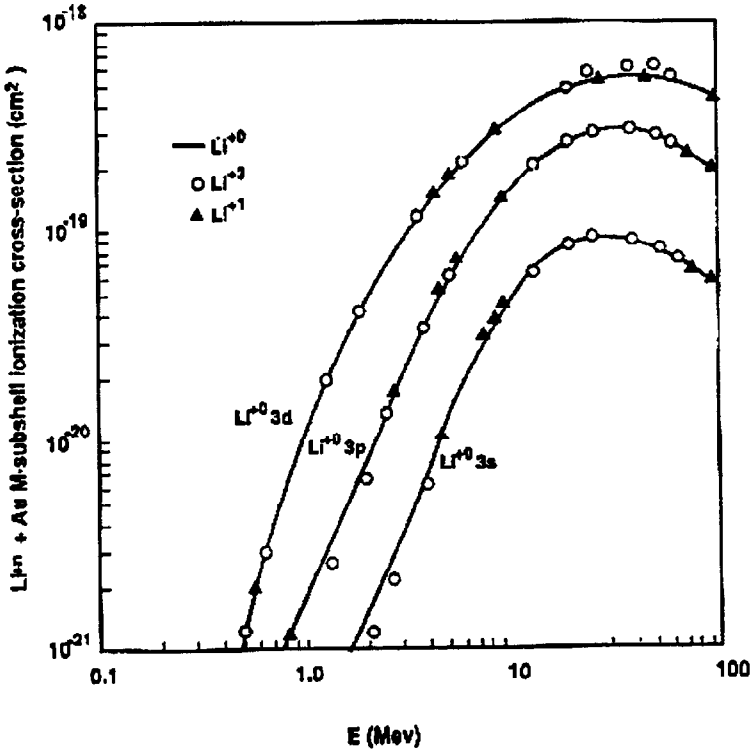

Figure 3. Calculated M shell ionization cross sections in Au.

Then the M-shell source function is given by

$$S = \frac{dn_M}{dt} = n_0 [J(0,t)/e] \{E(s)/E(0)\}^{1/2} \sigma_{M4,5}$$
$$= n_0 [J(0,t)/e] \{1/E(0)\}^{1/2} \{1.83 \times 10^{-20} E(s)^3 [1/1.13]^{5/2} \Theta(1.3 - E) + \Theta(E - 1.3)\Theta[3.7 - E] 1.83 \times 10^{-20} E(s)^{9/4} [1/1.13]^{7/4} + 11.4 \times 10^{-20} E(s)^{3/2} [1/3.7] \Theta[3.7 - E]\} \quad (14a)$$

which, with the projectile energy as a function of distance traveled given by Eq.(8), becomes

$$S = n_0 [J(0,t)/e] \{1/E(0)\}^{1/2} \Theta(R - s) \{1.83 \times 10^{-20} [E(0)^3/R^4][R - s]^4 [1/1.3]^{5/2} \Theta(1.3 - E) + \Theta(E - 1.3)\Theta[3.7 - E] 1.83 \times 10^{-20} [E(0)^{9/4}/R^3][R - s]^3 [1/1.13]^{7/4} + 11.4 \times 10^{-20} [E(0)^{3/2}/R^2][R - s]^2 [1/3.7] \Theta[3.7 - E]\} \quad (14b)$$

This equation exhibits the simple polynomial dependence that makes an analytical treatment possible.

For the cases treated the detector angle relative to the vertical was 7 degrees or 0.12217 rad. Neglecting terms on the order of the square of the tangent of the detector angle will introduce errors on the order of 1%. The numerical calculations were done on a 100 × 100 × 100 grid in ρ, ϕ, and z. For 20 Li ion beam energies, the L- and M-shell calculations took 50 s of Cray YMP time, 20 and 30 s, respectively. The cone has a radius at the top of 4 mm, a radius at the bottom of 2 mm, and a height of 6 mm, corresponding to a cone angle of 18.4 degrees. The distance from the zero point of the axis to the detector pinhole was 56.1 cm. Calculations were done for cone thicknesses of 0.5 and 1.0 microns. The calculated yields for the two cases are shown in Figure 4. For the M-shell case, the radiation mean free path is 0.5 microns, so that the increase in yield is negligible in going from 0.5 to 1.0 micron. In Figure 4 I show the M-shell yield for the 1.0 micron case, and the difference in the yields for the two cases. For the L-shell case there is a big jump in the yield between 5 and 6 MeV, due to the plateau in the 2s ionization cross section. The L-shell yield does not increase by a factor of two in doubling the thickness. The mean free path for L-shell photons is 4.2 microns.

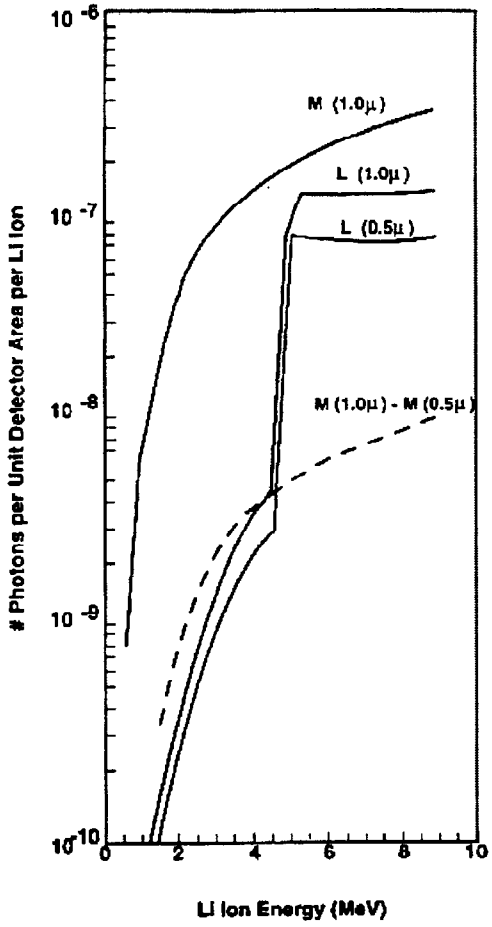

Figure 4. L-and M-shell yields for Li ions on Au cones of thickness 0.5 m and 1.0 m. Because the cone is optically thick for the M-shell, there is only a small difference in doubling the foil thickness; thus I show the difference in M-shell yield with foil thickness.

References

[1] A. R. Moats, M. S. Derzon, G. A. Chandler, R. J. Dukart, and T. A. Haill, Rev. Sci. Inst. 66, 743 (1995).
[2] E. J. McGuire (to be published).
[3] Ya.A. Teplova, V.S. Nikolaev, I.S. Dmitriev, and I.N. Fateeva, Zh. Eksp. Teor. Fiz. 42, 44(1962) [Sov. Phys.-JETP 15, 31(1962)].
[4] K. Siegbahn et al, "Electron Spectroscopy for Chemical Analysis", (Almqvist and Wiksells, Stockholm (1967).
[5] B. L. Henke, E. M. Gullikson, and J. C. Davis, Atomic Data 54, 181 (1993).
[6] E. J. McGuire, Phys. Rev. A22, 868 (1980).
[7] E. J. McGuire, Phys. Rev. A3, 587 (1971).
[8] E. J. McGuire, Phys. Rev. A5, 1043 (1972).

7.6 Upper Time-Integrated Thermal X-ray Camera Intensity Analysis - M. S. Derzon

Three time-integrated pinhole cameras viewed the soft x-ray emission out of the target from above (Section 7.7). The spectral sensitivity, calculated using XRDNEW, of each camera is shown in Figure 1. The Kodak 101-07 film used has a constant sensitivity below 1000 eV. The energy bands were chosen to roughly correspond to three channels of the energy-, space-, and time-resolved (EST) diagnostic and the x-ray diode (XRD) diagnostics. The camera acquired images on all shots. However, for a few shots the camera alignment was off and only part of the image was recorded.

On three of the eight full-power shots all the images were useful. On four more shots two of the three images were readable, the others had either damaged filters or film. On the last shot, two frames were saturated, and the third was misaligned.

A serious problem was found when analyzing the data. The amplitude scaling, based on the intensity obtained after correcting for pinhole size and filter, does not correlate with our preconceived ideas about the x-ray spectrum (Planckian) or other diagnostic measurements. This is shown by plotting the relative intensities of the different energy bins, scaled to the pinhole diameter, against one another. A monotonically changing curve is expected, regardless of which channel is plotted against another, as seen in Figure 2. For small variations, i.e., less than a factor of two (see Section 12) in beam energy into the target, emitted radiation should also vary by less than a factor of two and the relationship between intensities measured should be roughly linear. As the plots in Figure 2 show, there is no simple relationship between camera intensities. Based on this, we do not believe that there is useful information in the absolute amplitudes of the analyzed images.

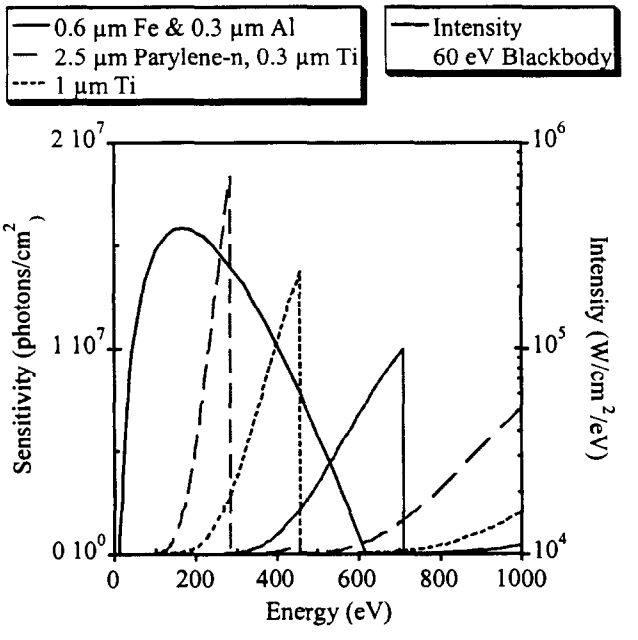

Figure 1. Calculated spectral sensitivity for the upper time-integrated camera (filter transmission x film sensitivity) and 60-eV blackbody intensity.

We discuss a few of the more likely explanations. The film is old (3-6 years, stored in a freezer) hence each strip is slightly different (the sensitivity varies). We believe this is the most likely cause of the problem because the film fog varied between shots. The second possibility was some problem with the film development, in spite of the effort to develop each piece the same and to the specifications described by Henke.[1] The film unfold to x-ray intensity is very dependent on the film fog and the bremsstrahlung background from the machine. The sum of these was observed to vary significantly between shots. The pinhole sizes were carefully checked prior to each shot and error in pinhole size is not believed to be a cause of this amplitude problem.

The footprints, meaning the spatial pattern of the unfolded intensity in the images, are similar across the energy spectra. This implies that the footprints are an accurate reflection of the relative x-ray intensities from point to point in the source. These footprints will be discussed in Section 9.

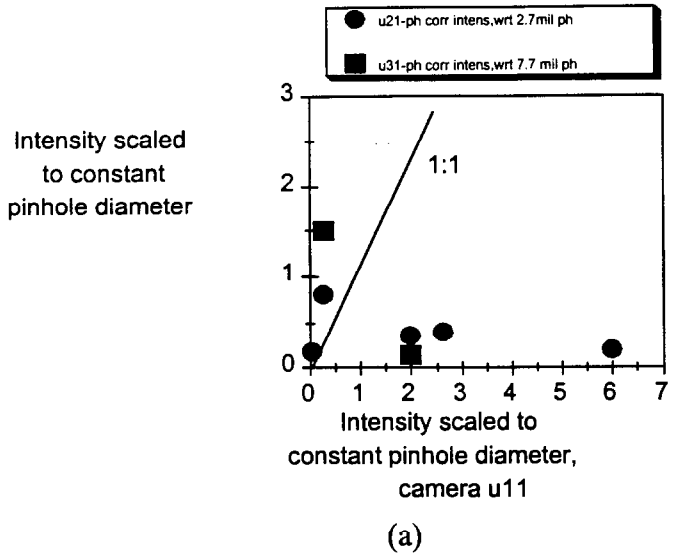

(a)

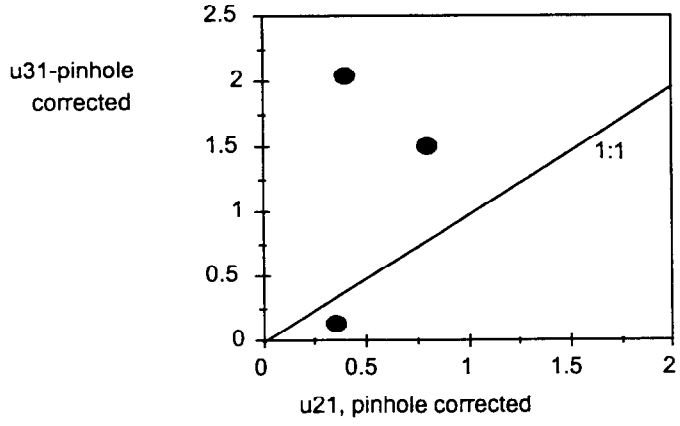

(b)

Figure 2. Pinhole-corrected relative intensity comparisons. Each point represents a given shot. Three images were not acquired on each shot. Camera u11 was filtered for the 200-300 eV region, u21 for the 300-450 eV region, and u31 for the 500-700 eV region.

Reference

[1] B. L. Henke, F. G. Fujiwara, M. A. Tester, C. H. Dittmore, M. A. Palmer, J. Opt. Soc. B, Vol. *1*, 828(1984)

7.7 Energy-, Space-, and Time-Resolved Thermal X-ray Diagnostic (EST) - T. L. Barber

A one-dimensional x-ray imaging diagnostic with six spectral bands was fielded to determine the size of the effective aperture as a function of energy and time.[1,2] The energy-, space-, and time-resolved (EST) diagnostic shown in Figure 1 uses a slit aperture to image the emission onto a fiber-optic faceplate coated with x-ray filters and a thin coat of scintillator (nominally 2 μm of BC 418,[3] see Section 7.9). The faceplate was placed against a linear array of optical fibers that carry the spatial information to the streak camera input. The faceplate is used for these reasons: to control scintillator thickness and uniformity, to protect the fiber array from debris,

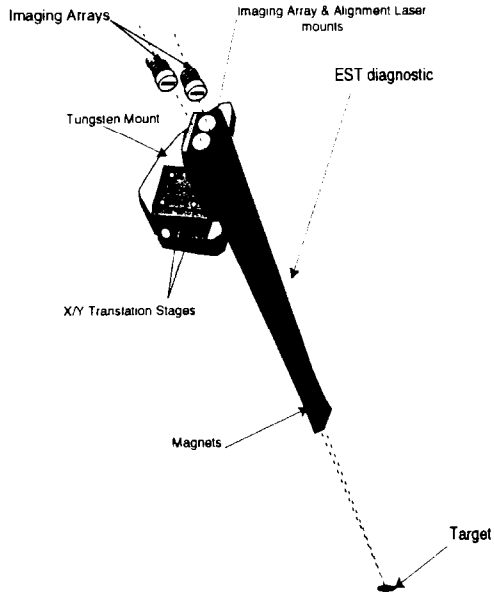

Figure 1. EST imaging assembly and alignment hardware.

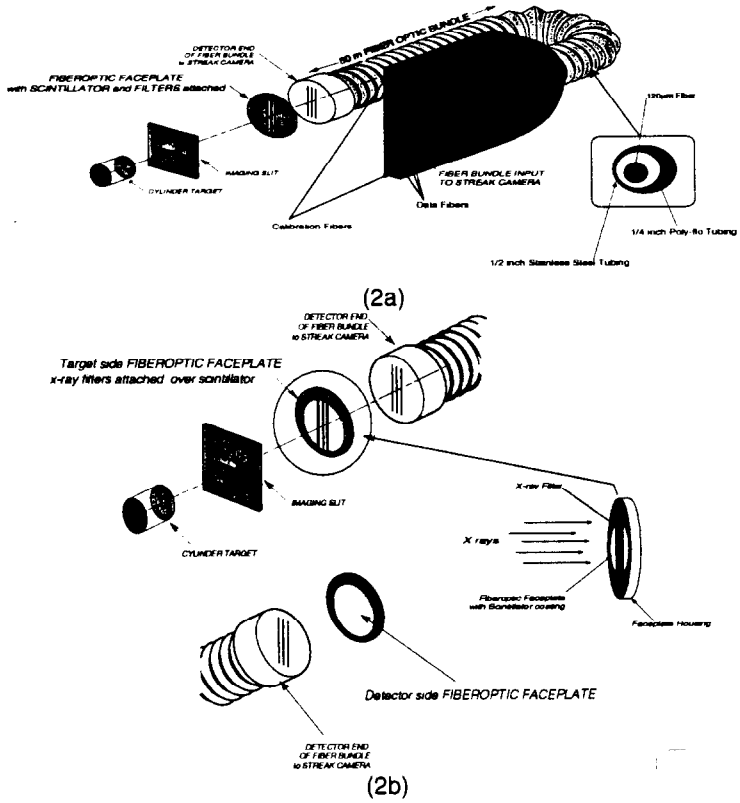

and to ease replacement when adjusting the x-ray sensitivities. Once the systems are calibrated with a steady state x-ray source, the faceplate will also provide absolute x-ray yields. The light exiting the fiber optics was focused onto a streak camera photocathode slit,[4] and the streak camera output is lens-coupled to a charge-coupled device (CCD) camera. The locations of the components are shown in Figures 2a and 2b.

Figure 2. EST components: (a) Schematic representation of EST diagnostic assembly. (b) Illustration of x-ray filters and scintillator with respect to detector end of fiber bundle.

The thickness of the scintillator coating and the x-ray coating on the fiber-optic faceplate determined the energy resolution. Some examples of calculated responses are shown in Figure 3. We fielded the EST diagnostic as three linear arrays with distinct spectral responses. Two systems were fielded simultaneously on our experiments for a total of six energy bands with peak sensitivities below 1000 eV.

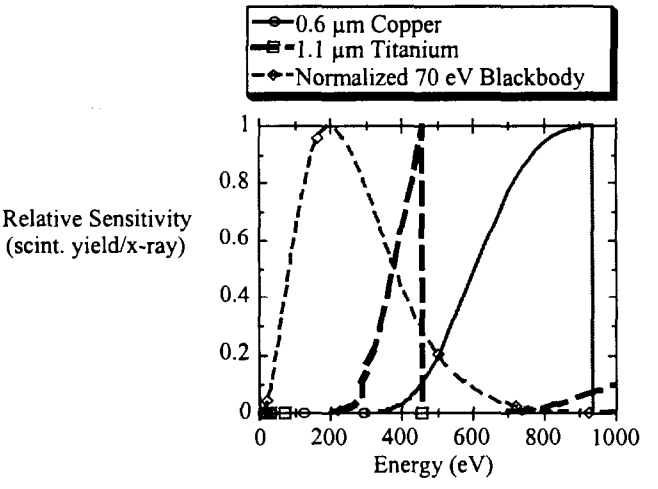

Figure 3. Estimated responses for x-ray filter coatings.

Each fiber bundle was made of 120-μm-diameter-core multimode fibers. Each systems' fiber bundle is coupled to its own streak camera/CCD camera system via an interface or 'patch' panel. At the top and bottom of the streak camera input bundle are two fibers that carry calibration data. The three imaging arrays are in the center of the bundle, as shown in Figure 2a.

Alignment of the EST diagnostic assembly was done by using an x /y translation stage and an alignment laser focused to a 150-μm spot. The laser was attached to the EST assembly at the detect and then focused through a pinhole onto the center of the target. After the alignment was complete, the lasers were removed and the EST imaging array was attached.

Characterization of the diagnostic systems

An approximately uniform source at the fiber inputs was generated by placing a strobe (output 2.5 cm in diameter) 60 cm from the diagnostic input. The acquired image was rotated 88.5 degrees with software to allow the time and pixel axis to be oriented to the right because the alignment hardware mechanism does not allow this rotation. The image (Figure 4) shows the three separate fiber arrays, fiber-to-fiber variations in transmission, slight gain variation with time, and two timing calibration features. The two timing calibration features are a 250-MHz comb signal and an optical pulse fiducial to establish the relative and absolute timing of the PBFA II shot with respect to the x-ray emission.

Each fiber optic bundle includes two fibers at each end of the streak camera input for timing calibration and test purposes. We inject both an impulse and an optical comb into the streak camera system. The impulse is a single ~500 ps full width at half maximum (FWHM) pulse of visible light, while the comb is a continuous train of these

pulses with peaks separated by 4 ns. These inputs allow us to compare absolute timing with regard to PBFA-II timing and calibrate the time scale of the diagnostic. These calibration signals are present on each data acquisition. An example of the calibration outputs is given in Figure 4. The comb trace is seen as the dotted line, and the impulse is seen as the bright point at the bottom of Figure 4.

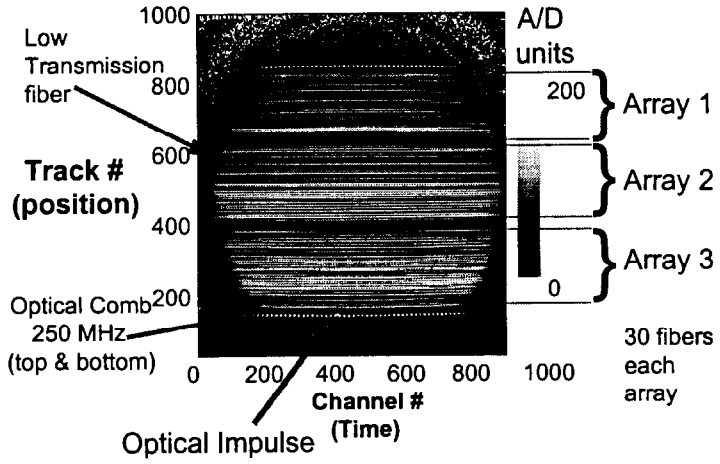

Figure 4. Uniform field source image showing the timing and output features of the diagnostic. Comb and impulse timing marks calibrate the time scale. Brightness changes illustrate gain variations over the field of view. A/D units refer to the uncalibrated value of the charge collected per pixel in the CCD.

In addition to the characterization described in reference 1, we have recently been able to measure the flat, or uniform, field sensitivity of the faceplate when exposed to x-ray radiation as well as the point spread function of the visible light generated in the scintillator that is emitted from the faceplate. This was done using a pulsed laser to generate an x-ray source to illuminate selected faceplates. The laser source consisted of an 800-picosecond-wide pulse from a frequency-tripled Nd:YAG laser. Energy output from the laser was 2 joules. The laser beam, focused to <100 μm in diameter, impinged on a molybdenum target that radiated an x-ray continuum up to 1 keV in energy and lines up to 2.4 keV in energy based on measurements made with a crystal spectrometer. The faceplates were placed 16 inches away from the x-ray source so that the source would irradiate the faceplate uniformly. The visible emission off the back of the faceplates was imaged using a fast lens and a CCD.

The lens which viewed the faceplate was known to exhibit appreciable vignetting for 400-nm light, and the extent of this vignetting needed to be measured before one can interpret the uniformity of the x-ray sensitivity. A uniform spectral source of known power, which approximated the emission spectrum of the BC418, was created with an integrating sphere and a 400 nm bandpass filter. The source was then placed at the focal point of the lens and an image taken (see Figure 5a). This image was then used to

normalize the image of the scintillator light out the back of the faceplate (see Figure 5b). The unfolded image (Figure 5c) is then the vignett-corrected image. A lineout, shown in Section 7.9 and reproduced here as Figure 6, illustrates the results obtained to date. There is roughly 5% scatter in signal amplitude at the peak emission and a 20% drop in emitted light at the edge of the lineout. There is some scatter in the data, which may be due to the low signal level acquired or some small-scale non-uniformities. The drop at the outer portions of the lineouts may be from the approximate nature of the vignetting correction (spectral match of the light source out of the integrating sphere) compared to that of the scintillator. Either way the uniformity needs to be understood in greater detail to reach our long-term goal for this diagnostic (1% uniformity). However, for the results presented in Chapter 10 the image extended over approximately 4-mm of the faceplate and less than 20% total variation in uniformity is expected in the portion of the faceplate that is used. The effect is accounted for in the uncertainty.

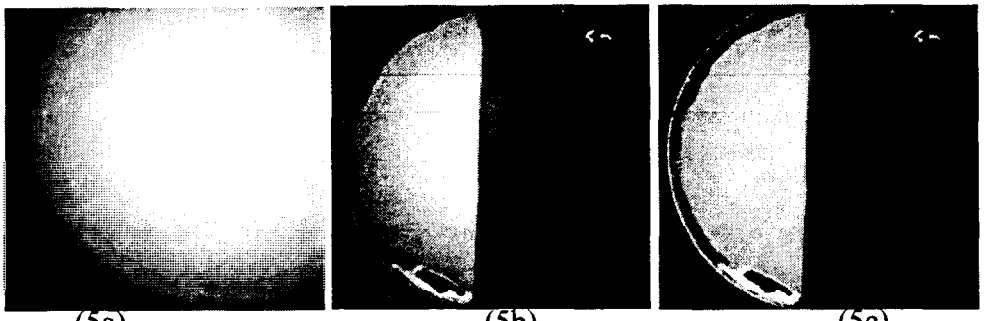

Figure 5. Vignett correction process for visible emission from scintillator coated faceplate. (a) Image of uniform source, (b) Raw image of faceplate, (c) vignett corrected image.

A factor in the interpretation of this data is that the point spread function of the visible light at the back of the faceplate must be less than the spacing between the optical fibers. An edge spread function was created in the image shown in Figure 5 by placing a sheet of titanium opaque to the x-rays in close proximity to the scintillator. By taking a lineout across the edge we can determine the width of the edge spread function to be ~100 μm, including the effect of camera and lens resolutions. This is much less than the ~300-μm spacing between fibers; hence each fiber observes a unique signal at the source.

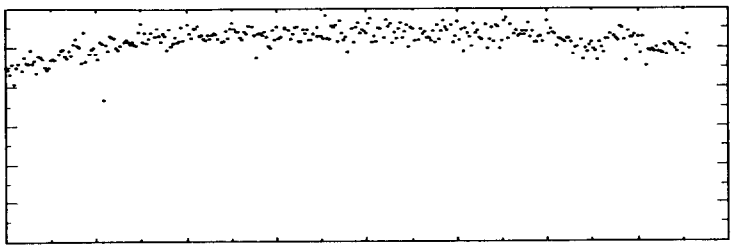

Figure 6. Vertical lineout near center of x-ray image.

In addition to instrument characterization described elsewhere, we are developing the tools to make this a well-characterized diagnostic. We can now obtain x-ray uniformities for individual faceplates that can be combined with the fiber- and streak-camera visible flatfields to give system uniformities. Future work will include absolute x-ray calibration, temporal impulse response, reproducibility and dynamic range measurements.

References

[1] M. S. Derzon, A. B. Filuk, J. Pantuso, R. J. Dukart, R. W. Olsen, T. Barber, M. A. Bernard, SPIE Proceedings, vol. 2002, p.31 (1993).
[2] M. S. Derzon, et al., Rev. Sci. Instr. **63**, 5068(1992).
[3] Bicron, 12345 Kinsman Road, Newbury, Ohio, 44065.
[4] Allied Signal - Amador Valley Operations and Kirtland Operations.

7.8 Fiber-based Intensity Diagnostic (FBI) - T. L. Barber

The Fiber Based Intensity (FBI) diagnostic, Figure 1 views the Ti wires. The instrument which works as a broadband x-ray spectrometer uses six x-ray filters to select spectral bands, and the x-rays are converted to visible light in a scintillator (same method as in the EST diagnostic). It uses multiple fibers with similar filters to increase data throughput and reliability. A 32-fiber detector array was used to acquire the data. There were a total of 6 energy bands using 5 fibers each. The 5 fibers of each energy group were patched into a 32 fiber-distribution panel and linear array.

The FBI's ultimate purpose is to provide a time dependent measurement of beam voltage and current near the target axis when two materials are employed in the target (see Sections 7.4 and 7.5). The voltage and current of the beam can be determined from the ratio of innershell line intensities, which is voltage dependent. The FBI diagnostic hardware is different than the EST hardware in that it does not have a slit for imaging or a scintillator coated on a fiber optic faceplate. In place of the fiber optic faceplate the FBI used thick x-ray filter pack that had the scintillator film directly attached with glue at the edges of the faceplate. Integrating the x-ray yield in space and sweeping in time provides a broadband spectrum analogous to the PIN (p-i-n semiconductor diode) spectrometer.

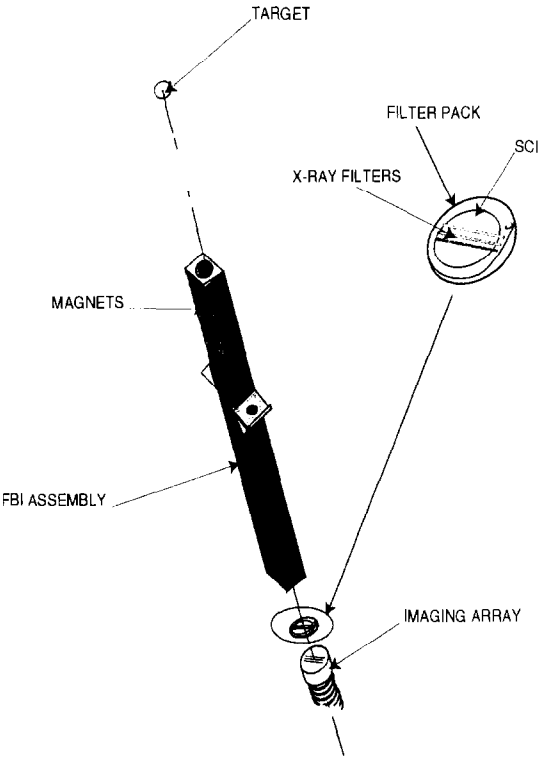

Figure 1. FBI Imaging assembly and filter pack. Three fiber arrays, two filters per array for six total energy cuts.

The goals of this first fielding of the FBI instrument were more modest than its ultimate purpose. Our initial goals were to obtain signal-to-noise measurements and determine if there are conceptual problems with the instrument.

There were many untested components and concepts when this diagnostic was first conceived and a more leisurely pace anticipated for its development. The diagnostic was developed late in the planning for the experiment, when it was learned that the p-i-n array

fielded in the past was incompatible with the other diagnostics. Obtaining a simple time FWHM of the beam near the axis (off the Ti-wire array) was deemed enough motivation for this diagnostic.

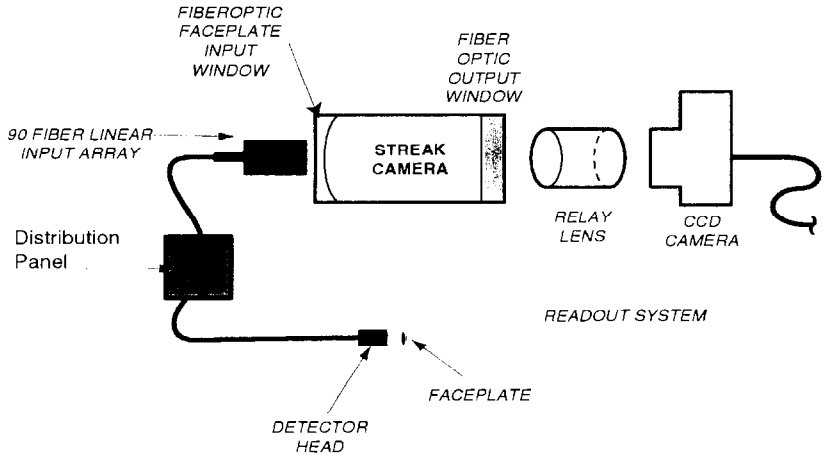

Figure 2. Typical setup for the EST and FBI diagnostics.

The EST and FBI diagnostics (Figure 2) have common features in that the hardware used for both consisted of an x-ray filter, scintillator, fibers and a streak camera. The emission from the scintillator/x-ray filter is coupled to a linear array of optical fibers. The array was then focused onto an EG&G [2] 50 mm S-20 photocathode streak camera with a fiber optic faceplate input window. The streak camera had better than 40 lp/mm static output resolution and was used with a Tinsley[7] f/0.58 lens coupled to a Photometrics Camera with a 1024x1024 Thompson CCD to acquire the data. As shown in Figure 3, the Nyquist limit of the Tinsley/CCD recording system is 12 lp/mm (Ref.SAND94-1840).

The quality of the unfolded information will be strongly dependent on the point spread function of visible light emission through the faceplate, the uniformity of the filters and scintillator. Characterization of these factors are underway. For now, however, we are reporting on the instruments nominal x-ray imaging performance and the parameters of the streak camera recording systems. Each of the diagnostics were recorded using three separate streak camera / ccd / lens setups, as shown in Table 1.

Table 1. Recording system configuration.

DIAGNOSTIC	LENS	CCD	INTENSIFIER
EST-1	*Tinsley M = 2.5:1,5%*	*Photometrics CH220 Front illuminated Thompson 1024x1024 16 bit D/A 20μm pixel*	*None*
EST-2	*Tinsley M = 2.5:1, 5%*	*Photometrics CH220 Front illuminated Thompson 1024x1024 12 bit D/A 20μm pixel*	*Yes*
FBI	*Nikon M = 1:1,<1%* **Estimated Mag& Overall Transmission**	*Princeton Instruments Back illuminated Tektronics 1024x1024 24μm pixel*	*Yes*

An example of the data is shown in Figure 3.

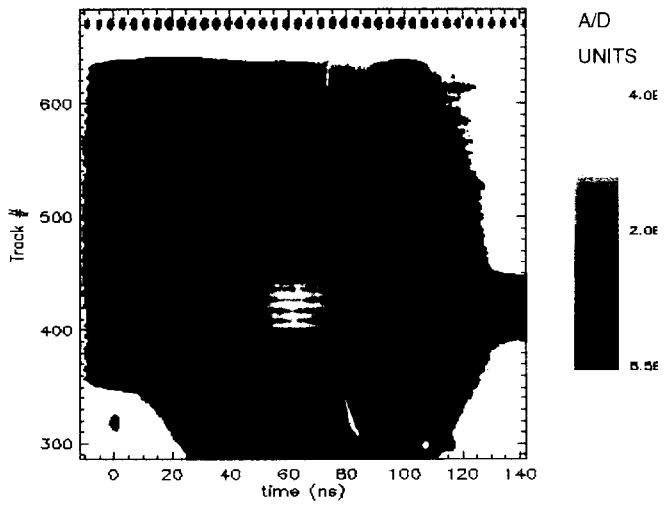

Figure 3. Raw FBI data.

The data were virtually useless in this configuration. The bright region from tracks 400-500 and time ~55-90 ns is believed to be due to relatively soft x-rays (<1.5 keV), produced by inner-shell aluminum radiation. As such, the pulse width gives an idea of the total beam temporal width hitting the Al coated target holder. Because the beam can sweep and even very low energy ions will excite this radiation, it is reasonable to obtain the long pulse width observed (25 ns), but it says little about the beam hitting the target. The signals of interest occur in tracks numbered ~500-800, however. Because of a tail to the point spread function in the instrument the much lower signal from Ti K-shell emission cannot be separated from the larger soft x-ray signal. This problem can be resolved in future work.

Some of the problems encountered and that are being corrected include alignment and noise. On the Li 94 target series, the EST alignment was done by using focusing lasers through a pinhole/slit as described. For future experiments, the EST hardware has been redesigned to accommodate an autocollomating telescope for a more accurate alignment to the target. The FBI hardware has been redesigned to utilize the same telescope foralignment. In the EST diagnostic, unwanted signal is generated by bremsstrahlung interactions with the fiber itself and the scintillator. When the scintillator is 2 μm thick there is little interaction; however, the FBI had 200-μm-thick scintillator and therefore 100x more bremsstrahlung-induced noise. This was a much larger problem than we expected. In the future these items will be addressed in the prefielding stages for each diagnostic.

References

[1] Bicron, 12345 Kinsman Road, Newbury, Ohio, 44065
[2] Allied Signal - Amador Valley Operations and Kirtland Operations.

7.9 Scintillator Coatings for the EST Diagnostic - D. K. Derzon

Introduction

Thin uniform coatings of a fast decay scintillator were required for the energy-, space-, and time-resolved (EST) diagnostic.[1] Existing methods of evaporatively coating the scintillator to nominally 2-micron thickness yielded films with uniformities of 10% standard deviation. This was inadequate. The desired uniformity, 1% standard deviation over an 8 mm length, was achieved by spin coating the scintillator onto the faceplates. Details of the evaporative coating process, the spin coating process, and characterization results will be discussed.

Evaporative Coating Process

Thin scintillator coatings nominally 2 microns thick were desired. The scintillator, Pilot U, was purchased from NE Technology in liquid form dissolved in xylene. Instructions from NE Technology for making thin coatings included diluting the dissolved scintillator further, syringing a known quantity onto the substrate, and then evaporating off the xylene. Several attempts were made using this method with little success. Although coatings were obtained, the yield was very low and the uniformity worse than desired. Initial coatings were made in a fume hood, but dust contamination was a large problem. All subsequent coatings were done in an EACI Envirco class 100 laminar flow hood. Use of the flow hood greatly decreased particle contamination but did not increase the yield significantly.

Pitfalls with this method included coatings that were too thin, coatings with dust particles because the evaporation times were long, coatings with large non-uniformities that could not be linked to any processing parameter and coatings with skewed thicknesses because the faceplates were not exactly level while the coatings were done. A typical coating by this method exhibited a 10% standard deviation from nominal thickness along an 8 mm length. Because the uniformity was unacceptable and the yield was so low, spin coating of the scintillator was investigated.

Spin Coating Process

The faceplates were cleaned initially in an ultrasonic cleaner in acetone and then in methanol in a fume hood. A final cleaning was done in the flow hood by wiping the faceplates with lint-free wipers soaked with ethanol. Care was taken to remove any dust particles using compressed CO_2 before coating. Pilot U was syringed directly out of the manufacturer's bottle using a 2 cc syringe and 18 gauge needle. The concentration of Pilot U was 10% in xylene. A faceplate was placed on a spin coater and enough Pilot U was syringed onto the faceplate to wet the entire surface over an area of ~ 30 mm^2. This was approximately three drops from the syringe. Spin speeds and times for the spin coater were 935 rpm or 1300 rpm for 2.5 minutes.

Initial coatings were made with spin speeds of 935 rpm and yielded coatings of nominally 2.9 μm. At this time a set of films were made using 0.20, 0.25, and 0.4 cc of 10% Pilot U as the starting amount of solution on the faceplate to see if initial quantity made a difference in final thickness. No obvious trend was found. Later coatings were made with slightly faster spin speeds of 1300 rpm in order to make a thinner final coating. All of the spin coated films described in this report were made using 1300 rpm. This spin speed yielded slightly thinner film thicknesses of nominally 2.7 μm.

Spin coating of the Pilot U consistently yielded films that were uniform to the eye. These coatings were made by syringing the Pilot U onto the faceplate and spinning the faceplate until most or all of the xylene evaporated off. Then, the coated faceplate was left sitting in the flow hood for at least 20 minutes, preferably 4 hours, in order to allow the residual xylene to evaporate off and the coating to harden fully. All spin coatings were done with the spin coater inside the flow hood in order to avoid dust particle contamination. The yield for this method was high, and bad films were easily cleaned off and recoated within 15 minutes.

Characterization and Discussion

All coatings were characterized for thickness using either a Sloan DEKTAK II or Veeco-Sloan Technology DEKTAK 8000 profilometer. Thickness scans of typical coatings by both processes are shown in Figure 1. The mean thickness for the evaporatively coated film along the 8 mm length of interest is 2.91 μm with a standard deviation of 0.3%. The minimum and maximum are 2.38 μm and 3.36 μm, respectively. The mean thickness for the spin coated film along the 8 mm length of interest is 2.69 μm with a standard deviation of 0.025%. The minimum and maximum are 2.62 μm and 2.94 μm, respectively. The large maximum observed as a spike in the trace is probably from a dust particle. The spin coating method produces a much more uniform coating than the evaporative coating method and meets the requirement of a 1% standard deviation in uniformity.

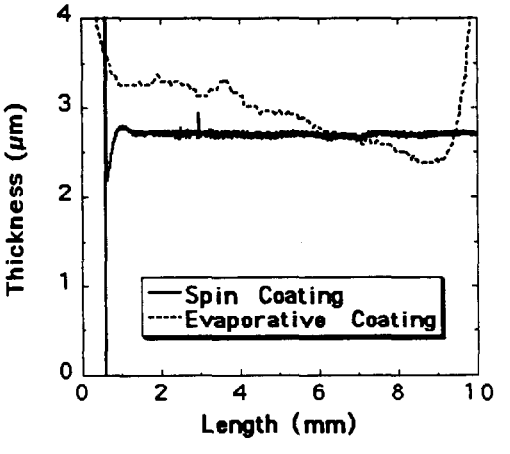

Figure 1. Comparison of film thicknesses of evaporatively coated and spin coated films of Pilot U.

The goal of this work was to create a coating with a uniform x-ray sensitivity. The first step was to spin coat a uniform coating. The second was to characterize the x-ray sensitivity. Initial attempts were made at characterizing the faceplates in the x-ray region. This was done using a pulsed laser to generate an x-ray source to illuminate selected faceplates. The laser source consisted of an 800 picosecond wide pulse from a frequency tripled Nd:YAG laser. Energy output from the laser was 2 joules. The laser beam, focused to <100 μm diameter, impinged on a molybdenum target that radiated an x-ray continuum up to 1 keV in energy and lines up to 2.4 keV, based on measurements with a gas proportional counter. The faceplates were placed 16 inches away from the x-ray source so that the source would irradiate the faceplate uniformly. The visible emission off the back of the faceplates was imaged using a fast lens and a CCD. See Section 7.8 for details.

A lineout of the scintillator emission generated from the x-rays incident on a typical faceplate is shown in Figure 2. This corresponds to the spin coating scan in Figure 1. Both the profilometer scan and the x-ray calibration output trace are taken from the general 8 mm length of interest on the faceplate, but are not from exactly the same locations. The trace in Figure 2 is centered with respect to the optical center of the faceplate. This data shows lots of scatter and a loss of signal at the edges. The random fluctuations near the peak emission are 5% rms, and the deterministic trend in the data goes from a mean near 0 mm of 270 A/D units to 220 A/D units near -5 mm, ~20%. The term A/D units refers to the linear scale readout of the CCD camera, which is uncalibrated. It is unclear how much of the 'random' fluctuation is from the CCD and how much is from the coating. These deviations are unacceptable. We have hypothesized some reasons for the deterministic trend and believe it is an artifact of the unfold process. Both can be studied and we believe improved. Clearly, more work needs to be done in this area.

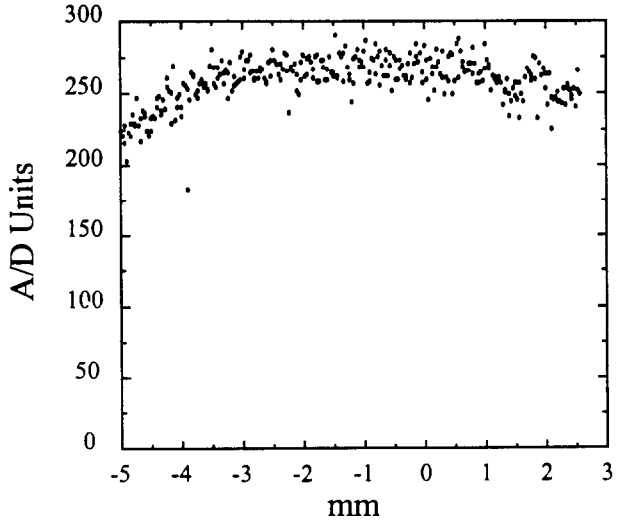

Figure 2. X-ray calibration output of faceplate 3.

Results

Scintillator coatings with less than a 1% standard deviation in mean thickness were made using spin coating techniques. Although final thicknesses were slightly higher than desired, attaining thiner coatings should be easily accomplished by using faster spin speeds.

Initial attempts at x-ray calibration of the coated faceplates show ~5% scatter and signal fall off at the edges. More work needs to be done in order to determine the source of the scatter and signal falloff.

References

[1] M. S. Derzon, A. B. Filuk, J. Pantuso, R. J. Dukart, R. W. Olsen, T. Barber, M. A. Bernard, SPIE Proceedings, vol. 2002, p.31 (1993).

7.10 Active Shock Breakout Diagnostic Prototype for Measuring Radiation Temperature - D. Noack

Introduction

A diagnostic that uses the breakout of a shock at the surface of a well-characterized material to estimate the temperature in the hohlraum was developed for the Li-94 Target Series. The velocity, D(cm/μs), of an ablatively-driven shock wave in an aluminum witness disk is related to the peak radiation temperature, T(eV), of the reaction driving the shock through the ablation pressure, P(Mbar).[1] We fielded a prototype of a laser-based Active Shock Breakout Diagnostic (ASBD) to measure shock wave velocity and compared the resulting radiation temperatures with those measured by other diagnostics. While a radiation temperature measurement was desirable, the main goal was to discover the strengths and weaknesses of the diagnostic technique.

Experiment Description

The elements of the ASBD included a modulated, continuous wave-6 W argon probe laser, a reflective aluminum disk mounted as the bottom endcap of the cylindrical hohlraum target, and a fast photodiode. The disk, measuring 5 mm in diameter, was coated with 2000Å of gold and backed by a washer to maintain disk flatness. A 2-mm diameter hole in the washer defined the active area of the aluminum disk. The radiation energy in the hohlraum ablated the inner, Au-plated surface of the disk, creating a shock wave which would then propagate through it and arrive at the outer surface which reflected the probe laser light. The shock-driven ablation of this surface caused a decrease in reflectivity estimated at a factor of 5 from previous calculations and measurements. In this case the disk was 100 μm thick on one side and 150 μm thick on the other side, creating a "step" so that the shock wave-driven ablation of the reflective surface might be observable at two discrete points in time. The surface-reflected laser light was then imaged by a 13 meter system of lenses and mirrors onto the face of a vacuum photodiode which had a risetime of 0.5 ns. At a peak radiation temperature of 60eV, it was estimated that the shock breakouts for the steps would occur at 24 ns and 29 ns after peak diode power. The photodiode would detect a maximum laser signal and two subsequent "drops" in that signal as each step lost reflectivity.

The Coherent Innova 70 argon ion probe laser was located in a remote location 25 meters from the target and focused to a 2.5 mm spot size nominally centered on the disk step. A triggered 1 ms, 2 -Hz shutter was used to modulate the laser beam, reducing laser heating of the target during alignment and protecting the photodiode from saturation or damage before and during the PBFA-II shots. Since conservation of probe laser power was necessary to maintain as high a signal to noise ratio (SNR) as possible, the argon laser was operated in the standard multiple line mode (seven wavelengths between 458 nm and 514 nm), and two edge filters with overlapping transmission ranges were employed at the photodiode to help limit light from the PBFA-II ion beam diode fluorescence. One filter transmitted 70% of the light up to 540 nm while the other transmitted 70% down to 490 nm. The photodiode signal was recorded on a PBFA-II

Data Acquisition System Tektronix model 640 digitizer and a back-up, Tektronix model 7104 oscilloscope.

The ASBD technique was not optimized in this diode, target, and optical hardware configuration. Although the data were not conclusive in determining radiation temperature and analysis has not answered all of the questions arising from our first use of this tool, the results offered some insights into the problem areas for a shock breakout diagnostic in this form and suggestions for future versions. Observations on the first use of this diagnostic are as follows:

(1) Digitizer traces recording the laser light loss indicated that the reduction in reflectivity from the ASB disk was approaching the predicted factor of five. However, diode fluorescence within the 50 nm range of the overlapping optical filters was detected by the photodiode and obscured the region where the reflected laser light level would have reached zero. The amplitude of what is believed to be diode fluorescence was about six times the laser light level. On PBFA-II shot 6551, laser light loss was not observed at all before diode fluorescence dominated the photodiode signal. A shot record of reflected laser light loss with respect to the time-shifted XRD signal is shown in Figure 1.

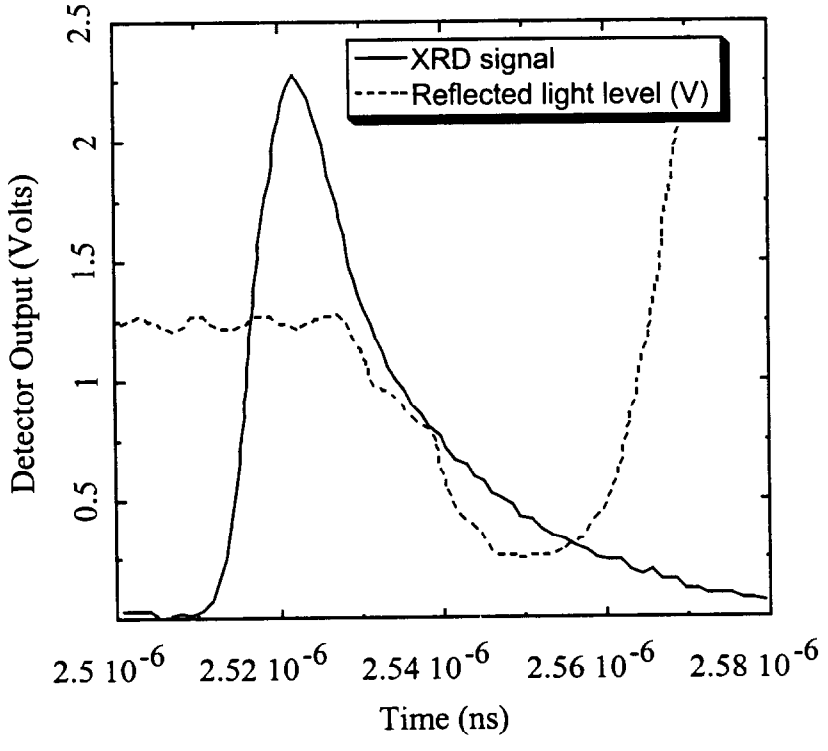

Figure 1. Reflected light level and XRD signal vs. time. (PBFA-II shot 6560)

(2) After photodiode and XRD signals were corrected for cabling and time-of-flight differences, we noticed that the beginning of laser light loss, corresponding to the ablation caused by the shock arrival at the surface or direct electron or ion deposition, was ≈20 ns earlier than the 24 ns predicted for the 100 μm thick step , or ≈6 ns after the XRD signal peak on PBFA-II shots 6547, 6554, and 6560.

(3) An unwelcomed laser artifact in the form of an ≈128 Mhz beat frequency had the potential of obscuring or confusing any step function in the laser light reduction from a "stepped" target disk. In addition, shock breakout times for the 150 μm steps could not be reliably determined because of the long falltimes (typically ≈22 ns) of the laser signals and the domination by diode fluorescence. These factors obscured data needed to determine shock velocities.

(4) Since the target disk was mounted at the bottom of the hohlraum target cylinder, we were concerned about possible direct ion beam preheating of the ASB disk. Preheating, which reduces the shock velocity in aluminum, would be a possible qualitative explanation for the very slow fall of the photodiode signal.

(5) The ASBD argon laser was modulated with a mechanical shutter with a 1ms open time at a frequency of 2 Hz in order to limit target heating during alignment. Most alignment was done at laser powers of 0.4 W, with the full 6 W laser power used only for final alignment. (Note that power levels at the target were an order of magnitude lower due to losses in the optical system.) Nevertheless, the possibility of laser heating of the ASB disk and, subsequently, of the foam inside the hohlraum was explored. Tests at atmosphere showed only a modest rise in target disk temperature, but in the PBFA II diode vacuum, lack of heat conduction away from the disk was suspected as a cause for longer laser signal falltimes and lower radiation temperatures measured by other diagnostics when the ASBD laser was in operation. During final alignments of the laser beam to the center of the target disk, some convergence/divergence effects, possibly due to target distortion from laser heating, appeared to occur in the target disk-reflected laser image when full laser power was applied, even when modulated.

Conclusions and Summary

The ASBD as configured for the Li-94 shot series confirmed that a reduction of the reflected laser signal could be observed in a radiatively-driven witness plate at the 60 eV level. It also pointed to a number of improvements needed to prevent the diagnostic from affecting ion beam/target interaction data. Since it appears that ion diode fluorescence occurs later than the shock breakout, SNR may be sufficient to again use an argon laser in the future. However, improvements would have to include electro-optic modulation to lower average laser power on target during alignment, single frequency laser output combined with a higher degree of wavelength discrimination at the detector, and a spatial aperture (slit) at the photodiode face for observing a 1-D section of the ASB disk. Plans were made to field this type of diagnostic on the SATURN accelerator with the following changes: (1) use of a single-shot, pulsed dye laser to greatly increase SNR and eliminate the need for mechanical shutters, cw laser noise, and the problem of target heating; (2) use of a 15 mW He-Ne laser to align the dye laser with the ASB target disk,

also avoiding the possibility of any target heating problems; (3) improvement of the optical relay and imaging system for better laser beam direction, centering, and imaging of the target disk; (4) use of an EG&G streak camera with a linear fiber optic array for streaking a 100-μm wide line of laser intensity across the image of the stepped target disk; and (5) the addition of laser intensity monitors both before and after laser reflection from the target to corroborate shock breakout information.

Reference

[1] R. Olson, SNL Internal Memo (March, 1994).

7.11 Neutron Time-of-Flight - C. L. Ruiz

The target experiment requires a good measurement of the lithium ion beam energy delivered by the diode. Typically, this quantity is measured by a two-step lithium-copper nuclear activation process. Part of the diode lithium beam (16%) is allowed to impinge on a thick (60 to 90 microns) erbium deuteride target (ErD_2). The lithium ions interact with the deuterium in the target by way of the $d(^7Li,n)^8Be$ reaction emitting energetic neutrons (14 MeV or greater). The neutrons produced at the source (target) impinge copper samples located at a fixed geometry relative to the ErD_2 target. Activation of copper is accomplished through the $^{63}Cu(n,2n)^{62}Cu$ reaction, leading to the beta decay of ^{62}Cu with a 9.74 minute half-life. Therefore, an estimate of the lithium beam ion energy delivered by the diode is made by counting the ^{62}Cu activity (counts/minutes). This technique, and the calibration, is described in detail elsewhere.[1]

The target shot series, because of geometry, placed serious constraints on the size and use of an erbium deuteride target. Typical erbium deuteride targets that give good sensitivity to lithium are 1.13 inches wide. The target series shot restricted widths to 0.28 inches and ruled out, because of sensitivity, the use of erbium deuteride. Further, any nearby placement of copper samples was prohibited because measuring lithium energies by the lithium-copper technique would be seriously compromised. To preserve this energy measurement a new technique has been devised. The reaction of lithium with deuterium produces neutrons into 4π steradians. We placed a collimated neutron detector[2] at a large distance (54 feet) from the source and detected the signal response of the scintillator plus photo-multiplier detector for these prompt neutrons. These neutrons arrive later than the bremsstralung produced by the PBFA-II accelerator and well separated in time by neutron time-of-flight (nTOF) affording unique identification. Thus, the nTOF technique allowed us to cross-calibrate the detector with the lithium-copper technique. First, on pre-target shots (6458 and 6466), we measured activity (counts/per minute) of ^{62}Cu and the response of the nTOF detector (in nanocoulombs) for erbium deuteride targets of normal size (1.13" wide by 1.6 " high). On the next shot (6469) we replaced the ErD_2 targets with similarly sized CD_2 targets but with increased activation sensitivity. For these three shots, nTOF prompt signals were recorded on 6880 LeCroy digitizers. We therefore cross-calibrated the sensitivity change (counts/min) in going from ErD_2 to CD_2 and the corresponding response (in nanocoulombs) of the nTOF detector. On the target series shots we measured only the nTOF responses and with the cross-calibrations were able to infer the lithium energy per shot. Results of cross-calibration measurements are shown in Table 1. In addition, the inferred total ion energy is listed. These estimates assume symmetry of the beam at approximately 5 cm radius and have an inherent error of 30 %. Table 2 contains the estimated energy in the ion beam for the target shots.

Table 1. Results from calibration shots.

Shot Number	Target	Activity (cpm)	Response (ncoul)	Energy (kJ)
6458	ErD_2	$2.5x10^6$	4.0	84
6466	ErD_2	$2.5x10^6$	4.0	96
6469	CD_2	$5.2x10^6$	10.0	96

Table 2. Results from thermal radiation target shots.

Shot Number	Lithium Ion-beam Energy (kJ)
6501	131
6517	103
6529	19
6547	116
6551	112
6554	121
6560	81
6569	80

References

[1] R. J. Leeper, K. H. Kim, D. E. Hebron, N. D. Wing, and E. Norbeck, Nuc. Instr. Meth. B 24/25, 695(1987).

[2] Model no. NPM-54, manufactured by EG&G, Las Vegas,Nevada.

7.12 Bolometers – Description and Analysis – G. A. Chandler

In this section we present a description and the results from an analysis of the two bolometer detectors used on this target series to measure the total soft x-ray radiation yield from our targets. After the results are given with a short discussion of the data, a comparison of the data with a previous target series using cone targets is given, followed by a detailed description of the experimental setup and of the detectors, which is then followed by a description of the data analysis. An appendix containing the equations describing the response of the bolometers is at the end of this section. **It should be noted however that these detectors are not calibrated and that we rely on using calculations based on the intrinsic response of the detectors.** The philosophy in fielding them is to see if there is consistency with the X-ray Diode Detectors, (XRDs), which are calibrated but sample the x-ray fluence from the target with a large spectral dependence and whose unfold is also more complex. Since the bolometers are believed to observe all of the soft x rays with a flat response (up to ~ 550 eV), they are a valuable diagnostic, complementary to the XRDs. In fact, for the previous PBFA-II Target series, the inferred temperatures between the XRDs and bolometers were in good agreement. As will be seen for this target series, the agreement between the detector systems is poor. The bolometers also allow us to look at shot-to-shot variations, as we expect the relative response to be more robust.

The principal behind these detectors is that a soft x-ray flux incident on a nickel resistive element will heat the element, changing its resistivity. The time to heat the element is very fast, of order ns, but the decay time for the temperature of the element is very long compared to our radiation pulses, of the order of μs, as is evident in the decay times for the voltage pulses. Thus, the bolometers act as integrating detectors for the radiation flux. If a constant current source is driven across the element, then by measuring the change in voltage across the element the change in the resistivity due to the photon flux can be measured and hence the total absorbed energy in the bolometer inferred as well as on the total radiated source flux and temperature. There are issues associated with the response of these detectors related to the nonuniform deposition of the x-rays into the element and the subsequent diffusion of the temperature profile created that are yet to be resolved. Nevertheless these types of detectors have been used as standard detectors for the soft x-ray fluence from radiation sources here at Sandia, and a comparison with the XRDs is insightful.

Results from the Bolometer Detectors

The results for this target series using the nominal response for these detectors and an error analysis, primarily using estimated values for the intrinsic variables describing the response for the detectors, is given in Table 1.

In this table the total energy radiated out of the top of the targets into 2π is listed along with a one-sigma error estimate. The peak brightness temperature corresponding to this energy output from a source with a circular aperture having the nominal diameter listed along with its 1 sigma error estimate, is also listed. Note that with the exception of

the 1st, 3rd, and 4th shots (shown with strike-thru characters in the table) all of the shots were nominally good machine shots. In looking at the three good target shots with a 3-mm diameter aperture, two- 2026 and 2033, showed similar radiation outputs. Shot 2029 has a significantly lower output for some reason. All three of the target shots with a 1.5-mm-diameter aperture were nominally good machine shots. Again, two of the shots, 2020 and 2032, had similar radiation outputs and one, 2031, had, for some reason, a significantly lower radiation output. It is interesting to see that on the four highest temperature shots two had a 3-mm aperture and the other two had a 1.5-mm aperture. **This would seem to indicate that hole closure is not an issue for these targets.**

Table 1. Results of the bolometer data for the PBFA-II 94-1 target series.

#	Target Shot #	DAS Shot #	Aperture Diameter (mm)	Energy into 2π (Joules)	± Error for Energy in 2π (Joules)	Peak Brightness Temp. (eV)	± Error in the Peak Temp. (eV)
~~1~~	~~2025~~	~~6501~~	~~3.0~~	~~759~~	~~130~~	~~50~~	~~2.4~~
2	2026	6517	3.0	2083	291	68	3.2
~~3~~	~~2027~~	~~6529~~	~~3.0~~	~~122~~	~~66~~	~~33~~	~~11.4~~
~~4~~	~~2028~~	~~6542~~	~~3.0~~	~~33~~	~~40~~	~~20~~	~~8.1~~
5	2029	6547	3.0	1387	214	59	2.9
6	2030	6551	1.5	606	97	68	4.9
7	2031	6554	1.5	393	107	59	7.4
8	2032	6560	1.5	531	102	67	5.0
9	2033	6569	3.0	1917	278	66	3.8

Comparisons with the Previous 93-1 Shot Series

It is valuable to compare this data with the data obtained on the previous 93-1 target series using cone targets. In Table 2 the energies obtained into 2π from an average of the unfiltered bolometers 2 and 3, from this run is listed. The same formula was used to unfold the data between the two runs. Except for shots 2018 and 2023 all the shots were nominally good machine shots. On shot 2020 the bottom inconel cathode tip shorted out ~ 2 μs before the machine pulse, however it appears to be a very good shot and so it was not put in the table with strike-thru characters. On shot 2015 approximately half the target appeared obscured by something. The questionable shots are shown with strike-thru characters in the table. The energy radiated from just the good shots show a large variation in output, ~ factors of 3 for the open cone target type. A detailed analysis of the images from the time-resolved x-ray pinhole camera show source size variations which ameliorate these differences in the specific energy radiated into 2π down to a factor of ~ 2. In fact there were large variations in the incident ion-beam intensity as inferred from the PIN detectors fielded to look at the ion induced x-rays from the target.

This has been written up by Derzon et al., "Shot to Shot comparison of the first Li-beam-driven hohlraum experiments," Review of Scientific Instruments, 1/95.

Table 2. Results of the bolometer data for the PBFA 93-1 target series.

#	Target Shot #	DAS Shot #	Aperture Diameter (mm)	Energy into 2π (Joules)	Specific Energy into 2π (J/cm^2)	Peak Brightness Temp. (eV)	Foam Density (mg/cc)	Gold Cone thickness (μm)
~~1~~	~~2015~~	~~5936~~	~~8.0~~	~~2721~~	~~8517~~	~~47.0~~	~~4.75~~	~~1.0~~
2	2016	5942	8.0	9055	21058	58.9	4.75	0.5
3	2017	5975	3.0	1344	12215	51.4	2.38	1.0
~~4~~	~~2018~~	~~5979~~	~~3.0~~	~~626~~	~~5691~~	~~42.5~~	~~2.38~~	~~1.0~~
5	2019	5984	8.0	1346	6119	43.1	2.38	0.5
6	2020	6000	8.0	6587	20585	58.6	4.75	1.0
7	2021	6010	8.0	2722	12374	51.6	4.75	0.5
8	2022	6014	8.0	2613	11360	50.5	4.75	1.0
~~9~~	~~2023~~	~~6017~~	~~3.0~~	~~248~~			~~2.38~~	~~1.0~~
10	2024	6022	8.0	4410	16962	55.8	2.38	1.0

With such variation it is hard to do a comparison with the present data but a simple attempt taking into account the variations in the target configurations will be made. In the 94-1 series the targets were 4-mm-tall cylinders with a 4-mm diameter and a 1.5- or 3.0-mm-diameter aperture in the top. The foam density used in the present series was nominally 5 mg/cc and the gold wall thickness was 1.5 μm. In the 93-1 series the targets were primarily truncated right circular cones 6 mm tall with an 8-mm diameter open end at the top and a 4-mm diameter open end on the bottom. Three of the targets were totally closed except for a 3-mm-diameter aperture in the top. To normalize out these differences we use a simplified analytic model of the target response used in the R. J. Dukart and J. Maenchen memo, "Analytical Modeling of Ion Beam Requirements for the August 1994 Goal; A presentation to the PBFAII intensity Team, May 19, 1993." In this report the power balance formula is given as:

$$\eta_f \eta_x P_{inc} = \frac{C \rho V T}{\Delta t A} + \frac{\sigma T^4 A_{ap}}{A} + \frac{\sigma T^4 A_{wall} (1 - \alpha)}{A} \qquad (1)$$

where:

η_f is the fraction of the beam power incident on the foam.

η_x is the x-ray conversion efficiency.

P_{inc} is the power intensity on the target.

C is the heat capacity of the foam. Nominal values for the heat capacity in J /(ev-gm) are - 1.3e5 for CH, 2.34e5 for H, and 6e4 for Au.

ρ is the density of the foam.

V is the foam volume.

A is the equivalent surface area of the hohlraum which intercepts the ion beam.

T is the radiation temperature of the hohlraum.

Δt is the FWHM of the ion beam pulse.

A_{ap} is the area of the aperture in the target.

A_{wall} is the area of the hohlraum wall.

α is the hohlraum wall albedo.

To come up with an estimate of the total flux measured by the bolometers between the cylinder and the cone targets it is useful to look at the ratio, **R**, of the flux out of the targets as seen by the bolometers:

$$R = \frac{T_{cy}^{\ 4}\, A_{ap\_d\_cy}}{T_{co}^{\ 4}\, A_{ap\_d\_co}} \tag{2}$$

where $\mathbf{A_{ap\_d\_}}$ is the area of the diagnostic aperture of the cylinder or cone target. T^4 is simply found from equation 1 if the heat capacity term is neglected. Hence the ratio of the temperatures to the fourth power for both targets, $\mathbf{R_T}$, can be given as:

$$R_T = \frac{T_{cy}^{\ 4}}{T_{co}^{\ 4}} = \frac{P_{inc\_cy}}{P_{inc\_co}} \frac{A_{cy}}{A_{co}} \frac{A_{ap\_co} + A_{wall\_co}\,(1-\alpha)}{A_{ap\_cy} + A_{wall\_cy}\,(1-\alpha)} \tag{3}$$

Table 3 lists the parameters for the open and closed cones and the cylinders with a 3-mm-diameter aperture used in the present experiments. The diagnostic aperture of the cone targets is considered to be just the top opening in the target.

Table 3. Parameters for the different targets used in the 93 and 94 experiments.

Parameter	Cylinder Target 94-1	Open Cone Target 93-1	Closed Cone Target 93-1
Radius-Bottom (cm):	0.2	0.2	0.2
Radius-Top (cm):	0.2	0.4	0.4
Height (cm):	0.4	0.6	0.6
Radius of Diagnostic aperture (cm):	0.15	0.4	0.15
Radius of other aperture (cm):	N/A	0.2	N/A
Effective Area for Beam Input (cm^2):	0.5	1.13	1.13
Area of hohlraum gold wall (cm^2):	0.683	1.191	1.75
Area of hohlraum apertures (cm^2):	0.071	0.628	0.071
Area of diagnostic apertures (cm^2):	0.071	0.503	0.071

Table 4 lists the calculated ratio of the flux out of the targets as seen by the bolometers for the cylinder vs cone targets for different ratios of the incident beam power using equations 2 and 3. An albedo of 0.8 was used in all cases.

Table 4. Calculated ratio of the flux from cylindrical to cone targets as a function of the ratio of the incident powers.

P_{inc_cy}/P_{inc_co}	$Flux_{cy}/Flux_{co\_open}$	$Flux_{cy}/Flux_{co\_closed}$
0.2	0.05	0.18
0.4	0.10	0.36
0.6	0.16	0.54
0.8	0.21	0.72
1.0	0.26	0.90
1.2	0.31	1.08
1.4	0.37	1.26
1.6	0.42	1.44
1.8	0.47	1.62
2.0	0.52	1.80

Comparing just the best shots the ratio of the energy emitted from the cylinder to the open cone is:

$$R = Energy\_cy\_2026/Energy\_co\_2016 = 0.23$$

and for the closed cone:

$$R = Energy\_cy\_2026/Energy\_co\_2017 = 1.55$$

The energy ratios for the bolometer measurements are comparable to the intensity ratios in the table since the emission times for the target types are ~ the same. These ratios indicate, when compared with Table 4, that the intensity on the cylinder for shot #2026 was approximately 90% of that on the best open cone target shot. For the closed cone target the ratio indicates that the beam intensity on the cylinder for shot # 2026 was 70% higher then on the cone. **The comparison of the cylinder to the open cone target is important because it indicates that the target performance was approximately what should have been expected for a similar beam intensity on the target. In fact the bolometer estimates of temperature do seem to scale nominally as expected between the two series for the best shots, from 58 eV to 68 eV.** It will be interesting to compare with a more detailed analysis including the heat capacity terms and LASNEX calculations. It will also be interesting to compare with a detailed analysis of the XRD data.

Two bolometer detectors were fielded on the TAR94-1 series, with one on each of the center lines of sight of the eleven channel detector arrays known as DAX1 and DAX2. These detector arrays are located on different line of sight pipes at 461 cm from the source. These same detectors, BOL1 and BOL2, have been fielded on all of the PBFA II hohlraum target series. The set of nickel bolometer detectors used on PBFA II target series up through the 94-1 target series were obtained from the Sandia Z-pinch program. The details of the design for these detectors can be found in an unpublished report by Dave L. Hanson at Sandia called "Users' Guide to the SNL Bolometer: A Time-Resolved Diagnostic for Soft X-ray Energy Measurements." The design of these detectors will be briefly discussed here.

The actual detector heads are shown schematically in Figure 1. They consists of an aperture plate which restricts the soft x-ray flux from the source to a defined area on the bolometer resistance element, which is nickel for both of these bolometers. A filter can be placed in the Coaxial shield of the detector, on the 94-1 target series the two bolometers were left unfiltered to observe to total x-ray flux from the source. The bolometer resistance elements were a thin nickel film, ~ 1 μm thick, deposited on a fused silica substrate. The fraction of the incident energy absorbed by the nickel element is shown in Figure 2. This substrate is then mounted on a macor substrate. A pair of ceramic magnets are mounted to the macor substrate providing ~ 500 gauss of traverse magnetic field, which suppresses photoelectric shunt currents that could seriously distort the bolometer signal. The macor substrate is then mounted into an HN connector.

Experimental Setup

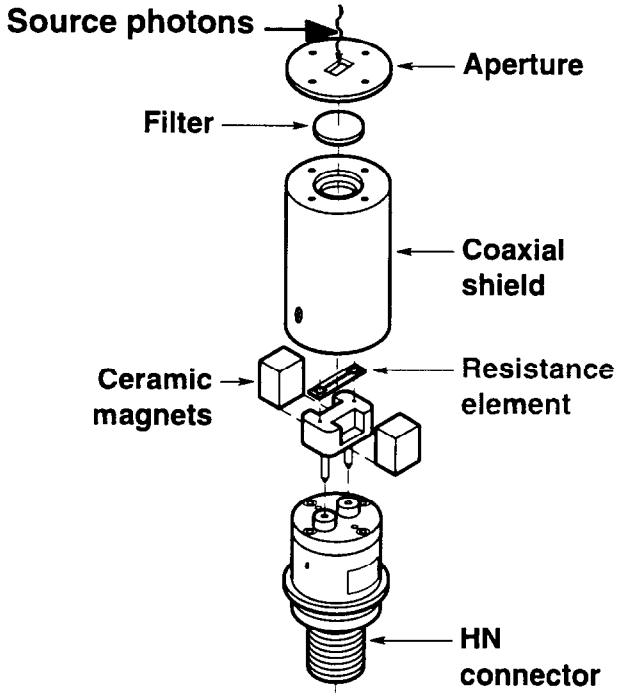

Figure 1. A bolometer detector

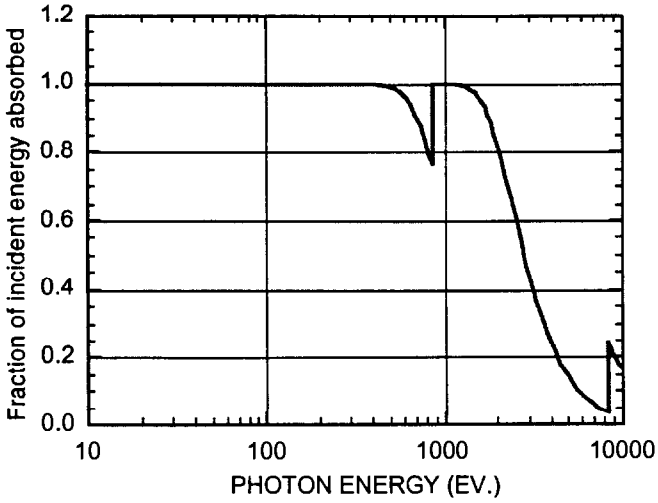

Figure 2. Bolometer sensitivity versus photon energy.

The detector is adapted down to an N connector to match the vacuum feedthru in the DAX housing assembly. A simple electrical tee, not a power tee, is attached to the outside of the DAX assemblies. A current drive cable is attached to one end of the tee and a signal cable is attached to the other end. Both the current and the signal cables are long (~ 157 ns from the high bay to DAS), 50 ohm, RG214 cables originating in the PBFA II DAS. The current drive cables from each of the bolometers were connected to their own Team Specialties Engineering pulsers and both the pulsers were driven by a Team Specialties Engineering power supply.

The signal cables monitor the volt-age drop across the bolometer element. In the PBFA II DAS the signal cable is split, using a power tee, so that the signal can be observed on both a slow and a fast time scale and with different amplitude sensitivities on two separate oscilloscopes. Thus for each bolometer there are two signal measurements. In addition the current output from each of the pulsers is monitored by separate scopes.

The energy emitted from the source into 2π is calculated for all four signals using equation A15 in the appendix describing the response of the bolometer element. **Again note that the energy emitted from the source is based on the theoretical response of the detector and not a calibrated detector response**. The peak temperature is then calculated for all four signals from the source energy measured using equation A20 in the appendix. As explained in the appendix, this equation assumes a Gaussian distribution of the radiation flux in time. To get a power from the source, which is required to get the temperature as indicated in equation A20, I use the full width at half maximum of a set of XRD signals. Differentiating the bolometer signals to get the source output power could also be done but the signal to noise level is poor, ~ 5 for the best signals. To unfold the peak source temperature the source area is also required and the nominal target aperture sizes have been used.

In order to come up with an error estimate for the energies and temperatures equations A21 and A22 in the appendix were used which are obtained from partial derivatives of the fundamental equations A15 and A20. The parameters and their respective error estimates are listed in Table 5. Note that except for three of the parameters used, the error estimates are all estimates of the standard deviations for the parameters. For the voltage, the current, and the full width at half maximum of the radiation pulse the standard deviations of the measurements yield the error. The values of these errors for shot 6569, which is representative of the data from a relatively strong signal seen during the shot series from a 3-mm aperture target, are shown.

The error in the source emission area is based on a nominal 100 μm error in the diameter specification. The tolerance on the part is 25 μm and the measurements of it are probably good to 10 μm from the optical comparater. Thus a 100 μm specification should be dominated by hole closure type issues and not the physical specification of the part.

Table 5. Error estimates for the bolometer response.

Parameter	±Error	% Error in Value	Source of error
Viewing Angle (deg)	3	0.8	Estimate
Source - Detector Distance (cm)	5	1.1	Estimate
Element Length (cm)	0.05	5.3	Estimate
Element Width (cm)	0.01	4.9	Estimate
Element Thickness (μm)	0.05	5.0	Estimate
Nickel density (g/cm^3)	0.89	10.0	Estimate
Specific Resistivity (ohm-cm/(Joule-gm))	1.0e-8	10.0	Estimate
Detector Voltage Jump (volts)	0.6	6.0	Shot 6569
Current measured (amps)	37	0.2	Shot 6569
Source emission area, 3.0 mm Target, (cm^2)	0.005	6.7	Estimate
Source emission area, 1.5 mm Target, (cm^2)	0.002	13.3	Estimate
FWHM of the Radiation Pulse (ns)	2.1	16.3	Shot 6569

To estimate a single temperature and a single error from the data on the TAR94-1 target series the following prescription is used. There are two bolometers for two completely independent measurements. There are two measurements per bolometer so that errors in obtaining the signal value from the digitizers can be averaged. In coming up with the errors from a given bolometer add in quadrature to the fixed errors the weighted average in the independent errors in the current and voltage. From these equations the weighted average for the measured voltage for a given bolometer, one from each of the fast and slow measurements, is given by[1]

$$\Delta V_{ave} = \frac{\Delta V_s \, \sigma_{vf}^2 + \Delta V_f \, \sigma_{vs}^2}{\sigma_{vf}^2 + \sigma_{vs}^2} \tag{4}$$

and the error in this average, σ_{v_ave}, is equal to:

$$\sigma_{v\_ave} = \frac{\sigma_{vf} \, \sigma_{vs}}{\sqrt{\sigma_{vf}^2 + \sigma_{vs}^2}} \tag{5}$$

The same equations hold for the weighted average for the current and its resulting standard deviation. Using these values for the current and voltage a single value for the energy and peak temperature for each bolometer detector is calculated using equations A15 and A20. The error in the measurements for each detector is again found from equations A21 and A22 and the errors listed in Table 1.

Using these results a weighted average source energy into 2π, $\mathbf{E_{src}}$, from both bolometers can be obtained as follows:

$$E_{src} = \frac{E_{src\_B1}\ \sigma_{E\_src\_b2}^{2} + E_{src\_B2}\ \sigma_{E\_src\_b1}^{2}}{\sigma_{E\_src\_b1}^{2} + \sigma_{E\_src\_b2}^{2}} \tag{6}$$

where $\mathbf{E_{src\_Bi}}$, is the total energy from the source into 2π found from bolometer #i, and $\mathbf{\sigma E\_src\_bi}$, is the standard deviation of the measurement for bolometer #i. Since the bolometers are on different lines of sight the errors in the observation angles and detector distances will be taken as independent. The errors in the detector element parameters will also be taken as independent. Thus all of the errors for the source output energy are taken as independent and the total error in E_{src} is given by $\mathbf{\sigma E\_src}$ as follows:

$$\sigma_{E\_src} = \frac{\sigma_{E\_src\_b1}\ \sigma_{E\_src\_b2}}{\sqrt{\sigma_{E\_src\_b1}^{2} + \sigma_{E\_src\_b2}^{2}}} \tag{7}$$

To come up with the peak temperature based on the two bolometers I can just use equation A20 with E_{src} replacing E_{src_tot}. To come up with the error estimate for the peak temperature based on both bolometers I will just use equation A22 where the source area and the full width at half maximum for the radiation pulse are not independent errors. Therefore a reduction in the error in the temperature from the independent measurements only comes about through a reduction in error in the source output.

Appendix - Response of the Bolometer Detectors

The differential change in the measured voltage across a bolometer element due to the change in the resistivity for a constant current source, **I**, is simply given as:

$$dV = I\,dR \tag{A1}$$

The change in the resistance, **dR**, is given in terms of the change in the resistivity, $\mathbf{d\rho}$, of the material from which the bolometer is manufactured as follows:

$$dR = \frac{l}{w\,t}\,d\rho \tag{A2}$$

where **l, w,** and **t** are respectively the length, width, and thickness of the bolometer element. The change in the resistivity with the specific energy absorbed by the bolometer element, **dε**, in units of energy/gram, is given by:

$$d\rho = \frac{d\rho}{d\varepsilon} d\varepsilon \tag{A3}$$

dρ can be given in terms of the differential energy absorbed by the bolometer element, $\mathbf{dE_{abs}}$, divided by the total mass of the bolometer element, $\mathbf{m_b}$,

$$d\varepsilon = \frac{dE_{abs}}{m_b} = \frac{dE_{abs}}{\rho_m \, w \, t \, l} \tag{A4}$$

where ρ_m is the mass density of the bolometer element.

NOTE: This assumes that the energy deposition into the bolometer element is uniform. I will come back to this later at some future time.

Using equations A1, A2, A3, and A4 we can find the differential energy absorbed by the bolometer in terms of the voltage change measured across the element and the constants that define the element parameters:

$$dE_{abs} = \frac{\rho_m \, w \, t \, l}{\frac{d\rho}{d\varepsilon}} d\rho = \frac{\rho_m \, w \, t}{\frac{d\rho}{d\varepsilon}} w \, t \, dR = \frac{\rho_m \, (w \, t)^2}{\frac{d\rho}{d\varepsilon}} \frac{dV}{I} \tag{A5}$$

Now to find the total energy absorbed by the bolometer element one can integrate both sides of the equation to find the total voltage change in the bolometer element:

$$\Delta E_{abs} = \frac{\rho_m \, (w \, t)^2}{\frac{d\rho}{d\varepsilon}} \frac{\Delta V}{I} \tag{A6}$$

NOTE: This assumes both that dρ/dε is a constant with respect to the energy absorbed and that there is not an energy loss mechanism occurring over the time interval of interest. I will come back to this at some later time.

The energy incident on the bolometer element is just equal to:

$$\Delta E_{inc} = \frac{\Delta E_{abs}}{f_{abs}} \tag{A7}$$

where $\mathbf{f_{abs}}$ is just the fraction of the incident energy absorbed in the bolometer element. If the energy is not absorbed it is either reflected from the surface or transmitted through the element. Given the total incident energy onto the bolometer element one can now find the energy emitted from the x-ray source.

The energy at the source that is intercepted by the bolometer element, $\Delta\mathbf{E_{src\_d}}$, is simply given by the source energy times the solid angle the detector has as seen from the source since the source & detector areas are small with respect to the distances between them. Therefore the source energy into the solid angle of the detector, $\Omega_\mathbf{d}$, is given by:

$$\Delta E_{src\_d} = \frac{\Delta E_{inc}}{\Omega_d} \tag{A8}$$

At this point one would like to find the total energy emitted by the source into all angles and this requires knowledge of the angular dependence of the source emission. For a uniform emitter the energy into all angles from the source is the same and hence the energy into a complete sphere is 4π times ΔE_{src_d} while that into a hemisphere is simply 2π times ΔE_{src_d}.

For a blackbody emitter the angular dependence of the emission has a $\cos\theta$ dependence where θ is the angle between the surface normal of the source and the viewing angle. In addition a blackbody source is by definition a surface emitter and so an integration over all angles includes just a hemisphere. The energy emitted normal to the source, $\Delta\mathbf{E_{src\_n}}$, is simply:

$$\Delta E_{src\_n} = \frac{\Delta E_{src\_d}}{\cos(\theta_d)} \tag{A9}$$

Given the symmetry of the problem the total energy from the source can now be found by integrating over the solid angle in spherical coordinates, $\sin\theta\, d\theta\, d\phi$, over a hemisphere as follows:

$$E_{src\_tot} = \int_0^{2\pi} \int_0^{\pi} \Delta E_{src\_n} \cos\theta \sin\theta \, d\theta \, d\phi \tag{A10}$$

$$E_{src\_tot} = 2\pi \Delta E_{src\_n} \int_0^{\pi} \cos\theta \sin\theta \, d\theta \tag{A11}$$

$$E_{src\_tot} = 2\pi \Delta E_{src\_n} \frac{1}{2} \tag{A12}$$

$$E_{src\_tot} = \pi \Delta E_{src\_n} = \pi \frac{\Delta E_{src\,d}}{\cos(\theta_d)} \tag{A13}$$

Using equations A13, A8, A7, and A6 the total energy put out by the source into 2π, $\mathbf{E_{src\_tot}}$, can be given as:

$$E_{src\_tot} = \frac{\pi}{\cos(\theta_d)} \frac{1}{\Omega_d} \frac{1}{f_{abs}} \frac{\rho_m (w\,t)^2}{\frac{d\rho}{d\varepsilon}} \frac{\Delta V}{I} \tag{A14}$$

The solid angle of the detector as seen by the source, Ω_d, is given by the detector area, w * l, divided by the source to detector distance, $\mathbf{d_{s-d}}$, squared and so equation A14 can be written as:

$$E_{src\_tot} = \frac{\pi}{\cos(\theta_d)} \frac{d_{s-d}^2}{w\,l} \frac{1}{f_{abs}} \frac{\rho_m (w\,t)^2}{\frac{d\rho}{d\varepsilon}} \frac{\Delta V}{I} \tag{A15}$$

To define a brightness temperature based on the total energy emitted one can differentiate equation A15 by time, τ, to get the total source intensity or flux, $\mathbf{I_{src\_tot}}$. The total flux emitted by a blackbody, $\mathbf{I_{bb}}$, at a given temperature, $\mathbf{T_{bb}}$, into 2π is given by:

$$I_{bb} = \sigma_{s-b} T_{bb}^4 \tag{A16}$$

Where for T in eV, and I_{bb} in Joules/(sec-cm^2), the Stefan-Boltzman constant, σ_{s-b}, is equal to 1.0284E+05 Joules/(sec-cm^2-°k^4). Therefore the equivalent blackbody

temperature which is emitting the same flux as our source, $\mathbf{T_{src}}$,(also known as the source's brightness temperature), is given by:

$$T_{src} = \left(\frac{1}{\sigma_{s-b}\, s_a} \frac{d E_{src\_tot}}{d \tau} \right)^{\frac{1}{4}} \tag{A17}$$

where $\mathbf{S_a}$ is the area of the source. If the signal to noise obtained from the detector is poor then differentiating the signal as indicated in equation A17 is not feasible. This is the case for the data obtained on the PBFA II target series to date, TAR94-1. Instead a temperature estimate is made by dividing E_{src_tot} by a time interval given by the full width at half maximum of the radiated flux, $\tau_{\mathbf{fwhm}}$, as determined by x-ray and/or pin diode detectors. In order to understand how this average flux compares to the peak flux emitted by the source we need to assume a distribution for the radiation output. If I take a Gaussian distribution for the radiation output, which is given by:

$$f(x;\mu,\sigma) = \frac{1}{\sqrt{2\,\pi}\,\sigma_\tau} \exp\left[-\left(\frac{(x-\mu)^2}{2\,\sigma_\tau^2} \right) \right] \tag{A18}$$

where I used a normalized Gaussian distribution for simplicity, then τ_{fwhm} is equal to $(8\ \ln 2)0.5 * \sigma_\tau$, where σ_τ is the standard deviation for the radiation output time interval. By definition the integral of the normalized Gaussian distribution is 1 and so the "average" intensity, $\mathbf{I_{ave}}$, compared to the peak intensity, $\mathbf{I_p}$, I come up with (again assuming a Gaussian distribution), is given by:

$$\frac{I_{ave}}{I_p} = \frac{1}{\sqrt{8 \ln (2)}\,\sigma_\tau} \sqrt{2\,\pi}\,\sigma_\tau = \frac{\sqrt{\pi}}{2\sqrt{\ln (2)}} = 1.0645 \tag{A19}$$

This shows that I_{ave} is actually **6.4% higher** in intensity than the peak intensity for a Gaussian intensity distribution. The peak source brightness temperature, $\mathbf{T_{src\_p}}$, which I will quote is then given by:

$$T_{src\_p} = \left(\frac{0.939}{\sigma_{s-b}\, s_a} \frac{E_{src\_tot}}{\tau_{fwhm}} \right)^{\frac{1}{4}} \tag{A20}$$

The total energy emitted into 2π, given by equation A15, and the peak source brightness temperature given by equation A20 is used in the PBFA II 94-1 bolometer

fielding sheets (where the f_{abs} is taken as 1). For the 93-1 target series these equations are used but the correction factor, 0.939, is not used in coming up with the temperature which would have the effect of raising the temperature by ~ 1-2% for that data.

In order to come up with an error estimate for this data I will, noting equation 4-9 in Bevington, take the partial derivatives with respect to the variables for equations A15 and A16, multiplied by their respective error estimate and then add the values in quadrature. Thus the error estimate for the total energy emitted into 2π , $\Delta \mathbf{E_{src\_tot}}$, is given by:

$$\Delta E_{src\_tot} = \pm \left[\left(\frac{\sin(\theta_d)}{\cos(\theta_d)} \Delta\theta_d \right)^2 + \left(\frac{2\,\Delta d_{s-d}}{d_{s-d}} \right)^2 + \left(\frac{\Delta l}{l} \right)^2 + \left(\frac{\Delta f_{abs}}{f_{abs}} \right)^2 + \left(\frac{\Delta \rho_m}{\rho_m} \right)^2 + \left(\frac{\Delta w}{w} \right)^2 + \left(\frac{2\,\Delta t}{t} \right)^2 + \left(\frac{\Delta \frac{d\rho}{d\varepsilon}}{\frac{d\rho}{d\varepsilon}} \right)^2 + \left(\frac{\Delta(\Delta v)}{\Delta v} \right)^2 + \left(\frac{\Delta T}{T} \right)^2 \right]^{\frac{1}{2}} E_{src\_tot} \qquad (A21)$$

where the component errors are given as standard deviations and the derived error is a one sigma error estimate. The error estimate for the peak source brightness temperature, $\Delta \mathbf{T_{src\_p}}$, is given by:

$$\Delta T_{src\_p} = \pm \left[\left(\frac{\Delta E_{src\_tot}}{E_{src\_tot}} \right)^2 + \left(\frac{\Delta s_a}{s_a} \right)^2 + \left(\frac{\Delta \tau_{fwhm}}{\tau_{fwhm}} \right)^2 \right]^{\frac{1}{2}} \frac{T_{src\_p}}{4} \qquad (A22)$$

where the component errors are again taken as standard deviations.

Reference

[1] Bevington, "Data Reduction and Error Analysis for the Physical Sciences," copyright 1969 and published by McGraw Hill. Just prior to his eq. 5-6 for the weighted average of a set of data points found on page 70 and equation 5-10.

7.13 Comparison of X-ray Filter Characterization Methods - T. E. Alberts

Introduction

The spectral study of soft x rays emitted from plasmas is a primary tool in understanding the physics of reactions occurring in fusion experiments.[1] X-ray filters facilitate this process by selectively limiting the x rays incident upon some diagnostic instruments from the full range emitted by the source plasma during an experiment.[2] Knowing the response characteristics of filters in actual use is critical for interpreting experimental data accurately.

Ideally, x-ray filters are characterized by x-ray transmission. However, it is much easier to characterize x-ray filters by alpha particle energy attenuation. We characterized a selection of x-ray filters by both x-ray transmission and alpha particle energy attenuation in order to compare the results and to identify sources of uncertainty.

The results of characterization should ideally be the same for either x-ray attenuation or alpha particle spectroscopy. Since the filters are used for their x-ray attenuation properties, the x-ray characterization results are viewed as the most useful for that application. The alpha spectrometer measurements would only be used to predict the x-ray response of filters. We eventually expect to establish a realistic correspondence between both methods of characterization. In establishing a correspondence, we hope to understand the factors affecting the uncertainties in using alpha spectrometer measurements to predict the x-ray response of a filter.

Measurement of Filter Thickness

We have chosen to use thickness as the property for comparison between measurements. This is because all filter specifications are made in the dimension of thickness and the first order of filter characterization by profilometry gives only film thickness. It is understood that for real calculations, the combined value of density, ρ, times thickness, t, must be used.

The transmission of alpha particles through a medium results in a measurable attenuation of particle energy. An alpha particle traveling through a medium will lose energy predominately through interaction with the electrons in the medium. The magnitude of this attenuation is dependent on the areal density (ρx) and atomic composition of the medium.[3] Spectral measurements of the energy of alpha particles transmitted through a foil in comparison to measurements taken without the foil reveal a peak shift to a lower energy. Based on known stopping powers of alpha particles in known mediums, this peak shift can then be used to infer the area density of the foil. The areal density can in turn be used to calculate the thickness of a foil of known density.

Various methods employing the energy attenuation of alpha-particles have been developed for the gauging of gas densities and foil thicknesses.[4] The method employed by Anderson[5] for thickness characterization of foils of known composition using alpha spectroscopy is used in this experiment. A software package was developed that calculates foil thicknesses from measured energy shifts. The calculations are based on known stopping distances of alpha particles in materials.[6]

Monochrome x-ray transmission through a medium or filter results in an exponential attenuation of intensity. At low energies, this attenuation is principally due to the energy of x-ray photons being absorbed by atomic electrons (photoelectric effect). More complete explanation of the theory behind this phenomenon, found in supplemental information,[3] discusses its relation to atomic theory and the observance of absorption edges. These absorption edges are the basis of using foils as x-ray filters to limit particular regions of an x-ray spectrum. Our interest here is limited to x-ray transmission measurements made at discrete energies.

The x-ray transmission of the filters in this study have been characterized at facilities located at LLNL and SNL. LLNL uses the Aracor Low Energy X-ray Machine (ALEX) for characterizing the filters. This facility uses a Henke tube for generation of x-rays and a gas-proportional-counter (GPC) for detection of x-rays. The SNL facility is still in development and measurements have yet to be published. This facility uses a single anode Manson source for generation of x-rays and a Kevex SiLi detector for their detection. The SNL facility has a slow measurement throughput of two filters at five energies per day compared to 18 filters at six energies per day at the LLNL facility.

The thickness of a single element filter of known density and mass attenuation can be calculated from a single x-ray transmission measurement at one energy. Measurements at multiple energies would ideally all result in the same thickness and the mean of the results should provide a reasonable approximation of the filter thickness. The experimental data have failed to meet this expectation satisfactorily. The mean thickness of filters measured at multiple energies rarely has a standard deviation below 10% and often exceeds 30%. This high uncertainty increases dramatically for multi-element filters. The greatest effort expended in this study has been concerned with interpreting this high deviation and determining the thickness value of a filter from multiple x-ray transmission measurements.

The large deviations could have several causes. For example, the x-rays generated for transmission measurements may not be a single x-ray energy. In the case of LLNL, the GPC does not distinguish between different x-ray energies, forcing us to assume the measurements are due to a single dominate x-ray energy. In the case of SNL, the peak data extraction does not yet account for background noise nor for detector resolution. Errors in the measurement of the x-ray transmission have not been fully studied. The filters themselves could lack sufficient uniformity or purity. These characteristics could be related to the material composition or quality of fabrication of each filter. For example, small pinholes in a filter would result in an increase in the measured

transmission of x-rays. This can be very significant if the filter is designed for low transmission. The equations used to calculate the thickness of a filter, are very dependent on the mass attenuation coefficient, μ. The uncertainty of these values has not yet been included in our calculations.

To calculate the thickness of a filter from multiple x-ray measurements we presently minimize an error function based on a least squares fit routine. We begin by defining the error function from the values of the measured transmission, T_m, and the calculated transmission of a filter, T_c, of thickness, t. The value T_m is the ratio of the measured values of incident x-ray intensity, I_o, and transmitted x-ray intensity, I, as shown in equation (1). Each of these values is a function of the x-ray energy, E. The predicted x-ray transmission of a filter, T_c, of thickness, t, is calculated using equation (2), where μ is the mass attenuation coefficient of the filter material. The value of μ is a function of the energy of the incident x-ray and is dependent on the filter material itself as well.[7]

$$T_m(E) = I(E) / I_o(E) \quad \text{- definition of x-ray transmission} \qquad (1)$$

$$T_c(E) = \exp[-\mu(E)\rho t] \quad \text{- relation of transmission to } \mu \text{ and } \rho t \qquad (2)$$

$$\text{error}^2 = \Sigma_E (T_m - T_c)^2 \quad \text{- function used to find filter thickness} \qquad (3)$$

The error function is used to find the thickness of a filter from multiple measurements (3-8 readings) at different x-ray transmission energies. This function is a sum over all measured values of energy, E. The value of T_c is calculated for the same energies as those used in measurement of T_m. In calculating T_c, the value of the filter thickness "t" is varied until the error function is minimized. A generalized reduced gradient algorithm defines the varying process for "t" and is only used to the find the minimum of the error function. The calculated thickness of the filter is the value that minimizes the error function. This method does not give weight to any particular measurement or to the magnitude of the transmission nor does it presently provide an uncertainty based on degrees of freedom. The definition of the error function and thickness uncertainties will become more refined as we examine uncertainties in individual measurements and calculations. This process has been automated in an Excel spreadsheet and can be used for multiple element filters as well as single element filters.

Presentation of Data

Figures 1 and 2 show a first order comparison of all available data. Figure 1 shows all data points while Figure 2 shows only the data for filters less than 1.5 μm thick. Barring the existence of a few stray points, the slope of the linear fit would suggest a rough one-to-one correspondence between the characterization methods. These stray points signify large errors and many are found to be characteristic of the filter material. As we pursue and refine this work, we hope to explain and eliminate these stray data points.

In a first order effort to eliminate stray data points, Figure 3 shows only data for selected thickness measurements. Filter designs showing consistently high errors, particularly those filters with carbon-hydrogen compounds and cobalt, have been omitted. The few high thickness filters have been omitted as well, since most of our measurements are of filters that are less than 1.5 μm thickness. The single element filters have also been identified since they require simpler thickness calculations and may be more accurate in revealing trends in the data. Close examination of the data points reveals that many points fall along a straight line. This suggests that a correspondence may apply to the characterization methods. This correspondence may be limited to certain regions of x-ray energy or be dependent on the composition of the filter material.

The numerical results of the generalized linear fit of the data shown in these graphs are listed in Table 1. We expect that any equation describing the correspondence between the characterization methods would intersect the origin

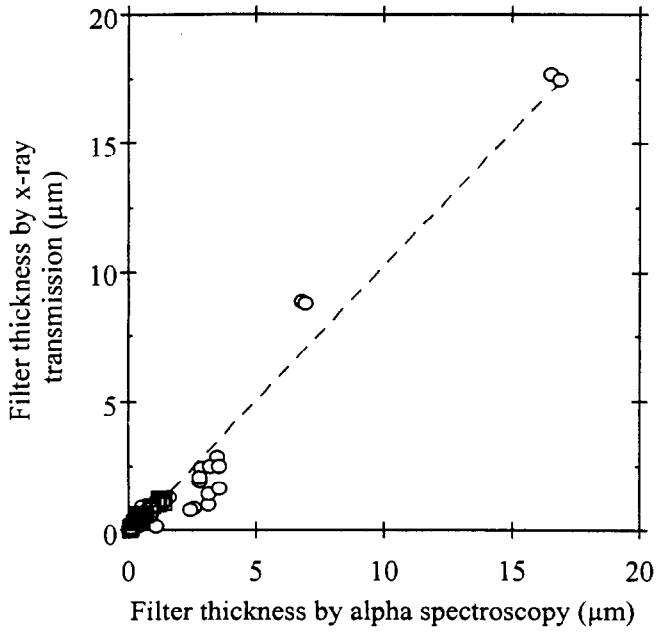

Figure 1. Comparison of filter thickness from alpha spectrometer and x-ray transmission measurements for all data. The straight line is a generalized linear fit for all points. Squares are single element filters; circles are multiple element filters.

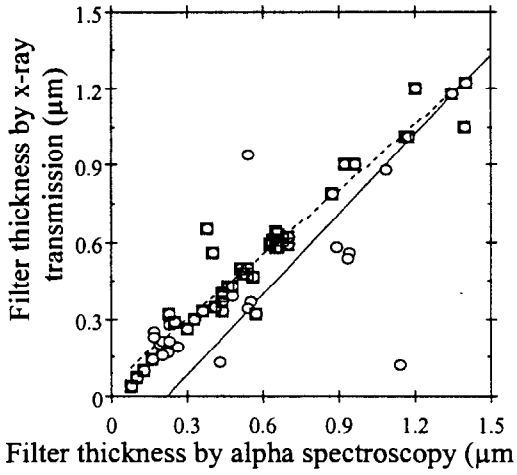

Figure 2. Comparison of filter thickness from alpha spectrometer and x-ray transmission measurements. This graphs shows only those filters up to 1.5 μm thickness. The solid line is a linear fit of all data points shown in Figure 1 (circles). The dashed line is a fit to the "selected," or consistent filters (squares).

and all three sets of data closely follow this characteristic. The slope of the linear fit would be 1 if the methods gave identical results.

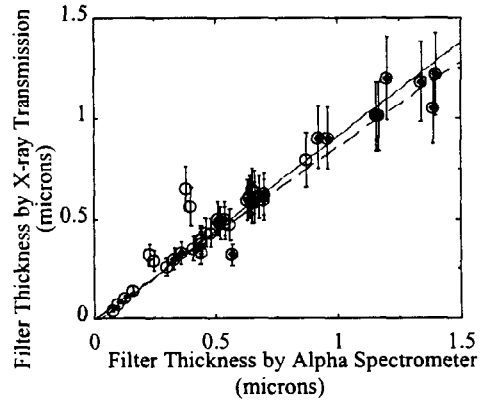

Figure 3. Comparison of selected filter thickness measurements from alpha spectrometer and x-ray transmission. Thick filters and filter designs with consistently high errors have been omitted.

Table 1. A least squares linear fit and error calculations were made on three sets of data. The linear fit shows how well each data set fits an ideal correspondence. The stated error is the uncertainty required in measurement to achieve a normalized Chi Squared value of 1.

Filter Data Set	y-intercept	slope	error
Ideal Correspondence	0	1	0%
All Filters (Figures 1, 2)	-0.229	1.043	57%
Selected Filters (Figure 3)	0.040	0.846	17%
Single Element Filters (Figure 3)	-0.003	0.858	14%

A linear fit was performed on three sets of data to show how well they compare to an ideal correspondence between x-ray transmission and alpha particle transmission measurements. The error value is the uncertainty required in the measurements for the data to fit a Chi squared test ($\chi^2 \leq 1$). The results from the set of all filter measurements shows a very poor correspondence between the characterization methods and a very high uncertainty in the data measurements. Filters with obvious x-ray characterization problems, such as surface quality as viewed with visible light, were included in this set for comparison purposes. These problem filters were removed from the second set. This set of "selected" filters shows a much better correspondence with appreciably better results in uncertainty. If we assume that the most reliable data set is indicated by the

lowest error, the best data set is for single element filters. This data set has the closest intercept with the origin and the lowest uncertainty but also indicates that filter thickness measured by alpha spectrometry is 86% of that measured by x-ray transmission. This is an important correspondence value and is very useful if verified by future research. While this value is an average for all the single element filters, future research should concentrate on determining correspondence values that may be dependent on particular elements.

Trends may also exist between the methods of characterization that may be dependent on the elemental properties of the filter material. We would like to see deviations between the x-ray characterization and the alpha spectrometer characterization that are consistent with some property of the filter material, but no obvious trends have been found. At this stage of research, our data does not suggest any dependence on atomic number, density, peak transmission, or peak energy. Considering that there appears to be no correlation dependence with respect to atomic number suggests that any correlation between the characterization methods may also be independent of the filter material involved.

Conclusions and Future Work

The uncertainty required in the transmission measurements for the data to fit a linear correspondence between the alpha-spectrometer and the x-ray transmission methods has been characterized. The best variation between the two methods of filter characterization is 14% for the set of single element filters. This is unacceptably greater than our goal of 10% and questions the validity of experimental results based on these characterization measurements.

More measurements need to be taken to verify the inconsistencies of x-ray transmissions on the same filter and to help explain the existence of the stray data points. A wider range of filter thicknesses and materials also need to be measured to support statistical conclusions dependent on filter properties. This should include a larger set of single element filters in order to simplify extraction of data from x-ray measurements and help identify either energy or elemental dependencies.

X-ray transmission measurements have the potential to characterize individual material thicknesses of filters consisting of multiple materials. Unfortunately, many filter thickness results between x-ray energies did not agree and totally unrealistic results frequently occurred when characterizing filters composed of multiple elements with similar transmissions. We do not yet have a complete explanation for all these inconsistencies because many need to be examined on a case by case basis. The extraction of filter thicknesses for the purpose of predicting the x-ray response of filters in other energy regions is not a trivial process and is still being investigated.

Alpha spectroscopy does not suffer from the large inconsistencies seen in the x-ray transmission results. This method, however, makes no attempt to characterize finished

filters composed of multiple materials. Also, measurements were made at only one energy, 5486 eV emitted from Am-248. It would be prudent to make measurements at other energies to see if results are as consistent as those taken at the Am-248 energy. A very positive attribute of alpha spectroscopy is that it does provide consistent results that may be taken as reproducible even if not accurate for x-ray filter applications.

The lack of consistent x-ray measurements and sufficient statistical data has not provided a comfortable understanding of the uncertainties involved with characterizing filters with these methods. Many weaknesses in our experimental methods have been identified but none appear significantly troublesome nor expensive to overcome. With the present procedures and equipment, many of the measurements were surprisingly close to predicted results. Enough information should provide better quantified uncertainties when foils characterized by alpha-spectrometer are used as x-ray filters. This would allow us to exploit the economic and throughput advantages offered by alpha-spectrometer characterization.

References

[1] L. P. Mix, E. J. T. Burns, D. L. Fehl, D. L. Hanson, D. J. Johnson, "Low Energy X-ray Emission from Light Ion Targets," AIP Conference Proceedings No. 75, Low Energy X-ray Diagnostics-1981.

[2] P.A. Ross, J. Opt. Soc. Amer. Vol 16, p 433(1921).

[3] G. F. Knoll, "Radiation Detection and Measurement," second edition, John Wiley & Sons, New York, 1989.

[4] W. H. T. Davison, "Measurement of Thickness Distribution of Thin Films by Alpha-particle Absorption," J. Scientific Instruments, 34, 418(1957).

[5] H. L. Anderson, "Alpha Particle Thickness Gauge Using a Solid State Detector," Nuclear Instruments and Methods, 12, 111-114(1961).

[6] Sandia National Labs, "FILTERLM.EXE," last modified by LeBow Inc., 1988. This program calculates filter thickness in microns from the energy attenuation of alpha particles passing through the filter.

[7] B. L. Henke, P. Lee, T. J. Tanaka, R. L. Shimabukuro, B. K. Fujikawa, "Low Energy X-ray Interaction Coefficients," Atomic Data and Nuclear Data Tables, volume 27 number 1, January 1982, Academic Press.

Intentionally Left Blank

8. Beam Characterization - A. R. Moats

During 1994, we executed a series of cylindrical hohlraum experiments on PBFA II. This was our second target series designed for lithium beams; the first series in 1993 used conical targets.[1] For these most recent experiments, we shot a total of nine 4-mm-scale, foam-filled cylindrical targets with approximately 2 TW/cm^2 lithium beam on target. One of our goals for this experimental series was to scale the hohlraum brightness temperature with the input ion beam and compare with theory. This quantitative scaling requires an absolute global measurement of the lithium beam power incident on cylindrical targets. Section 12 contains the results of this scaling.

In prior experiments with both proton and lithium sources, we had obtained relative beam intensities using characteristic line images of the gold cone walls of the targets themselves. For the cylindrical geometry in the 1994 series, we could not image the hohlraum side walls. Instead, a set of three to five titanium strips arranged around the target at a 5-mm radius (the Ti "Bird Cage") measured the height of the lithium beam vertical focus centroid, vertical width, azimuthal symmetry, and absolute intensity at three to five azimuthal locations. A picture of the cylinder target with the titanium strips is shown in Figures 2 and 4 of Section 3 on target characterization.

The titanium strips were inclined at a 65° angle with respect to the horizontal, forming a conical cage around the target with a radius of 5 mm from the central axis of the target at the midplane; this is 3 mm in front of the 2-mm radius target. Each strip was thick enough (0.5 mm x 0.5 mm square cross section) to eliminate contamination from Li ions from the opposite side of the anode. We placed one strip in each of three quadrants around the target (quadrants #1, #2, and #4) and two strips separated by 30° azimuthally in the remaining quadrant #3. For the first target shot, all five strips extended down to the bottom of the target (2 mm below target midplane) and up to the large brass insert above the target (5.6 mm above target midplane). For subsequent shots, we shortened two strips to 2 mm above the target midplane to prevent the "Bird Cage" from intersecting more than 10% of the incoming ion beam energy. These short strips gave us information on the beam behavior above the target only.

Two time-integrated x-ray pinhole cameras (TIXRPHCs) viewed the ion-beam-induced titanium K_α characteristic line radiation from the "Bird Cage." These cameras are discussed in Section 7. Figure 1 shows the titanium strips as seen from below the target looking upwards through the 3-mm-thick mylar windows that served as the argon-vacuum interface—similar to the view of the TIXRPHCs (the TIXRPHCS actually viewed the target at a 7° angle). Figure 2 shows a typical Titanium "Bird Cage" image of the five "Bird Cage" strips from the TIXRPHCs (from shot #6501).

An intensity scan along one dimension (or lineout) along each titanium strip represents the vertical beam profile at each of 3 to 5 azimuths during the peak power of the PBFA-II pulse. The film image can be analyzed to the 4.5-keV Ti K_α thick-target yield from Li^{+3} hitting the front side of each strip. Because the K-shell ionization cross-section for Li^{+3} on Ti decreases rapidly for ion voltages below the expected PBFA-II peak beam voltage, these yields will be weighted preferentially towards the higher lithium ion energies seen at the beginning of the voltage pulse and spanning the time of peak power in the incoming beam. These can be seen in the calculated K-shell ionization cross-sections in Figure 3 of Section 7.4 on titanium K- and L-shell emission. From a particle-in-cell code developed at Sandia National Laboratories that determines ion trajectories - SOPHIA [Section 7.4], the proton contamination for the target area at a radius of 5 mm is negligible; any proton in the beam will not focus within the radius of the Bird Cage. Thus, each strip should be a clear impression of the vertical beam profile close to the target at each of 3 (or 5) azimuths during peak power. A typical set of ion beam vertical profiles is shown in Figure 3. Note that in shot #6569, strips #1 and #4 are the shortened strips, thus showing near-zero intensity at the target midplane.

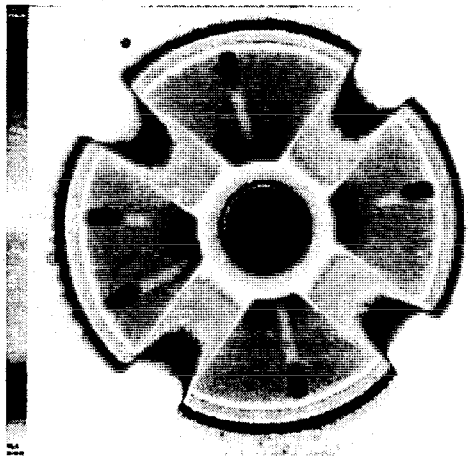

Figure 1. Radiograph of target viewing the 5 titanium strips from below (through the mylar windows).

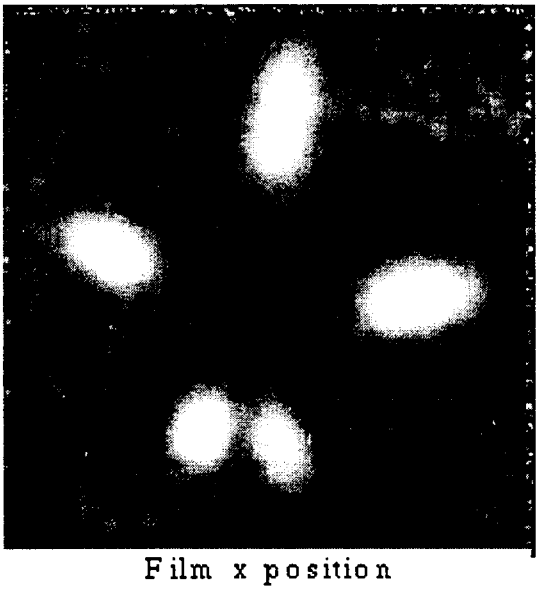

Figure 2. Example of Ti K_α image of Titanium Bird Cage from shot #6501. This camera viewed the target at an 7^o tilt angle.

The routines used to deduce the vertical beam profiles from these film images are discussed in Moats.[1,2] The corrections include subtraction of film fog and bremsstrahlung background, density-to-intensity conversion using data from Henke[3,4,5] geometric corrections due to the magnification and 8° tilt of the cameras, a 1/r correction for beam radial focussing, correction for the difference in apparent yield due to the relative angle between camera and strip angle (see Figure 4 of Section 7.4), and conversion from I(r)to I(z). (I is relative intensity, r is radial distance from the center axis, z is the vertical distance from the target midplane.)

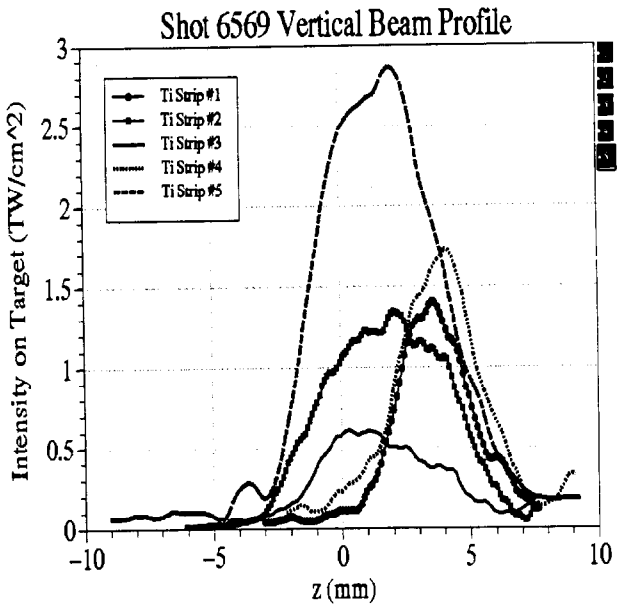

Figure 3. Vertical beam profiles from shot #6569. Strips #1 and #4 are shortened and thus only view the beam above the target. The target midplane is at z=0.

For three shots (#6501, #6560, and #6569), the resolution was high enough (nominally +/- 1 mm for z) to reliably gauge the centroid vertical focus position (Figure 4) and vertical full-width-at-half-maximum (FWHM in Figure 5) for each quadrant in which a long Ti strip was located. The focus for these three shots is consistently ~ 2 mm above the target midplane. For the 1993 Cone Target Series,[1] the focus varied high or low from shot-to-shot at the Ti strip located at 10-mm radius. This is as opposed to the 5 mm radius for the 1994 series. However, for the two shots from the 1993 series where the target cone was visible at a

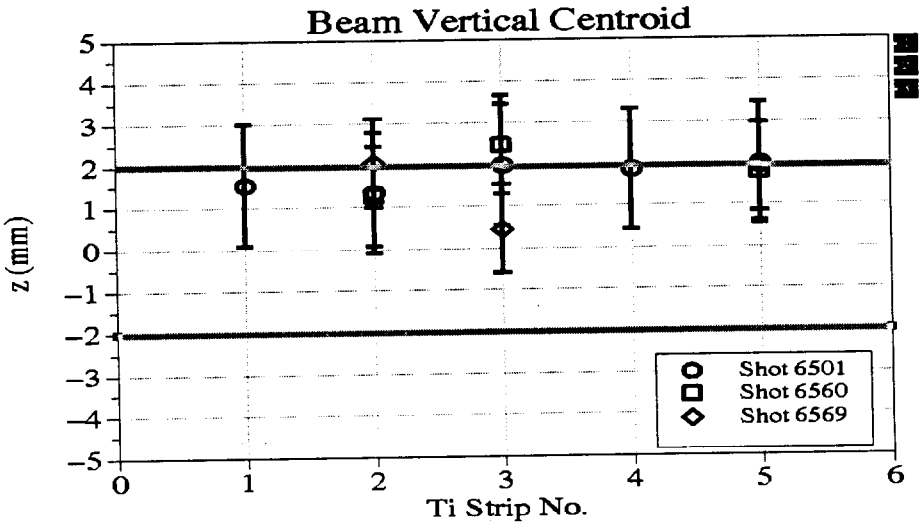

Figure 4. Vertical centroid focus position from three target shots. The target midplane is at z=0 and extends to +/- 2 mm.

nominal radius of 3 mm, we observed a focus above the target midplane at the target cone, even though the focus was centered at a 10-mm radius. We need more data before we can reliably identify this high focus at the target as a trend. The vertical width for the 1994 series appears quite narrow (down to 5 mm FWHM) at 5-mm radius, especially as compared to the average 8 - 10 mm FWHM reported for previous shots with an on-axis flat foil target using particle diagnostics. Note that the target itself is 4 mm high. Using the SOPHIA code, pre-focussing of the ion beam to a radius of 15 mm from the central axis was observed for the anode used for this target series. The data from the Ti "bird cage" is consistent with this conclusion.

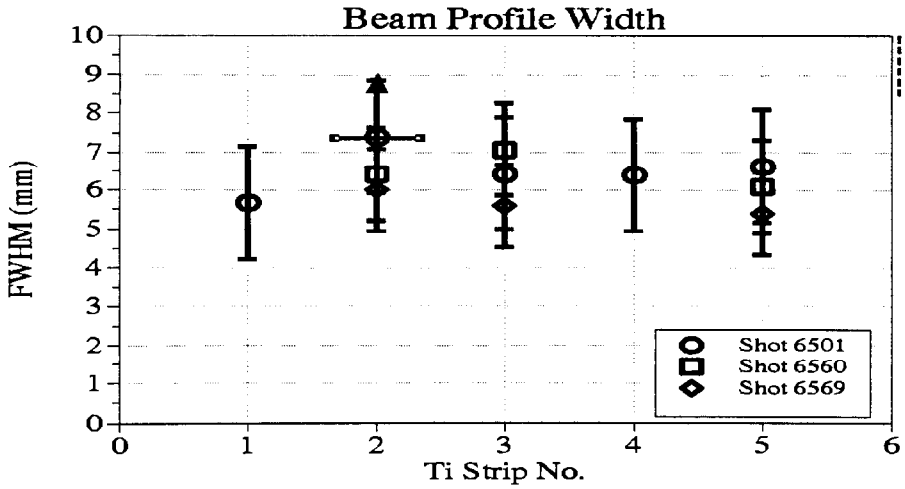

Figure 5. Full-width-at-half-maximum (FWHM) for the same three shots. Error bars are due to the spatial resolution of cameras.

As can be seen from the beam profiles of shot #6569 (Figure 3), the peak intensities and the intensity at the target midplane varied by more than a factor of 3 quadrant-to-quadrant. In fact, factors of 2 to 4 differences in intensity from strip to strip are commonly seen in all the 1994 shots. For one of the eight shots analyzed (shot # 6560), the maximum and minimum intensity seen for the titanium strips differed by more than a factor of 7, but maximum to minimum intensities of less than four were more usual. Figure 6 shows the range in intensities at the target midplane ($z = 0$) for each shot. Taking the average and computing a standard deviation σ for each shot yields σ of 24% to 86% of the mean. Qualitatively, looking at each shot, most of the beam energy appears to come from one or several "hot spots." The quadrants where these "hot spots" occur varies from quadrant to quadrant during the experiment and from shot to shot.

We demonstrated a much more azimuthally symmetric proton beam[2] during a PBFA II experiment using a proton source in 1991. For these shots, σ varied from 6% to 29%. This could indicate that the asymmetry is source-related.

Because of this asymmetry, any measurement where the intensity is averaged around the target from a limited set of separated points must be approached with caution. With only 3 full-length Ti strips intercepting the target midplane, we must assume some degree of smoothness about the beam's behavior between discrete measurements.

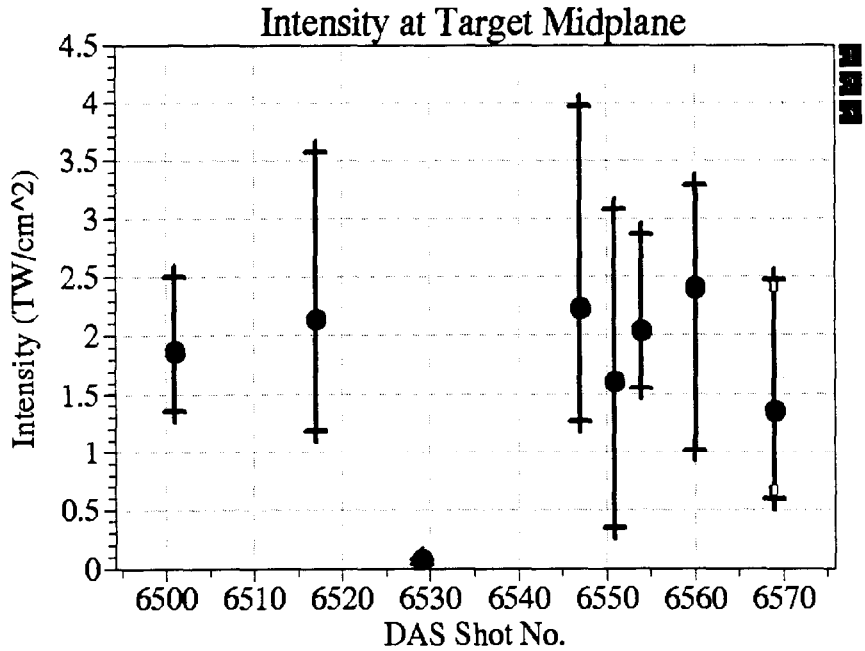

Figure 6. The range of absolute intensity for each shot is shown along the target midplane. Circles show the mean intensity; the crosses show the maximum and minimum intensities measured.

However, we can see wide variations in the beam profiles between the two strips only 30° apart in quadrant 3. One conclusion is clear: **Any experiment that draws generalizations from one-quadrant measurements for the LiF source are highly suspect and must consider the possible effect of this high degree of asymmetry.**

We compared the degree of azimuthal asymmetry with the asymmetry in the soft x-ray images of the foam and did not see any obvious correlations during this target series. In fact, while shot #6569 had the most asymmetric ion beam hitting the target, it had the most symmetric foam image. Beam smoothing is apparently occurring in the hohlraum even with this high degree of driver asymmetry. This is consistent with the results of the 1993 cone target series.

For the beam characterization discussed so far, relative shot-to-shot intensities were sufficient. However, we are now able to determine the absolute intensities necessary for scaling information. To accomplish this scaling, we used data from a set of two power-coupling series shots performed just prior to the 1994 Target Series to obtain a cross-calibration between particle and radiation-based diagnostics.

For shots #6472 and #6476, we added titanium strips, identical to the Ti "Bird Cage" (except for length and angle), 4 mm in front of a flat, 0.5-micron-thick gold foil

target at a 45° angle parallel to the gold foil. The target setup in this case is shown in Figure 7. The flat foil measured the Li beam intensity and energy from a 60° sector of the diode using the standard particle diagnostics (see the Section 3 on beam diagnostics by D. J. Johnson). A magnetic spectrometer (MS) placed above the target viewed the Rutherford-scattered lithium ions from the gold foil.[6, 7, 8] The Ti strips were placed so that their image did not shadow the field-of-view of p-i-n diodes used in the Magnetic Spectrometer to measure the ion beam momentum-time history. The TIXRPHCs that characterized the beam during the cylindrical-target series viewed the Ti strips from below for these two cross-calibration shots.

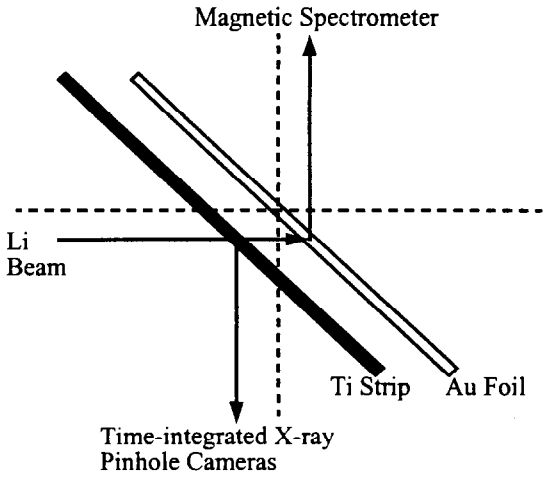

Figure 7. Target setup for cross-calibration shots, looking along the plane of the Au flat foil target (not to scale). Only the Ti strip at 45° is shown here, although another strip at 65° with respect to the horizontal was also fielded. The Ti strip shown is 4 mm in front of the Au foil.

The magnetic spectrometer measured the peak beam intensity at the flat-foil target [9, this report] while the yield from the Ti K_α image of the Ti strips was measured with the TIXRPHCs using the same analysis routines used for the target series shots.

Then, from both shots #6472 and #6476, the ratio between the peak intensity on the Ti strips at the centroid versus the absolute peak intensity on target (in TW/cm^2) as determined from the magnetic spectrometer was calculated. Peak intensity, rather than the intensity at the target midplane, was used both because of uncertainties in the position of the midplane for the titanium strips in the modified target holder for these shots, and because the peak intensity was the quantity most often available from magnetic spectrometer data analysis. These two shots yielded numerical ratios within 5% of each other. For subsequent target shots (assuming the same nominal voltage-current history as in the setup shots), we used the average of these two values to convert relative intensities to absolute intensities for both the 1994 cylindrical target series and the 1993 cone target series. Since the PBFA II diode configuration was held constant through these cross-calibration shots and the following 1994 Target Series shots and the voltage-current history was similar, the assumption that these ratios were constant is reasonable. However, this assumption is less valid for the earlier 1993 series.

Table 1 shows the absolute intensity of the average of the midplane target intensities by shot number. The second column shows the absolute intensity taken directly from the intensity-conversion factor of the cross-calibration shots in which intensity on the flat-foil for a 60° sector was used. From an analysis in the Section 4, there is a $6/\pi$ correction factor that translates the MS intensity (flat-foil for a 60° sector) to the actual beam-on-target for a 2π beam illumination on a cylindrical target. Thus, for the 1994 target series, the beam intensity on target centered around 2 TW/cm^2, as shown in column 3. We examined sources of error for the entire film-density-to-absolute-intensity process to determine the total error in the absolute intensity measurements (excluding error due to the azimuthal asymmetry). For each absolute intensity measurement at each azimuth, the error in the absolute intensity is 23.4%. The largest sources of error are the background fog on the film, uncertainties in the voltage history, the 1/R correction, and the filter transmission factors. There is also the uncertainty in the detailed beam trajectories that introduces an error in the conversion from the flat-foil to cylindrical geometry that we are unable to quantify at present.

So, for the 1994 cylindrical target series, we were able to measure for the first time the absolute ion beam intensity on a hohlraum targets. We also made measurements of the beam's apparent over focus and compared the observed focus with SOPHIA calculations. We measured the azimuthal intensity and found that the lithium beam was more asymmetrical than the previous proton beam shots. Notwithstanding, the 1994 target series shots were more reproducible than the previous 1993 LiF series in that the majority of shots centered around 2 TW/cm^2, consistent with previous shots. The shot-to-shot reproducibility of the average peak intensity of the ion beam during the 1994 series improved because of changes in the diode operation indicated from the 1993 series data.[10] In Section 12, we show the scaling of these mean intensities with the hohlraum's brightness temperature and compare these results with modeling.

Table 1. Intensity on target midplane from the TIXRPHC measurements with the Ti Bird Cage. Shots #5936 - #6022 are from the 1993 cone target series; shots #6501 - #6569 are from the 1994 cylindrical-target series. Intensity (flat-foil) is the uncorrected intensity that can be compared directly to flat-foil target shots; Intensity (on TAR93/94 target) is the corrected intensity-on-target from all quadrants during the hohlraum experiments.

Target	DAS Shot No.	Intensity (flat-foil) (TW/cm^2)	Intensity (on cone or cylinder surface) (TW/cm^2)
1993 Cone	5936	0.32	0.61
1993 Cone	5942	0.99	1.89
1993 Cone	5975	0.41	0.78
1993 Cone	5979	0.26	0.50
1993 Cone	6000	0.55	1.05
1993 Cone	6022	0.10	0.19
1994 Cylinder	6501	0.98	1.87
1994 Cylinder	6517	1.12	2.14
1994 Cylinder	6529	0.04	0.08
1994 Cylinder	6547	1.17	2.23
1994 Cylinder	6551	0.84	1.60
1994 Cylinder	6554	1.07	2.04
1994 Cylinder	6560	1.26	2.41
1994 Cylinder	6569	0.71	1.36

References

[1] A. R. Moats, M. S. Derzon, G. A. Chandler, R. J. Dukart, and T. A. Haill, 1995, Rev. Sci. Instrum. 66(1), 743.

[2] A. R. Moats, M. S. Derzon, D. J. Johnson, W. E. Nelson, J. G. Pantuso, C. L. Ruiz, and D. F. Wenger, 1992, Rev. Sci. Instrum. 63(10), 5065.

[3] B. L. Henke, S. L. Kwok, J. Y. Uejio, H. T. Yamada, and G. C. Young, 1984a J. Opt. Soc. Am. B 1 (6), 818.

[4] B. L. Henke, F. G. Fujiwara, M. A. Tester, C. H. Dittmore, and M. A. Palmer, 1984b, J. Opt. Soc. Am. B 1 (6), 828.

[5] B. L. Henke, J. Y. Uejio, G. F. Stone, C. H. Dittmore, and F. G. Fujiwara, 1986, J. Opt. Soc, America B, 3 (11), 1540.

[6] Fehl (1992), private communication.

[7] Kensek, 1990, private communication.

[8] R. J. Leeper, et al., 1988 Rev. Sci. Instrum. 59, 1860.

[9] D. J. Johnson, et al., Proceedings of the 7th IEEE Pulsed Power Conference, Monterey, CA, 1994.

[10] M. S. Derzon, et al., Rev. Sci. Instr., 66(1), 740 (1995).

9. Spatial Characteristics of X-ray Emission Out of the Diagnostic Aperture - M. S. Derzon

In Section 7.6, on time-integrated cameras, we observed that the size of features measured with the time-integrated pinhole cameras is similar for each energy cut. These features can be observed in Figures 1a and 1b as small fairly concentric closed contours in the plots. The contrast in the pictures is different although similar features are observed in each case. This is due to the different energy sensitivities, source spectral output and the slightly different resolutions for each camera. The same effects are quantified more clearly in Figure 2, where lineouts are shown at two energy cuts for two different shots. Dimensions shown in the figures are at the target.

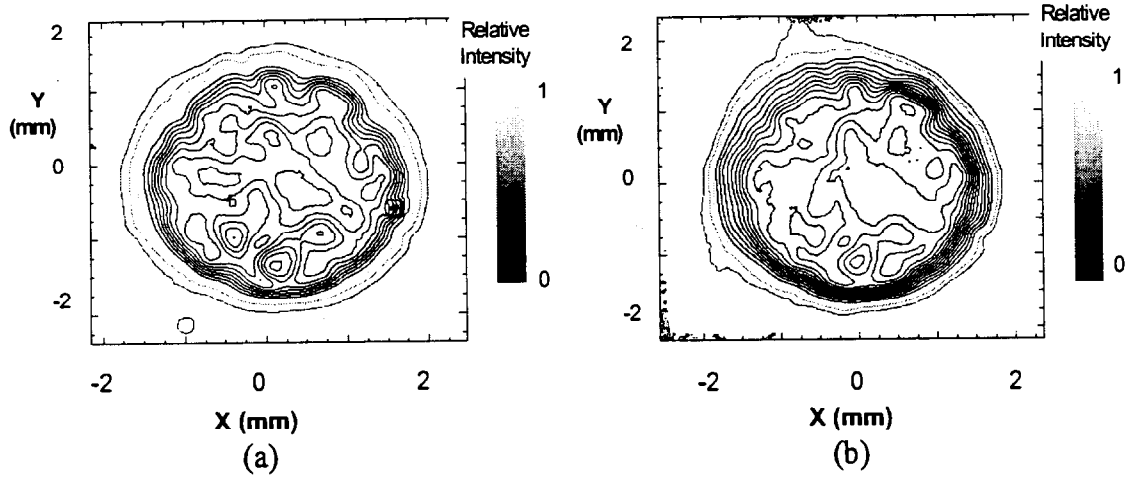

Figure 1. Images a (200-280 eV) & b (300-450 eV) from shot 6501. Smoothed with a five-pixel Lee filter. Dimensions shown are at the target. The diagnostic aperture is 3 mm.

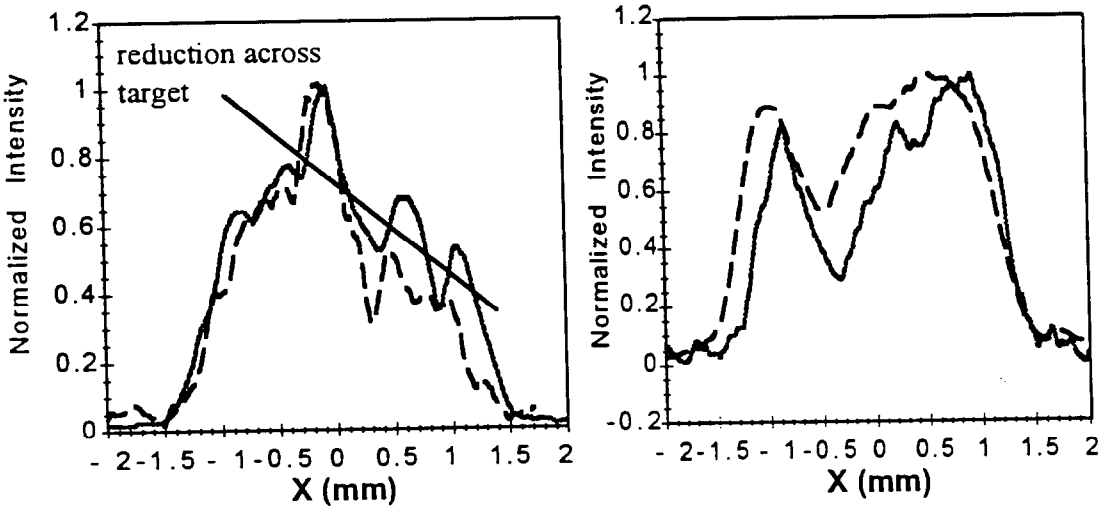

Figure 2. Lineouts through the central portions of shots 6529(a) and 6547(b). Dashed line is the 200-280 eV lineout, solid line is the 300-450 eV lineout. Dimensions shown are at the target. The diagnostic aperture is 3 mm.

One important feature is the mottling shown in Figure 1. By mottling (~0.5 mm structure) we refer to the spatial features of size, l, much greater than a pixel and much less than the target size, 0.038 mm$<< l <<$ 3 mm. These features appear as oblong features in the contour plots. Images from three of the six shots (6501, 6529, 6547) with large apertures exhibit similar features. On one of the other two shots the film was improperly installed and no images were acquired and on another (6569) the emission was uniform across the central emission feature.

In the three shots with mottling, 10-30% variations in intensity are observed. We cannot say with confidence whether or not there is an x-ray energy, or optical depth, dependence to these intensity fluctuations. In general, the mottling appears to be a reduction in intensity from a fairly uniform emission spot, rather than a uniform field with spikes. This is apparent in the contour plots where the small concentric features are reductions in intensity and the larger odd shaped features that comprise most of the area are the higher intensity background. The low intensity regions could be localized low temperatures or regions where cold material or impurities absorb some of the emitted radiation.

One of the shots, 6529 (see Figure 3), showed a trend in emission across the target (see Figure 2a), where the average intensity was much higher along one side of the target than the other (when the fluctuations are smoothed). This trend is observed in the horizontal lineout through the image center. It is not clear what the source of this trend is; we speculate that it may be large azimuthal non-uniformities in the beam, or density gradients in the foam. Another anomaly appeared in shot 6547, see lineout of Figure 2, where the emission footprint shows a single large decrease in emission as if the target were cracked, contained a void, or something obscured part of the target. It is unlikely something obscured the target, however, because we expect the feature would have sharper edges. Visible images of the targets acquired before the shots do not show any sign of these features.

The sixth of the large aperture shots, 6569, exhibits exceptional uniformity on the one frame which did not exhibit film saturation (see Figure 4). Unfortunately, the camera was misaligned and part of the image was off the useful portion of the film. Still, this image shows that uniform emission was obtained over most of the emission spot.

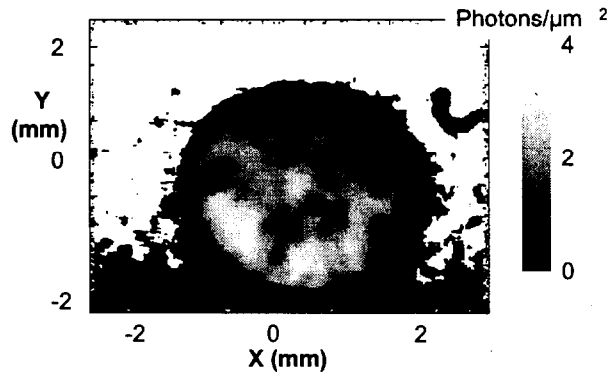

Figure 3. Shot 6529, soft x-ray energy image of emission out target aperture. Dimensions shown are at the target.

Images of the small aperture targets also gave unexpected results. For the three machine shots with small aperture targets the emission features were qualitatively different. For this reason we show a single image from each shot in Figure 5. Shot 6554 has intense regions and

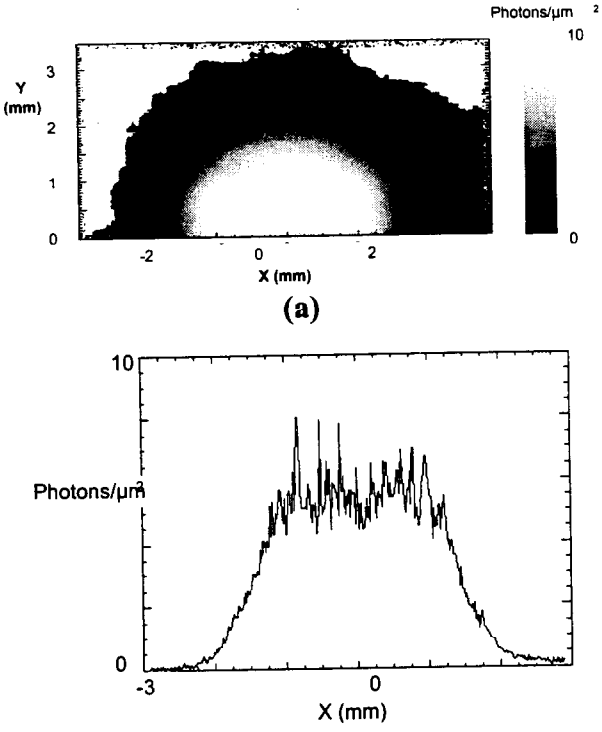

Figure 4. (a) 300-450 eV image from shot 6569. (b) Lineout through central chord of target. Dimensions are at the target.

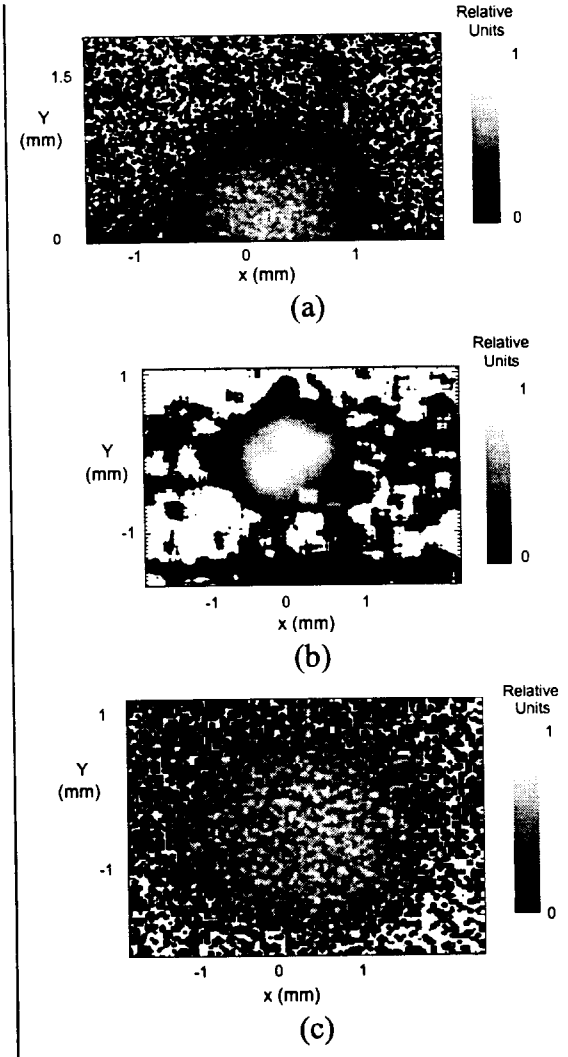

Figure 5. 300-450 eV images of three targets with 1.5 mm apertures. (a) Shot 6551, (b) Shot 6554, (c) Shot 6560. Dimensions shown are at the target.

shot 6560 has one bright region and the intensity changes across the region. The features observed in the images from the large aperture targets could be the source of the variations in the emission patterns observed here.

In analyzing other diagnostics it is necessary to have estimates of the source size and character. In Figure 6 we show lineouts through the center of each of these small aperture targets, and in Table 1 we show the FWHM estimated from the emission and the measured aperture diameter. For most of the large aperture targets, the measured FWHM are within ~10% of the preshot aperture diameter. In one case the size is larger than the original size, and in others it is smaller. This is not understood. For the small aperture targets the emission spot is ~30% smaller than the original aperture. The implications of this will be discussed in greater detail in the chapter on aperture closure, Section 10.

In summary, the emission spots are roughly the size of the preshot unperturbed dimensions. Many features are not understood. The emission frequently shows mottling, a short wavelength intensity fluctuation, and in one case a variation in intensity across the aperture in addition to the mottling. The small aperture targets exhibit some non-uniform features that are consistent with the effects observed in the larger aperture targets. The analysis of the time-integrated x-ray images place the most intense emission features close to what is expected. However, it is clear that there are many problems. The mottling that is obvious in the large aperture images may account for the features observed in the small aperture targets, but the source of the variations in emission for the majority of these shots is not obvious and more work will be necessary to understand this. The apparent decreases in intensity over the uniform field cannot be identified as being from the surface near the cameras or at the back of the target, and therefore the source of the non-uniformities cannot be identified through opacity arguments. The FWHM measured in some cases is greater than the initial hole size; the cause of this is not understood.

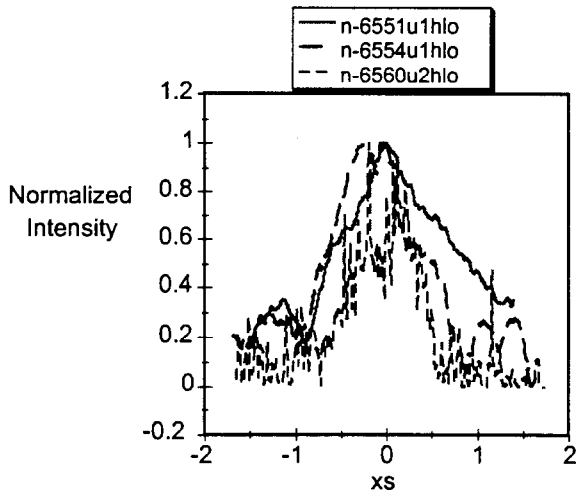

Figure 6. Lineouts through three the emission features of small aperture targets.

Table 1. Aperture size measured using x-ray images, and preshot characterization.

Shot Number	Preshot Aperture Diameter (mm)	FWHM (mm) *
6501	3.02	3.2
6517	3.02	----
6529	3.0	3.0
6542	3.0	----
6547	3.0	2.4
6551	1.61	0.9
6554	1.56	1.0
6560	1.67	0.9
6569	2.98	2.6

* - FWHM of x-ray emission, number shown is the mean obtained from the three cameras. The uncertainty in these is dominated by signal noise and background effects. I have not generated a good quantified estimate of 1-sigma (too much effort). Simple estimates place the relative error in size at 10%.

10. Measurements of Diagnostic Aperture Closure and Their Importance to Temperature Estimation - M. S. Derzon

Accurate and precise measurement of the time-dependent diagnostic aperture area is critical to the interpretation of the flux and fluence, and therefore the temperature, inside the hohlraum. By measuring the edge features of the time-integrated soft x-ray images we can estimate a time-averaged velocity for different energy x-rays and the effect on temperature estimation. We are also developing slit-imaging instruments for the time-resolved measurement of the aperture size and profile, as discussed in earlier sections of this report. In this chapter we present the results of both the time-integrated x-ray image interpretation with regard to aperture closure and the time-resolved aperture measurements. Time-dependent hole closure velocities were measured, giving a time-averaged velocity of ~2 cm/μs, in good agreement with sound speed and time-integrated estimates.

In this chapter we also present analysis of the effect of hole closure on temperature estimates from the bolometers and XRDs for both the large and small aperture targets.

Estimated velocity based on time-integrated images

We estimated the aperture closure by taking the difference in the initial diameter, the measured hole size, and the measured FWHM of the x-ray emission feature from the time-integrated cameras. The results compared to peak power on target are presented in Figure1 as a function of the peak intensity as obtained from the inner-shell x-ray emission measurements. The dimension used in the plot was the average obtained from the available images at all energies (see Table 1 in previous section). The negative value displayed corresponded to the one shot where the emission spot size was larger than the initial aperture. It is of interest to observe that there is no trend observed in this data.

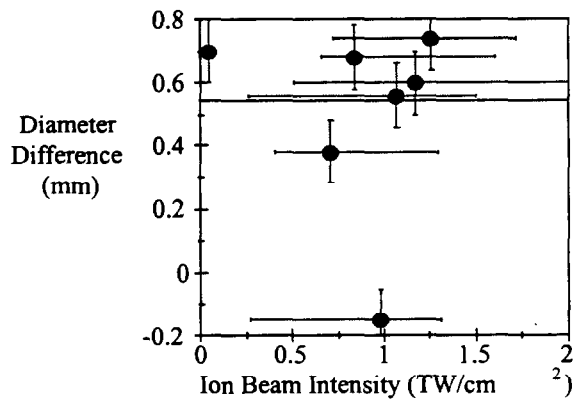

Figure 1. Comparison of the difference in aperture diameter between the preshot diameter and the aperture size as estimated from the time-integrated soft x-ray images. The horizontal line represents the mean diameter difference.

The effect of ion beam intensity on velocity was not modeled. However, we expected some sort of deterministic trend. There may be a trend if the two questionable points, the low intensity

and the negative diameter difference, are dropped. However, as of this writing there is no objective reason for dropping those two points from the analysis. Because there was no clear spectral dependence on measured size there was no correlation with x-ray energy.

Using the mean diameter variation of 540 μm from the time-integrated cameras (not including the negative point), we estimate the aperture velocity to be (540 μm/2)/15 ns or 2 cm/μs, where 15 ns was used as the width of the average power pulse on the target. This can be compared to the sound speed of the gold, as calculated in the equation below (see Plasma Formulary):

$$C_s = \left(\frac{\gamma Z T}{M_i}\right)^{1/2} = 9.79 x 10^5 \left(\frac{\gamma}{\mu}\right)^{1/2} \left(\bar{Z} T\right)^{1/2} \quad (1)$$

where γ = adiabatic index = 1.1, μ = ion mass in proton units = m_i/m_p = 197, Z = average charge state = 16, T = temperature in eV.[1] The sound speed of gold is 2 cm/μs at 60 eV (from the XRDs). This type of simple estimate suggests that the amount of motion observed is reasonable. The caveats to keep in mind when considering the interpretation: the gold does not move at this peak velocity throughout the power pulse and the velocity is sensitive to x-ray energy because the spectrum could vary depending on the amount of material between the source and the detector (however, no trend was observed). Also, this calculation does not account for the tamping of gold motion by the presence of foam in the aperture. The calculation is useful only to show that the amount of motion observed is reasonable, based on a simple model. The next section contains a more rigorous discussion based on other measurements that provide consistent conclusions.

Estimated aperture closure based on time-resolved measurement of hole size

The EST diagnostic, discussed in Section 7.7 takes one-dimensional images of the x-ray emission out the aperture. An example is given below in Figure 2. The uniform intensity region at the left of the image is signal generated by bremsstrahlung in the fibers, faceplate, and scintillator. The oblong intensity band at 80 ns represents the emission from the target aperture.

The results are typically quantified by analyzing sequences of both vertical, at a fixed time, and horizontal, at a constant position, lineouts. The vertical lineouts provide estimates of the emission feature size and shape as a function of time, and the temporal axis lineouts can be used to determine if the emission at the edge of the aperture has a different duration than that at the center. For example, by fitting a Gaussian to 2-ns wide vertical lineouts we have obtained the source size estimates shown in Figure 3.

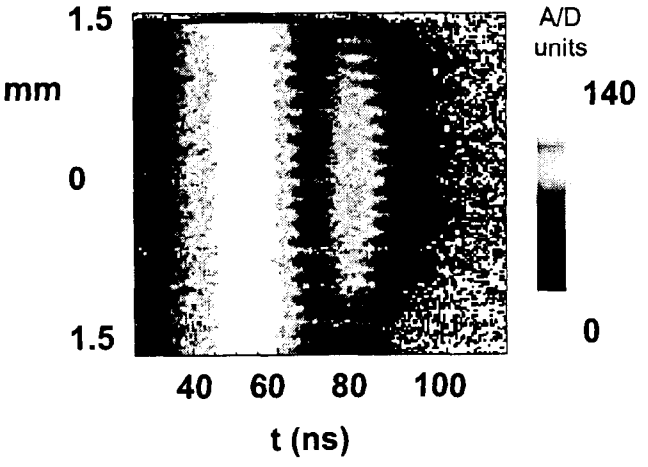

Figure 2. Flat field corrected streak image of the bremsstrahlung and x-ray emission from shot 6569. The term A/D units refers to relative intensity into the CCD camera which collects the charge in a preamplifier and then converters the analog(A) signal to a digital (D) and in this case arbitrary unit, A/D unit.

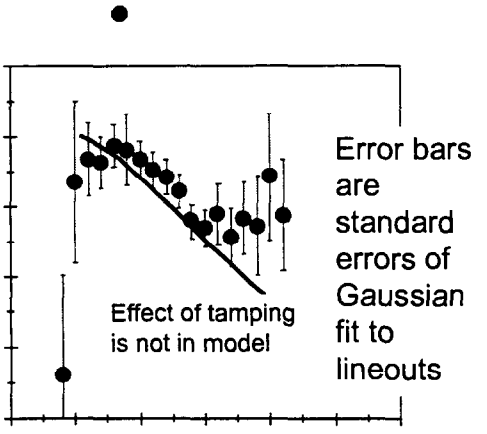

Figure 3. Unfolded source size estimate for shot 6569 compared to calculated size using sound speed estimates for hole closure velocity.

The aperture size versus time was estimated by subtracting twice the sound speed (since the diameter changes twice as fast as the velocity) times the time. The temperature history used in the calculation was obtained from shot 6517, the highest temperature shot, and time corrected to best match the rise of the emission from shot 6569. Shot 6517 was used because it was the only shot for which the XRD results had been analyzed, as of this writing. The velocity of the gold was assumed to be constant once the gold reached peak temperature. The comparison with the simple model is shown because the model appears to predict the amount of hole closure until the foam is able to tamp the motion of the gold.

We also compared the shape of the emission feature as measured with the EST diagnostic to a simple model. This is basically an transform in order to estimate a radial emission profile. The general solution of an azimuthally symmetric source into a 1-dimensional intensity profile is shown in the equation below,

$$\underset{profile}{Measured} = \frac{dS(y)}{dy} = \int_x I(r)\,dx \quad , \tag{2}$$

and the parameters are defined as shown in Figure 4. For a uniform source, where I = constant for $r < r_0$, the measured profile is given by,

$$\frac{dS(y)}{dy} = \int_0^{r_0} I(r)\, dx = I_0(2\sqrt{r_0^2 - y^2}) \tag{3}$$

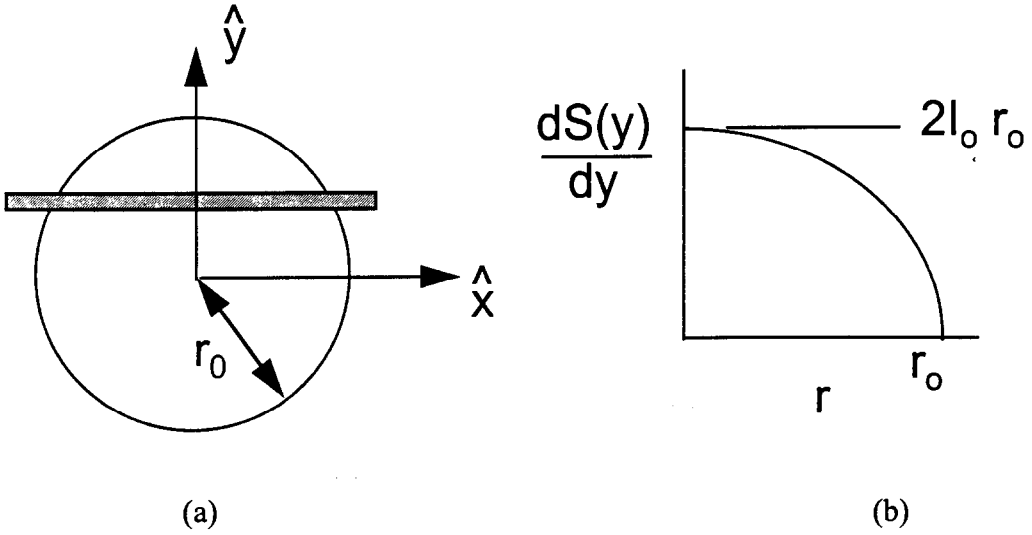

(a) (b)

Figure 4. Schematic illustrating how measured 1-D profiles allow estimates of emission feature parameters. (a) Geometry, (b) Simulated profile.

From this it is straightforward to relate the FWHM of the measured profile to the radius of the emitting source,

$$FWHM = \frac{\sqrt{3}}{2}\ 2\ r_0 \tag{4}$$

The source size plotted in Figure 3 is then the inferred size, assuming a uniformly emitting circle. For shots 6551 and 6569 this assumption is reasonable since the time-integrated images, as shown in Section 7.7 on the time-integrated cameras, were fairly symmetric.

We know that the source is fairly uniform in azimuth, with the exception of the mottling, based on the time-integrated images from Section 9. The central feature of the large-aperture emission also appears fairly constant with radius. Therefore, the 1-dimensional images can be unfolded to obtain a crude idea of the radial profile, as shown in Figure 5. The figure shows normalized intensities for a few different radial profiles, as a function of normalized radius, and illustrates that the measured profile can be compared to hypothesized profiles without resorting to options such as Abel inversion.

In this case, the results from shot 6569 show that the profile at peak emission is roughly constant with radius.

This comparison is adequate if only gross features of the profile are important. The measured profile is more similar to the constant profile than either a profile that increases at large r, i.e., f(r) = r, or one which decreases at large r, i.e., f(r) = 1-r. This implies that the emission profile is close to uniform with radius across the aperture.

A simple pressure balance argument can suggest the amount of motion that might be observed before the gold would be tamped. At steady state, no motion and constant temperature, the pressure in the foam will equal the pressure in the gold when,

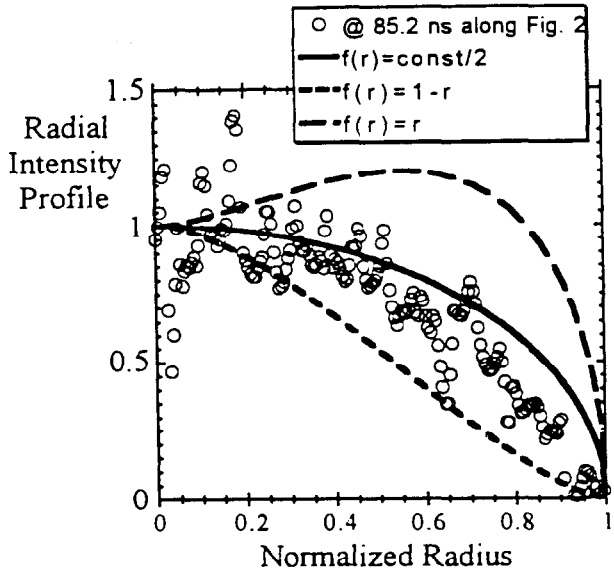

Figure 5. Intensity normalized at r = 0 and slit-imaged intensity profiles for data of shot 6569 and a few potential radial intensity dependences.

$$(\overline{Z_{CH_2}} + 1)\, n_{CH_2} T_{CH_2} = (\overline{Z_{Au}} + 1)\, n_{Au} T_{Au} \tag{5}$$

or

$$n_{Au-ablt} = \frac{(\overline{Z_{CH_2}} + 1)\, n_{CH_2}}{(\overline{Z_{Au}} + 1)} = \frac{(\overline{2.5+1} + 1)\, 2.6x10^{20}}{(16 + 1)} = 5x10^{19} \quad [cm^{-3}] \tag{6}$$

when the temperature in the gold is assumed to equal the temperature in the CH_2. The values of Z were obtained from the LASNEX results. If the amount of solid density material blown off of the thick aperture edge is known, then the thickness of solid density material can be related to the thickness of ablated material by,

$$t_{Au-ablt} = \frac{n_{Au-solid}}{n_{Au-ablt}}\, t_{initial} = \frac{6x10^{22}}{5x10^{19}}\, t_{initial} \tag{7}$$

The mean free paths in gold of most of the photons at this temperature are at or below 0.5 μm. Using 0.5 μm for the thickness of solid density gold that is ablated into the aperture implies that the gold would be expected to expand no more than 1 mm. Clearly a better calculation needs to be done; however, the gold motion observed (500 μm in diameter) and the velocity are reasonable given the simple modeling.

A more detailed simulation was performed with Lasnex to understand the hole closure that was observed. This modeling was discussed in Section 5. We show the results of this modeling in Figure 6, where we have superimposed the results from shot 6551, which was a small (1.5 mm) aperture target, the power pulse used in the simulation, and the Lasnex estimate of the source size. The data indicates that the diagnostic aperture stayed open till after peak deposition, which is nearly co-incident with peak temperature in the modeling. Because the simulation did not run past 20 ns due to zone tangling and the experimental uncertainty is large, it is only reasonable to state that the experiment does not disagree with the simulation. The uncertainties shown in the figure are the standard error in a least squares fit to a $(1-r^2)$ 0.5 profile. There is a 5% systematic error in the magnification, not shown, which may account for the slightly larger inferred source size.

When the experimentally obtained source sizes are compared for both the large and small aperture targets, by adding 1.5 mm to the source size for the small aperture, the general trends and slopes are similar (see Figure 7). We do not have the precision to determine if the modeling

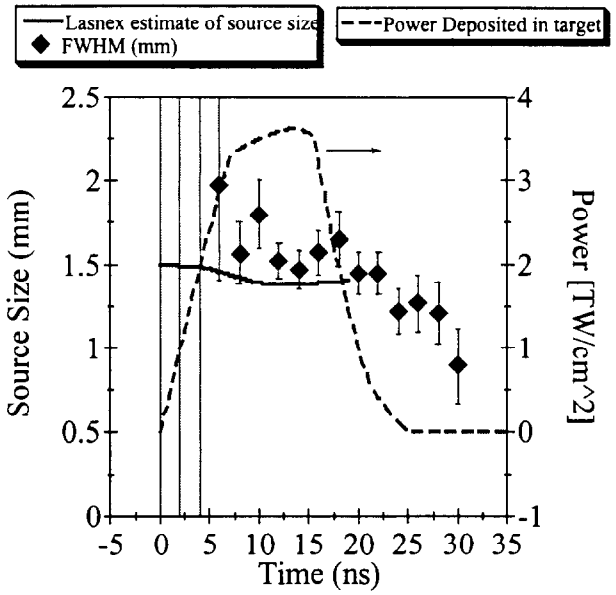

Figure 6. Comparison of a Lasnex simulation with inferred source size and ion beam power pulse for shot 6551. The dark solid trace is the Lasnex simulation, points are the experimentally determined source size, and the light trace is the ion power pulse.

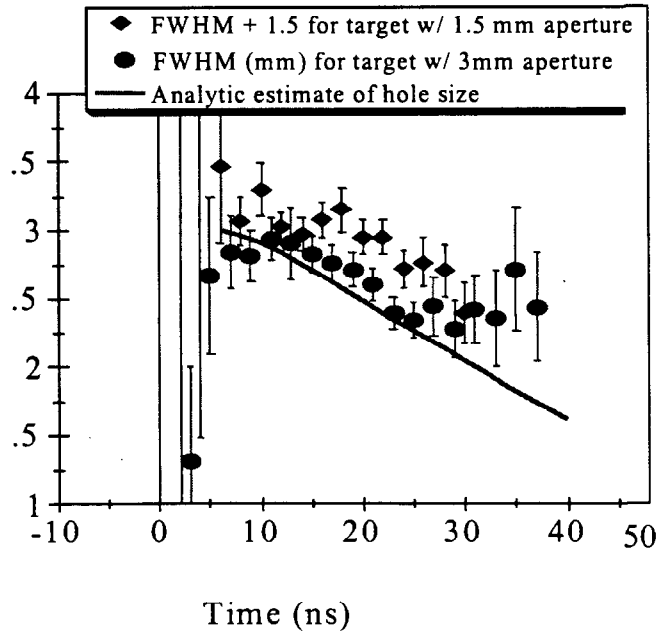

Figure 7. Comparison of source size for small- and large-aperture target shots to the sound speed model for hole closure.

and experiment are in good agreement. Because of the lower signal for the small aperture target, the useful portion of the trace ends earlier than on the large aperture shots. The effect of tamping is obvious in the large aperture target and not in the small aperture target. The slopes appear similar in both cases, as expected for similar temperature profiles.

Effect of hole closure on bolometer and XRD interpretations of temperature

In Figure 8, we compare the temperature as determined from the uncalibrated time-integrated calorimetery of the bolometers to the peak temperature as determined with the time-resolved XRDs. Both diagnostics are spatially integrating. It is clear from the figure that the bolometers routinely give temperature estimates that are higher than the XRDs by roughly 20%. The difference may be due to calibration errors or they may be caused by the methodology used in obtaining the temperature.

Temperature is determined from equations 9 and 10 for the bolometers. As shown in eqn. 9, the total fluence measured by the bolometers, F_T, is proportional to the 4th power of the temperature, linear with area of emission, assuming a uniform source, and the pulse width.

$$F_T = \int_0^\infty dt \int_{-\infty}^{\infty} dA(\sigma T^4) \cong \sigma T_p^4 A \, \Delta t \tag{8}$$

$T_p \cong \sqrt[4]{F_T / \sigma A_{FWHM-TI} \Delta t}$, where $A_{FWHM-TI}$ is the time-integrated (TI) full width at half-maximum. (9)

For the XRDs the temperature is estimated from

$$T_p \cong \sqrt[4]{P_T / \sigma A_{FWHM-pk}} \tag{10}$$

where σ is the Stephan-Boltzman constant. It is the weighting factors, $A_{FWHM-pk}$, $A_{FWHM-TI}$, Δt that are responsible for differences in the temperature estimates that are not caused by calibration errors between the XRDs and the bolometers.

In the general case, as a function of time, an appropriate area is obtained from the expression

$$A = \int_{emission\ spot} I(x,y)dA / I_0 \tag{11}$$

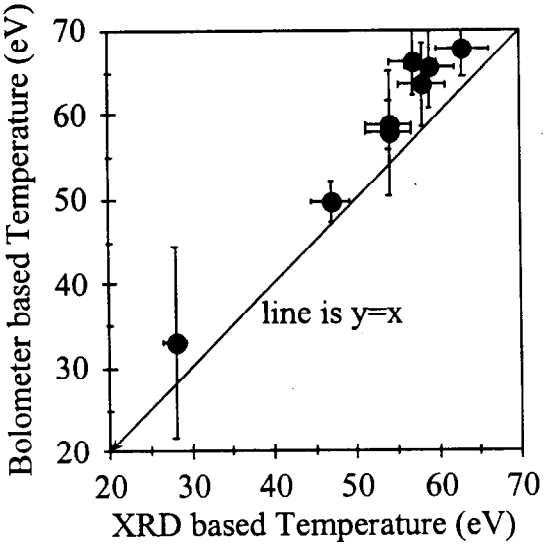

Figure 8. Estimated temperature as determined by the bolometers vs. the XRDs.

where I is the x-ray intensity as a function of position and I_0 is the peak intensity. We have not measured A as a function of time. In its place we use the time-integrated value of A obtained from the average area of the available soft x-ray images. Using the FWHM of the typical XRD trace (which is not Gaussian and assymmetric about the peak, as shown in Figure 9), to generate an uncertainty results in estimated temperature results with an artificially short width and therefore a high temperature. If we use the temporal width of the central fiber of the EST diagnostic images of the emission, we obtain a temporal width longer than from the XRDs, consistent with the effect expected due to hole closure, but which should be used with a smaller emitting area than the initial hole size. Therefore, in all of these instances only an approximate temperature is obtained.

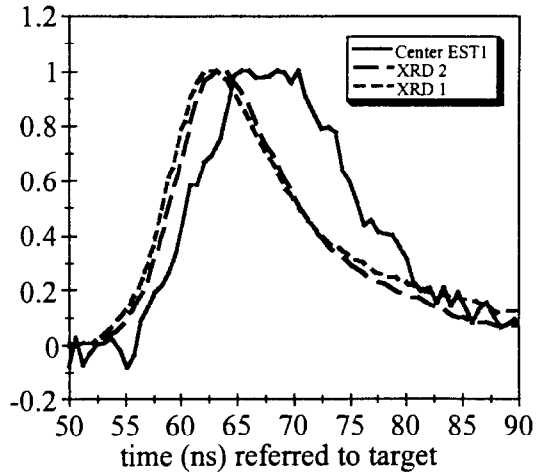

Figure 9. Time history of two XRD traces and the emission from the center of the target as obtained with the EST diagnostic. The $FWHM_{center} = 17 \pm 4$ ns and the $FWHM_{XRD} = 13 \pm 2$ ns.

To explore the effect of these weighting factors further we have generated Figure 9. In this figure we compare bolometer results using slightly different values in the area and temporal widths chosen as weighting factors and use the same XRD interpretation. To gain an understanding of the magnitude of these effects in order to get an idea of the systematic error, we have plotted estimates of temperature as determined from the bolometers versus the original XRD estimates using a variety of estimates for the area and temporal width of the emission. The bolometer results of Figure 7 were obtained using the nominal hole size, which assumes constant emission over the radius, and uses an average FWHM from the XRD traces.

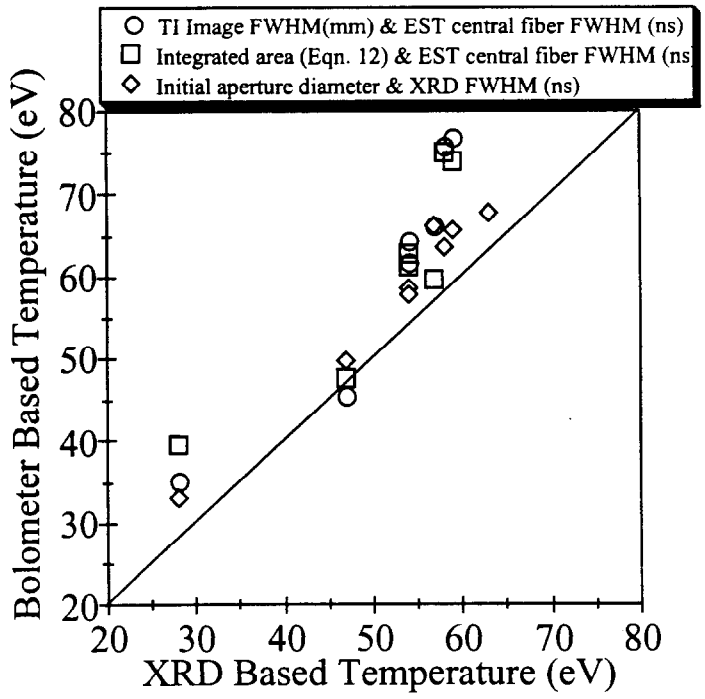

Figure 10. Comparison of bolometer-based temperature estimates using different estimates of the emission area and the temporal FWHM.

In Figure 10, the circles represent using the area of the open aperture, as measured with a visible camera, before the shots were fired to determine the appropriate area for the emission and the

temporal FWHM of the center of the emission feature obtained from the EST diagnostic. The square points correspond to using the area obtained from equation 12 with time-integrated images, and the FWHM from the XRDs. The difference is typically 3 eV for timing differences and as high as 10 eV for hole closure estimates.

To summarize, the bolometer temperature estimates can be affected by roughly 6% depending on whether or not the FWHM of the XRD traces or the EST central fiber FWHM is used to estimate the pulse width.

Effect of hole size on temperature estimates

The modeling predicts a slight increase in temperature, 3-5 eV, for the small aperture targets. In an attempt to determine if this effect was observed and if the hole closure had an effect, we analyzed the temperature data based on hole size. The result is shown in Figure 11. There is no correlation between the XRD-inferred temperatures and hole size. Chi-squared testing with a 5 eV uncertainty shows no linear correlation in the bolometer-inferred temperatures with aperture size, although a linear correlation coefficient of 0.8 implies there is some relationship with hole size. We are not confident that a correlation has been measured.

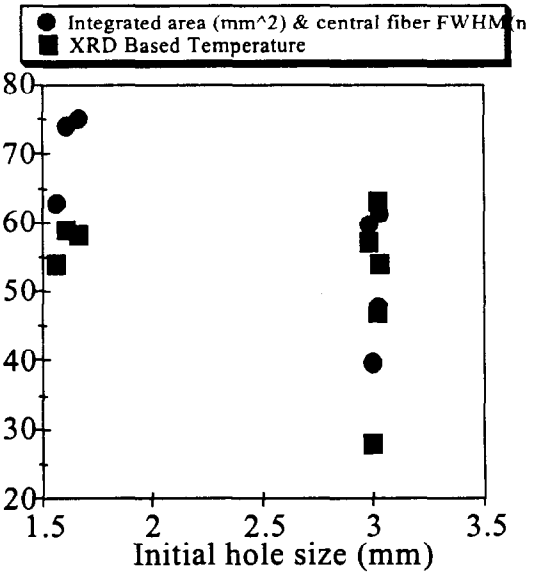

Figure 11. Temperature comparison of bolometers and XRDs with initial hole size. XRD and bolometer estimates made using FWHM of emission spot and XRD temporal FWHM.

Conclusions

We find that the time-integrated and time-resolved inferred estimates of hole velocities are consistent with 2 cm/μs. We have been able to measure the velocity and perform consistency checks with simple scaling arguments. We have not been able to further our understanding of the hole closure physics by comparison with Lasnex simulations. Both better modeling and smaller experimental uncertainties will be required for a better understanding of the complex dynamics of hole closure.

We were unable to experimentally observe the ~ 4 eV predicted effect of hole size on temperature. This would be damning except we did not expect to see this given our experimental uncertainties and the measured shot-to-shot variations in beam performance. The primary reason for using two aperture sizes was to ensure adequate emission for imaging and hole closure measurements, and the change in the targets aperture allowed the comparison and provided information for us to identify the "mottling" discussed in Section 9.

References

[1] R. Dukart, Private Communication 1994.

11. X-ray Spectral Measurements

11.1 X-ray Diode Results - G. A. Chandler

This section contains a description and results from an analysis of the 13 x-ray diode (XRD) detectors used to measure the soft x-ray radiation flux from the targets. After the results are given with a short discussion of the data, a detailed description of the experimental setup, the detectors, and the data analysis follows.

These detectors have been absolutely calibrated and yield the most accurate measurements we have of the spectral components from our targets in the energy range between ~100 – 1000 eV. The spectral resolution is quite low, having an $E/\Delta E$ of only about 2 or 3. Since the response as a function of energy is far from a simple step function, the spectral unfolding is fairly complex. The XRDs are well complemented by the bolometer detectors. These were described in Section 7.12, they have a flat or consistent response over most of the energy regime of interest. The bolometers are time integrated and rely on intrinsic as opposed to calibrated responses. In contrast to the previous PBFA-II target series, TAR93-1, where the inferred temperatures between the XRDs and bolometers were in good agreement, the bolometers indicated a higher temperature than the XRDs.

In the XRDs a soft x-ray flux passing through a filter and onto a photocathode induces a photoelectron current which is collected across a biased vacuum gap. The sensitivity, the electrical current measured as a function of the photon flux, is a complex function of the filter and photocathode response. These detectors respond fast enough, ~0.5 ns, to yield a time-resolved measure of the incident photon intensity. In the following section, the results from the XRDs will be presented.

Summary of results from the XRD Detectors

The results for the 94-1 target series, using the calibrated response of the XRDs for the peak flux and the inferred brightness temperature are given in Table 1. Except for the 1st, 3rd, and 4th shots, shown with strike-through characters in the table, the accelerator performed well. In the table, with the noted exceptions, the peak flux radiated out of the top of the targets in the energy band between 98.1 and 1200 eV into 2π is listed along with a one-sigma error estimate. For the first exceptional target shot (2025) the same filtration was used for all of the XRDs with an aluminum photocathode and a second set of filters was used on the XRDs with a carbon photocathode. This was done to check for diagnostic issues associated with the lines of sight to the target. Thus a spectral unfold of the data from this shot to yield a brightness temperature was not possible. The temperature for this shot corresponds to the brightness temperature required to yield the measured signal in these two energy bandpasses. It was found on this shot that the acquired signals for XRDs having the same photocathodes and the same aperture sizes were all within ±10% of their mean value. However, simply scaling the XRD signals by the area illuminated on the photocathodes indicated that 8-mm-diameter photocathodes detected 17% less flux then expected as compared with 5-mm-diameter photocathodes. The signal levels for the other exceptional shots, 2027 and 2028, were too poor to unfold.

The energy flux measurements assume a Lambertian emission of the x rays from a target with the nominal diagnostic aperture listed. The temporal full width at half maximum (FWHM) of the radiation pulses for the nominally good shots were obtained from the widths of XRDs signals having a S/N greater than 10. The error listed is the standard deviation between the different channels. The peak brightness temperature corresponding to the flux output from the source over the energy range of 98.1 to 1200 eV is also presented along with a one sigma error estimate.

Table 1. XRD results.

#	Target Shot #	DAS Shot #	Aperture Diameter (mm)	Peak Flux Radiated into 2π (Watts)	± Error in Peak Flux into 2π (Watts)	Radiation Pulse Width (ns)	± Error in the Pulse Width (ns)	Peak Brightness Temp. (eV)	± Error in the Peak Temp. (eV)
~~1~~	~~2025~~	~~6501~~	~~3.0~~			~~15.3~~	~~0.5~~	~~47.7~~	~~2.3~~
2	2026	6517	3.0	8.8E10	9.3E09	12.7	1.4	60.7	1.5
~~3~~	~~2027~~	~~6529~~	~~3.0~~						
~~4~~	~~2028~~	~~6542~~	~~3.0~~						
5	2029	6547	3.0	4.3E10	4.9E09	14.4	1.4	51.2	1.0
6	2030	6551	1.5	1.6E10	1.7E09	14.9	3.0	55.7	1.5
7	2031	6554	1.5	1.1E10	1.3E09	16.9	6.8	51.5	1.1
8	2032	6560	1.5	1.4E10	1.6E09	13.7	2.5	53.7	1.4
9	2033	6569	3.0	6.0E10	6.7E09	12.9	2.1	54.8	1.5

The three good target shots with a 3-mm-diameter aperture, shots 2026, 2029, and 2033, had very different peak outputs. The bolometer data for the same shots, showed much higher temperatures, by ~10 eV, and showed a factor of 1.5 times less fluence for shot 2029 as compared with shot 2026 and only 8% less fluence for shot 2033 as compared with 2026. The reason for the difference between the two diagnostics for these flux measurements is not understood. It is true that the bolometers rely on calculated values for the unfold and not on a specific calibration but the previous target series yielded very similar results between the detectors. In any case, because of the absolute calibrations, we believe the XRD results to have greater significance.

The machine performance for the target shots with a 1.5-mm-diameter aperture was acceptable. The peak fluxes for the three shots agreed within 25%. As with the bolometers, on the four highest temperature shots two had a 3-mm aperture and the other two had a 1.5-mm aperture. In addition, the pulse widths do not show a correlation such that the smaller apertures have a shorter pulse width, as might be expected if hole closure were an issue. This suggests that hole closure may not be an issue for these targets and is, in fact, consistent with diagnostic hole closure measurements showing that the hole does not close appreciably until after the peak in the radiation pulse. See Section 10 on hole closure.

The detailed spectral unfolding of the XRD signals is discussed in Section 11.2. The spectral unfold for target shot 2026 is shown in Figure 1. The upper and lower bounds, as determined for estimated 1-sigma uncertainties in the raw data, are shown along with the unfolded spectrum. In addition 50, 60, and 70 eV blackbody spectra are shown. In the sense that the measured spectrum is flatter than a blackbody with an equivalent brightness temperature, it is a typical spectral unfold. This is evident in the energy bins between 400 and 800 eV, which are factors of 2-10 to higher than the equivalent blackbody. This result is not understood, although it may be associated with temperature gradients in the target such that the lower energy channels are associated with a cooler outer temperature and the higher energy channels are associated with a hotter internal temperature.

The time-resolved brightness temperature of this target shot vs. time is shown in Figure 2, along with a LASNEX calculation. The time is defined from the 5% point of the current rise in the eight Faraday cups corrected

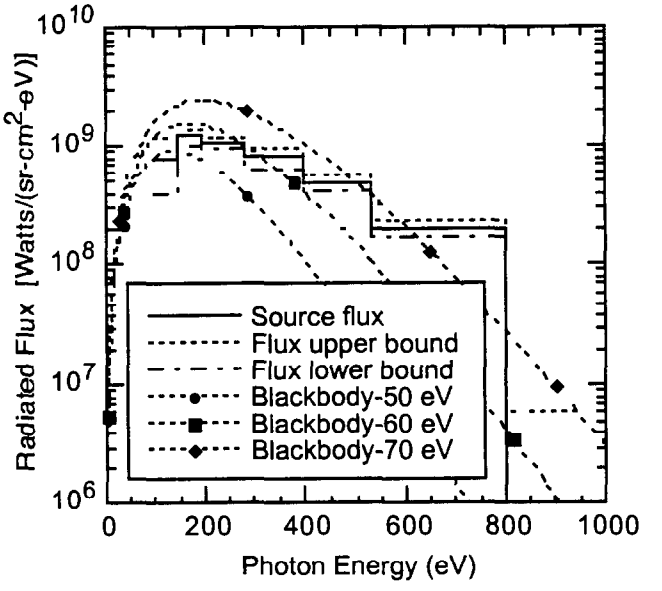

Figure 1. Time-integrate unfolded peak radiation spectrum from shot 2026.

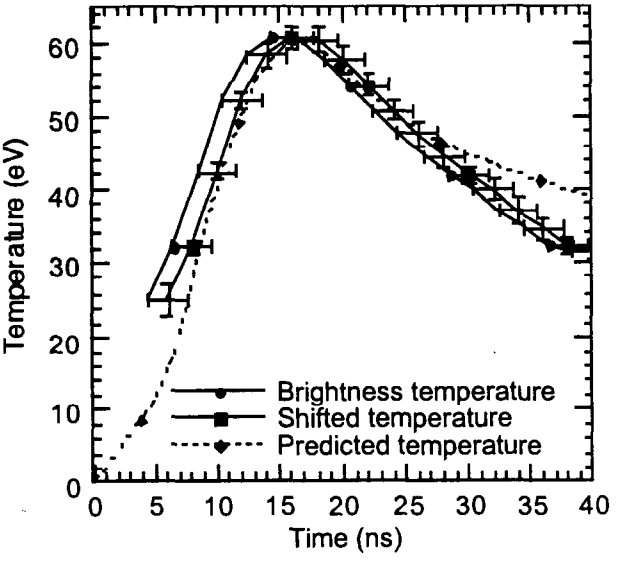

Figure 2. Unfolded, time-resolved brightness temperature for shot #2026.

to the center of the diode using a 9-MeV ion beam. The XRD data were corrected for the x-ray time-of-flight to the target, 16 ns. The amplitude and shape of the measured vs. the calculated temperatures are in good agreement with this LASNEX calculation having a peak power of 2 TW/cm^2 incident on the target. The absolute timing between the measured and the calculated temperature histories differs by ~ 1.5 ns. The experimental temperature rises earlier then predicted but is within the 1-sigma timing uncertainty of 1.6 ns for this shot. This uncertainty is dominated by the spread in the Faraday cup timing.

We have unfolded the temperature histories for the six shots as shown in Figure 3. The time origin is again set by the faraday cup signals to indicated the ion beam start time. The three targets having a 3-mm-diameter aperture are shown with solid lines and the three targets having a 1.5-mm-diameter aperture are shown with dotted lines. Error bars, which are representative for all the data, are shown only for shot 6517. For three shot (6517, 6551, and 6554) the temperature comes up ~ 6 ns after the start of the ion beam. For the three other targets the temperature rises ~ 2 ns later. This could be simply explained by the error bars on the timing, which are ~ ±2 ns. The timing difference could also be due to beam transport issues associated with beam sweeping, vertical and horizontal aiming, and azimuthal variations.

We have compared the shapes of the measured temperature histories with the LASNEX prediction in Figure 4. The amplitudes have been normalized and the timing shifted to line up the peaks. The measured temperature histories are fairly consistent in shape, indicating that the temperature profile is insensitive to the range of peak target temperatures observed. For the two shots that were analyzed out to 40 ns (6517 and 6569) the late-time temperature histories fall faster

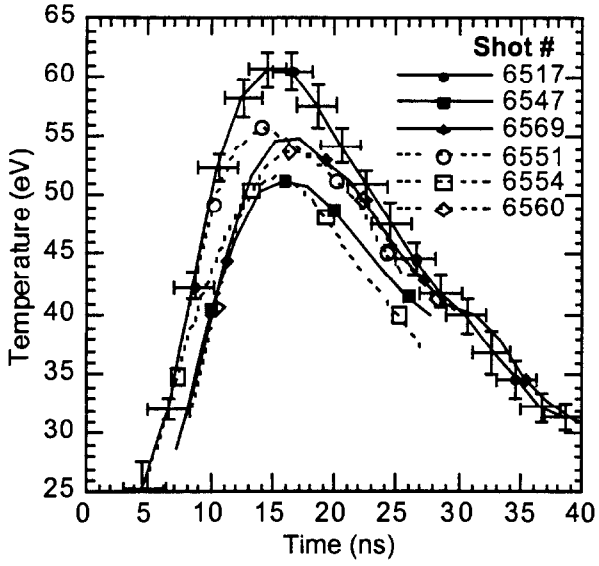

Figure 3. Unfolded time resolved temperature histories for six target shots.

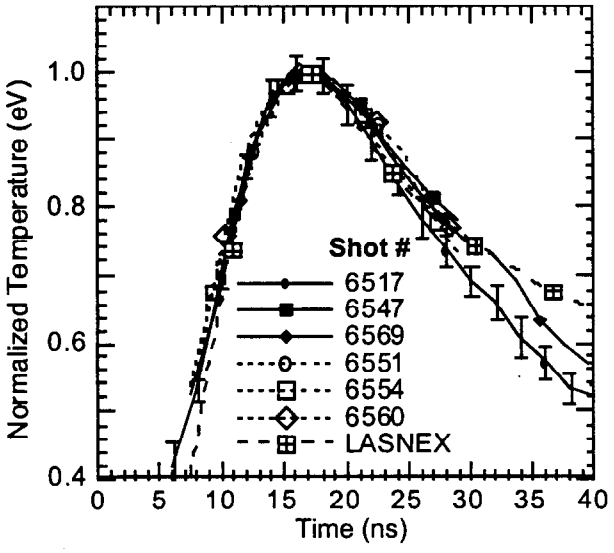

Figure 4. The shapes and time histories for six target shots are similar.

than the LASNEX prediction. This may be due to hole closure. In Section 10, on hole closure, the aperture for shot 6569 is seen to go from 3 to 2.4 mm in diameter at late-time, >20 ns. This would cause a 12% increase in the late time temperature recorded, bringing the normalized temperature for this shot in very good agreement with the calculation.

The analysis of the spectral shape shown in Figure 1 for target shot 6517 as a function of time is shown in Figure 5a - 5c. These figures show the measured spectrum at 10.5 ns into the power pulse (rising temperature), at 14.5 ns (peak temperature), and at 22.5 ns (falling temperature). The corresponding brightness temperatures are 52, 61, and 51 eV. In addition, the equivalent blackbody spectral brightness temperature profiles are also shown. A high energy tail is seen in all the unfolded spectra.

All of the cylindrical target shots show this high energy tail when compared with their equivalent blackbody, as shown in Figure 6a - f. The reason for this spectral behavior is not understood. One explanation, as previously stated, is that there is a temperature gradient, from colder to hotter, as one looks into the target along the XRD line of sight. The opacity of the colder material, perhaps from foam jetting out of the hole, or from the same material that leads to the nonuniformities in the x-ray images of the targets, absorbs the lower-energy photons from the hotter material but not the high-energy photons. This would imply a hotter temperature inside the target than measured, ~ 70 eV based on matching the flux into the higher energy channels. Another explanation could be a non-Planckian tail on the photon distribution, perhaps due to the energy deposition mechanism.

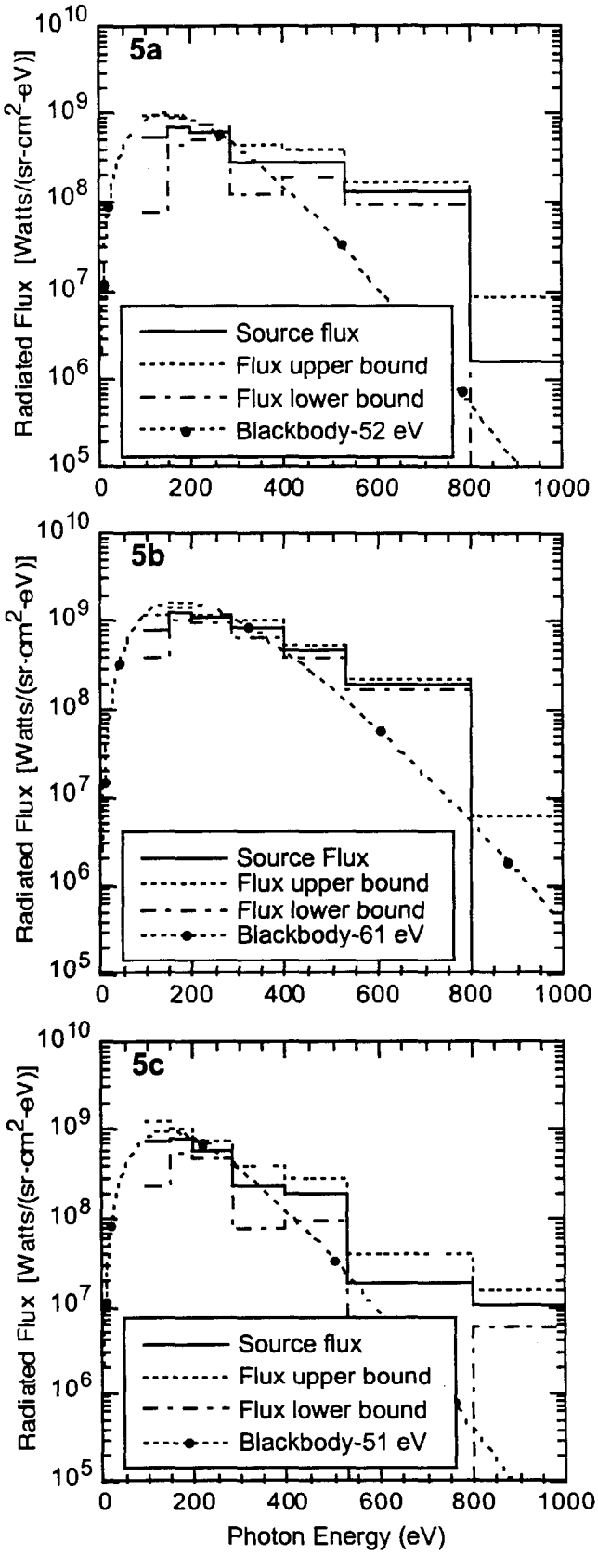

Figure 5a. The unfolded spectrum from shot 6517 at 10.5 ns, **(5b)** 14.5 ns, and **(5c)** 22.5 ns into the power pulse.

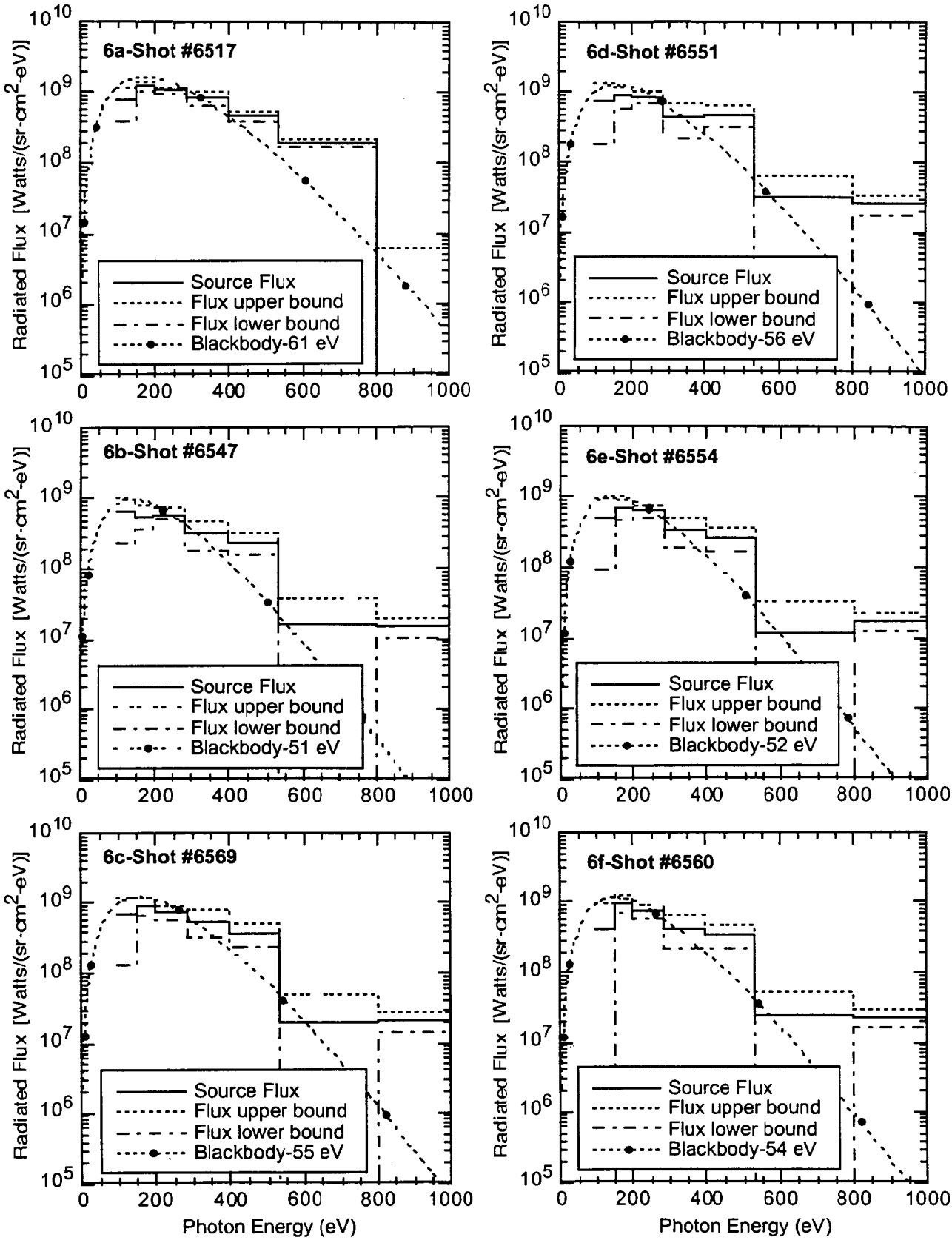

Figure 6a-f. Unfolded flux profiles at peak power throughout the shot series. The target shots with a 3-mm-diameter diagnostic aperture are on the left and the those shots with a 1.5-mm-diameter diagnostic aperture are on the right.

When overlaying the spectral unfolds at the peak in the radiation emission from different shots, as shown in Figure 7, similar profiles are observed. The most apparent difference is for the highest temperature shot which shows ~ 10 times the flux in the 500-800 eV bin than the other shots.

It is interesting to note that on the previous series with the open cone targets the spectrum did not have a high energy tail. This is seen in Figure 8 showing the unfolded spectra from the cylindrical target shot 6517 with shot 5942 from the cone target series. The brightness temperatures for both of these shots is ~60 eV. The reason for this difference is not understood.

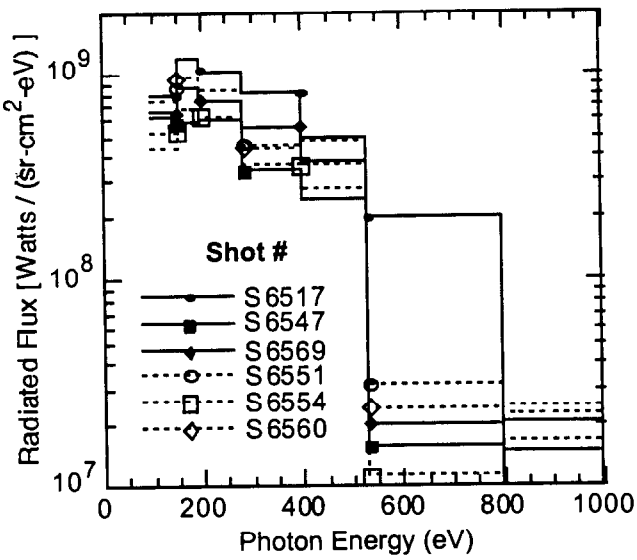

Figure 7. Unfolded flux profiles at peak temperature. Target shots with a 3-mm aperture are shown with solid lines while shots with a 1.5-mm aperture are shown with dotted lines.

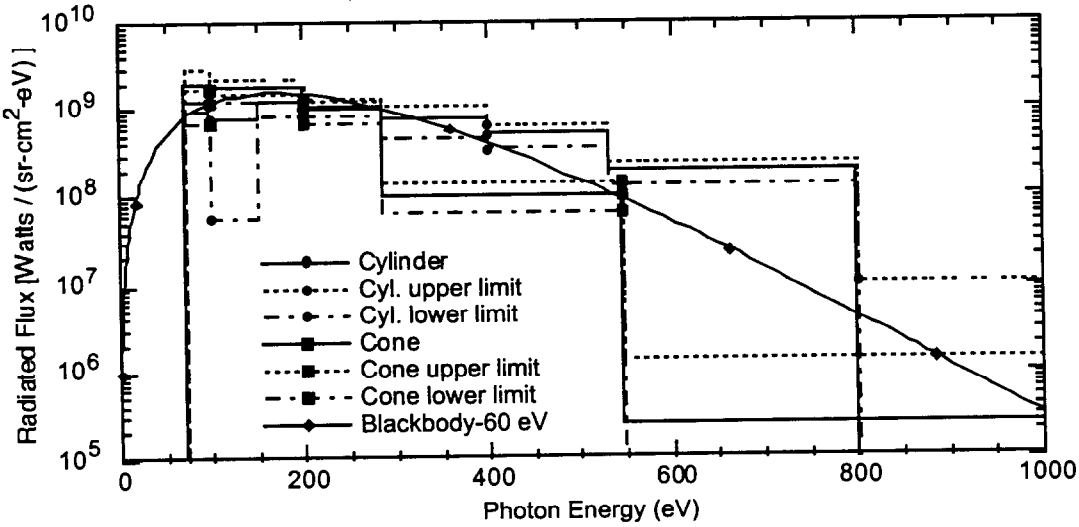

Figure 8. Unfolded spectral comparison between cylindrical and cone targets at peak temperature.

Experimental Setup

Thirteen filtered XRDs were fielded on the TAR94-1 series in two eleven channel detector arrays known as DAX1 and DAX2. The other 9 channels were used for p-i-n detectors. These detector arrays are on different line of sight pipes at 472 cm from the source at 6° and 9° from vertical, respectively. The electrical current through the XRDs measured is a function of the photon flux incident on the photocathode. The spectral sensitivity is a product of the filter and photocathode response. These detectors response fast enough, ~0.5 ns, so that they yield a measure of the incident photon flux. The design of these detectors will be briefly discussed next.

The detector heads, shown schematically in Figure 9, consists of an N-connector body into which a Teflon insulator is inserted to support the negative 1000 volt bias applied to the photocathode. Some photocathodes are made from diamond turned aluminum. The stalk on the photocathode is the center pin of the N-connector. Carbon photocathodes are made from disks of polished vitreous carbon which are silver epoxied to a nickel-plated aluminum piece provide the center pin of the N-connector. A Teflon spacer ring maintains a 0.5-mm gap between the photocathode and the anode mesh. The nickel anode mesh is 5-μm thick with a 90% open-area ratio. A limiting aperture, (5-or 8-mm-diameter) restricts the illuminated photocathode area. A locking nut holds the assembly together.

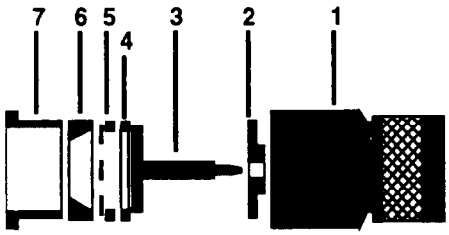

1. "N" Connector Body
2. Teflon Insulator
3. Photocathode
4. Teflon Spacer
5. Anode Mesh
6. Limiting aperature
7. Locking Nut

Figure 9. XRD detector assembly.

The detector is directly coupled to an N-connector vacuum feed-through in the DAX housing assembly shown in Figure 10. The photocathodes were DC-biased to negative 1000 volts through Picosecond Pulse Labs 5532A insertion tees in the PBFA-II data acquisition room through long 50-ohm cables (~ 98 ns of 0.5" Heliax and 59 ns of RG9914). The bias cables also acted as part of the signal cable run. The output signal was coupled through a 12-nanofarad capacitor in the insertion box to Tektronix DSA640 digital oscilloscopes using 26.5 ns of RG223 cables. Testing of the relative timing between the XRD channels yielded a standard deviation of 0.25 ns and a spread of 0.5 ns. Timing corrections to the detectors,

baseline shifts, cable compensations, and droop corrections to account for the capacitive coupling through the insertion box were performed on the raw data signals.

The XRD diagnostics were designed into detector housings as shown in Figure 10, with the diagnostics in one of the two arrays. Apertures in this setup are located in a fast closing valve that protected the diagnostics from target debris. The apertures (~1.27 cm diameter), are in a filter holder (~ 1.0 cm diameter), and in a magnet holder assembly (~1.9 cm diameter). The magnets prevented photoelectrons from the filters and ions from the source from reaching the XRDs. The filter apertures combined with the apertures on the XRDs (0.5 or 0.8 cm diameters), limited the clear field of view of the target by the XRDs to a diameter of 4.0 cm or 2.2 cm respectively. The target aperture sizes were only 3 mm in diameter and so alignment was not difficult. Spatially-resolved images of the target verified the localization of the x-ray flux from the target aperture for photon energies above ~ 200 eV.

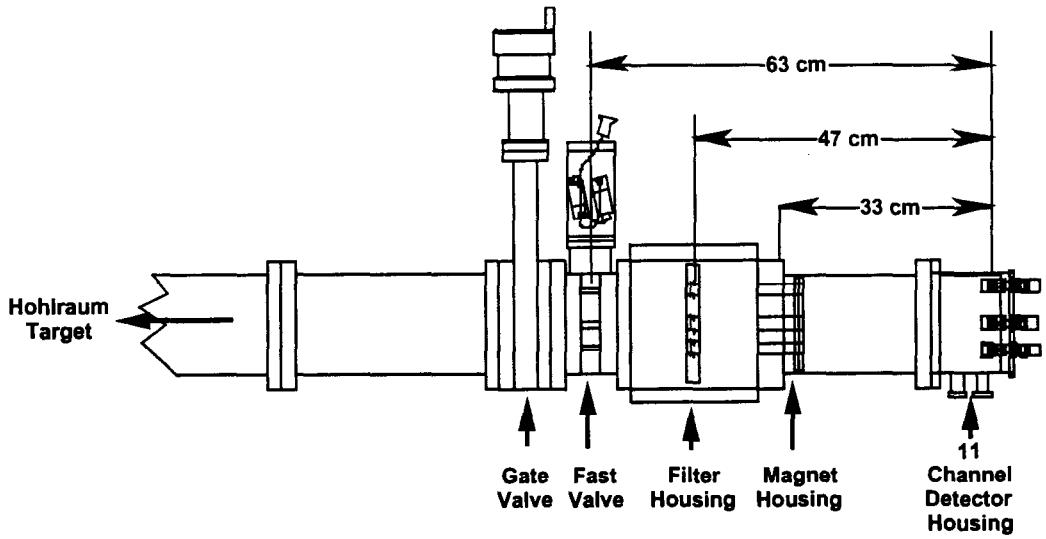

Figure 10. The 11-channel x ray detector (DAX) set up.

Filtered XRD Responses

The 13 filtered XRD responses were chosen to give information on the soft x-ray output in the range of ~ 70 to 1000 eV. These responses were set by the choice of thin x-ray filter materials and the choice of photocathode materials. The nominal responses for the 13 XRDs are shown in Figure 11a - c. Significant sensitivities of these detectors exist above 1000 eV; hence, background channels are used to infer the contribution to the lower energy channels from the higher energy photons from the source. Diamond polished vitreous carbon and diamond turned aluminum photocathodes were used. The same set of XRDs were used for all of shots in the series. All but two detectors were calibrated at the National Synchrotron Light Source (NSLS) at Brookhaven National Laboratory on the Los Alamos National Laboratory vacuum ultraviolet beam line U3C. One of the detectors (XRD 26) used a calibration performed earlier at another

facility and another one (XRD 34) used the response from a similar carbon photocathode XRD. The detector calibrations were performed with photon energies between 180 - 1550 eV. Typical XRD calibrations for these photocathodes are shown in Figure 12. For all of the calibrated XRDs the responses used in the data analysis were fits to the individual XRD calibrations. The fits were obtained by scaling mass absorption coefficients for the photocathodes to the calibration data in amps/MW. This is consistent to first order with models for the photocathode responses.[1] The quality of the fits can be seen in Figure 12. The fits to the responses of the aluminum photocathodes were allowed to have carbon, oxygen, and fluorine components. The oxygen component was always present as is clearly seen by the enhanced sensitivity across the oxygen absorption edge. The fluorine component was present most of the time and was ascribed to contamination with tetrafluoroethane present in effidusters(handheld gas-propellant) used to clean them. The carbon photocathodes were allowed to have oxygen and hydrogen components.

It is important to note that extrapolations of these fits, based on the mass absorption coefficients, are used below 180 eV, a region in which there are 3 primary channels, aluminum, silicon, and boron. Above 1550 eV extrapolations of the fits are also used, a region for which there is one background channel that has a significant response.

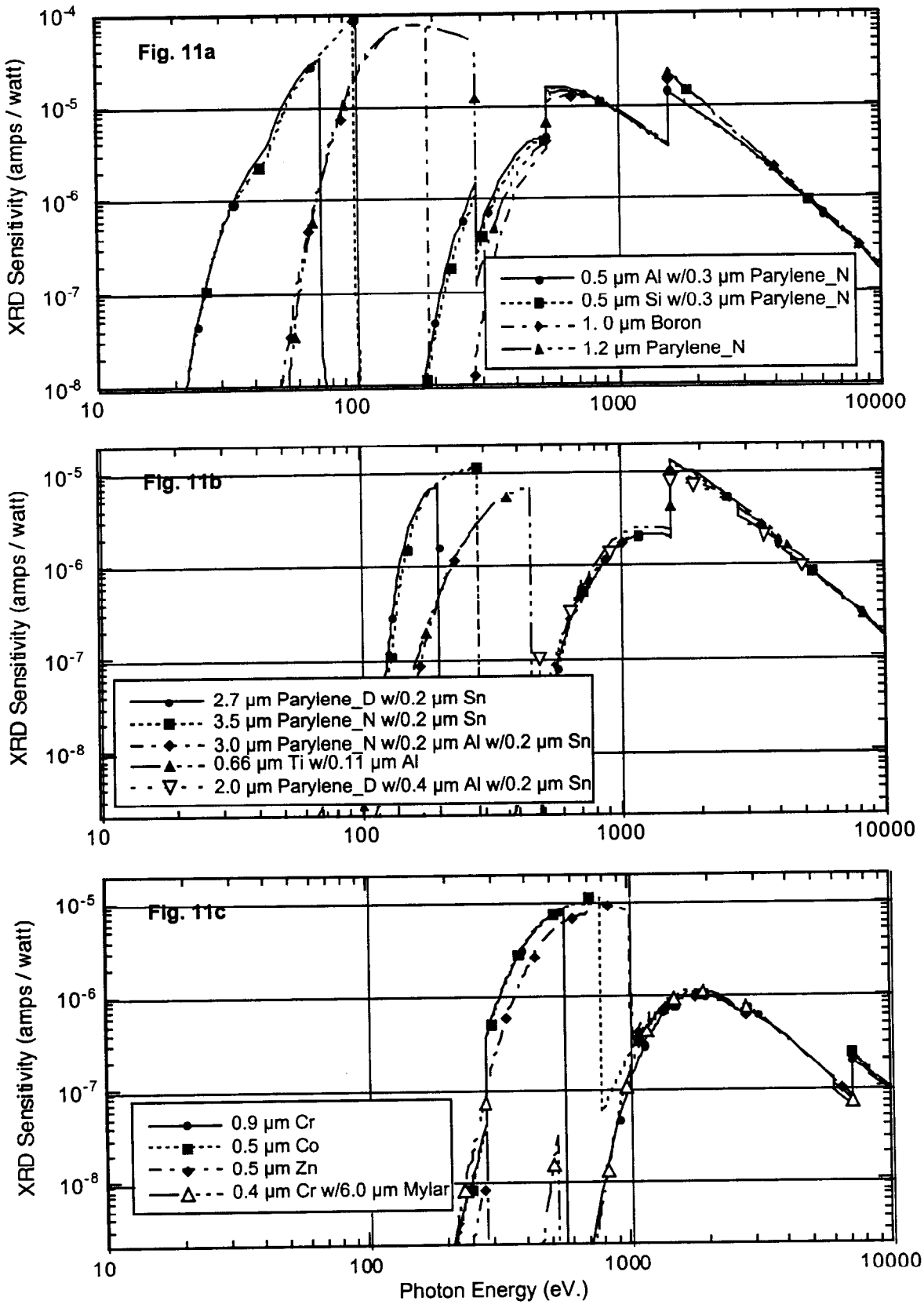

Figure 11a-c. Nominal XRD sensitivities used.

The fits to the calibrated responses of the nine aluminum photocathode XRDs are shown in Figure 13. There are two basic responses, six contaminated with the fluorine and three uncontaminated. The presence of a fluorine-K-edge in the data is taken as evidence for fluorine contamination. XRD 26, an uncontaminated XRD, appears to have an anomalously high sensitivity above the aluminum K-edge, although this is an extrapolation. This detector was associated with a boron-filtered channel and, given the unfolded spectrum, most of its response was to photons less then 1000 eV.

Four carbon XRDs responses are shown in Figure 14. The sensitivities are matched to within ± 3%, above the carbon edge at 284 eV. The individual fits to the calibrations for XRDs 35, 36, and 37 were used. For XRD 38, which was also used but not calibrated, the fit for XRD34 was used.

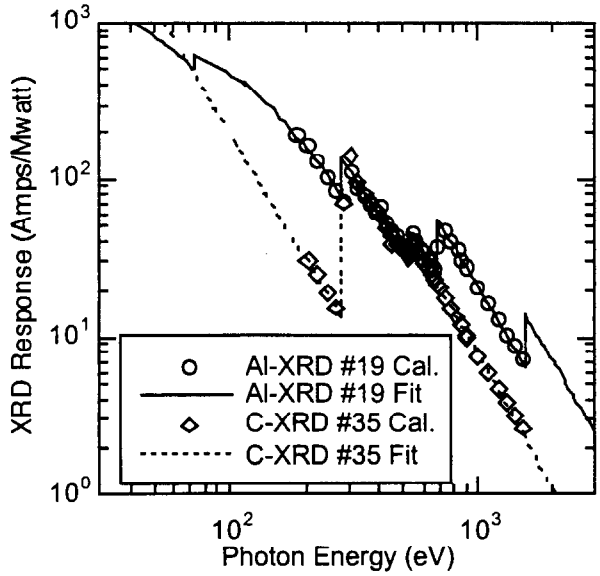

Figure 12. Typical calibration data and fits to the data for an aluminum and carbon photocathode.

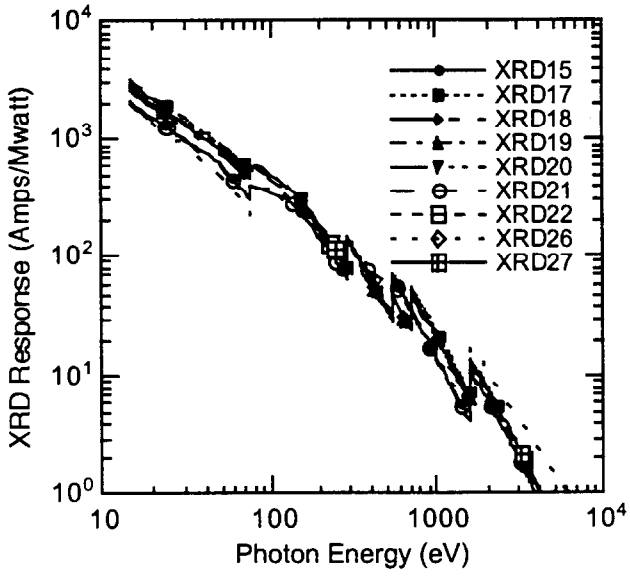

Figure 13. Responses for all of the aluminum photocathodes used.

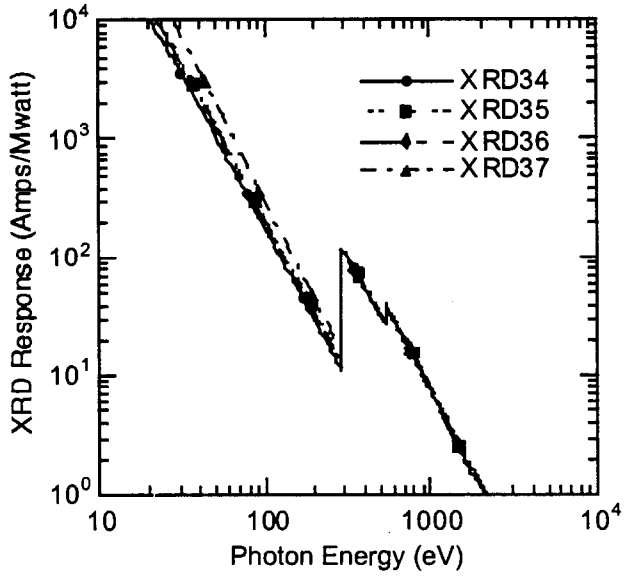

Figure 14. Responses for the carbon photocathodes.

This pre-PBFA-II shot series calibration data is generally considered to be accurate to ±10%. Exposure to the PBFA-II environment is suspected of altering these responses. Postshot series calibration of the detectors is thus desired and was done for the carbon photocathodes. A comparison of the pre- vs. post-calibrated response for the carbon photocathodes is shown in Figure 15. The response of the detectors varied by as much as 35% above the carbon edge and as much as 3.5 below. The analysis to date used only the precalibrated responses for these detectors. The effect on the unfolds due to large changes in the low energy response may be small since all of the carbon XRDs were filtered for high energy responses above the carbon edge. The change in the response above the carbon edge depends on the detector. Two of the channels increased in their response and one decreased. The largest change in this region is a 25% increase in sensitivity for one of the detectors. This increase in sensitivity is in the correct direction to explain the high energy tail in the unfolded spectrum, but is too small to explain the factor of 2 - 10 difference observed compared to a blackbody.

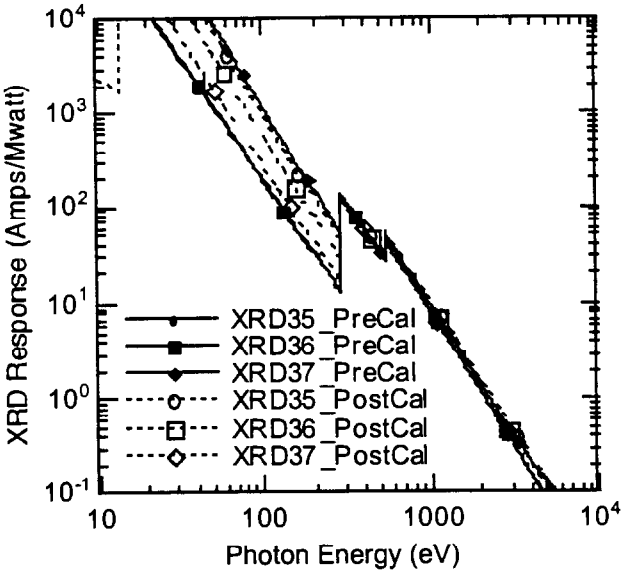

Figure 15. Pre- vs. post-calibrated carbon photocathode responses.

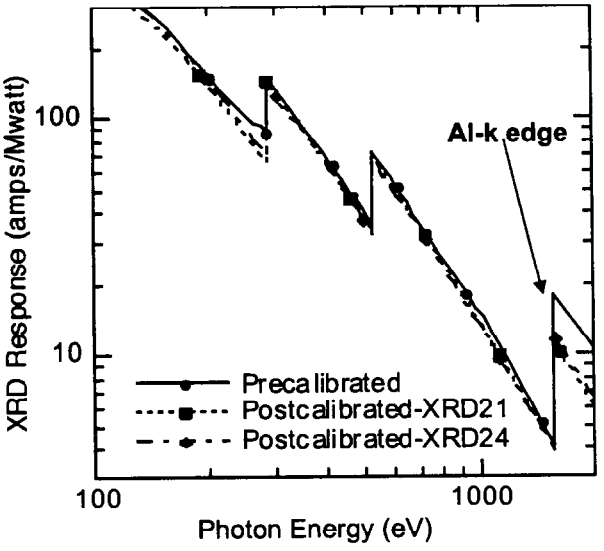

Figure 16. XRD pre- and post-calibrations.

For the aluminum photocathodes no postshot calibrations were available. An estimate of the changes that might be expected come from the previous target series, 93-1, where two aluminum photocathodes which were used for all 10 shots, XRD21 and XRD24 had preshot and post shot calibrations. Their preshot calibrations agreed to within 20%, and were fit to a single response function. Their postcalibrations were fit separately, and as can be seen in Figure 16, there is good agreement between the pre- and post-calibrations for these detectors below the aluminum K edge. The difference below this region is within 20%. The good agreement observed may be skewed from the real situation in the

sense that these two XRDs appeared to have the least contamination on their surfaces after the 93-1 target series. The real answer as to the effect of the PBFA-II environment on the detector response awaits our next target series.

In the unfold of the data it became clear that the response of the lowest energy channels, below 100 eV, yields an anomously large low energy peak, as discussed later in this section. To understand the response in this region, calibrations were done after the experiment on new aluminum photocathodes at the National Institute of Standards and Technology (NIST), on the SURF II facility. These calibrations indicated a factor of two enhancement in the response of the aluminum XRDs below the aluminum L-edge at 73 eV as compared with the extrapolated responses used for this experiment.

In addition, extensive calibrations were performed on the x-ray filters, which are also a critical component in defining the spectral response of the detectors. All of the filters had an alpha spectrometer characterization of the filter thickness. In addition, x-ray calibrations were performed, primarily on a Henke source facility at the LLNL Nova facility, but also at the NSLS facility. These calibrations are discussed in the section by T. A. Alberts. The unfolding of the detector response from the acquired data is discussed in the next section.

References

[1] B. L. Henke, J. A. Smith, and D. T. Attwood, J. Appl. Phys. 48, 1852 (1977).

11.2 X-ray Diode Unfolding Procedures - D. L. Fehl

The filtered XRD spectrometer faces a different x-ray environment in a PBFA-II hohlraum experiment than in a calibration. For example, at a calibration source incident photons are nearly monochromatic during the sampling interval and are of relatively low intensity. In a PBFA-II experiment the incident photon flux is orders of magnitude larger, and the x-ray photons comprise a time-varying spectrum *S(E,t)*. The PBFA-II environment also includes x-ray, electromagnetic pulse (EMP), and debris backgrounds, which are not present at calibration facilities. Nevertheless, for PBFA-II experiments if one can argue that if (1) photons of differing energy contribute independently to the current in each XRD, (2) the x-ray flux incident on each XRD is not large enough to cause electron charge density (saturation) effects, and (3) the rise- and fall-times of the x-ray flux are not significantly faster than the response time of the gauge and its recording system, then the data D_i collected in the i-th channel of the spectrometer due to *S(E,t)* can be written as:

$$D_i(t) = \int_{E_{min}}^{E_{max}} S(E,t)R_i(E)dE + \varepsilon_i \qquad (1)$$

for channels $i = 1,2, \ldots 13$. Here the response functions, $R_i(E)$, for each filter-XRD pair (channel) are estimated from the calibrations. The ε_i terms represent experimental uncertainties or perturbations to the data. Such noise terms may fluctuate from channel to channel.

Eq. (1) can be interpreted in two ways. In a practical sense, the data arise as a set of averages over the spectrum, with the response functions as weighting factors. That is, nature produces the physically appropriate spectrum, and the experiment performs the forward integrals, in addition to adding uncertainties. In a more formal sense, Eq. (1) is a simultaneous system of first-order Fredholm equations[1] distinguished by channel i and time t. For each t, one can regard this system as a linear transformation (or mapping) of the space of all integrable spectral functions S that are defined on the domain $[E_{min}, E_{max}]$ into $M = 13$-component sets of data.

Given the finite data D_i in Eq. (1), one wishes to "recover" the spectrum S. This desire poses several difficulties, especially if one is seeking a complete (analytic) specification of S. The first problem relates to the response functions. As noted above, these weighting functions are averaged with the spectrum over a finite energy domain, and this operation irrecoverably "washes out" or distorts details in the incident spectrum. Thus, resolution is lost. Even if one could measure S itself at a finite number of energy points by sufficiently narrow response functions, the Whittaker-Shannon Sampling Theorem restricts the reconstruction of S between sample points. A second difficulty in recovering S is that inverse or unfolding problems represented by Eq. (1) are, in general, "ill-posed." That is, for arbitrary data sets D_i there may be no solutions at all or no unique solutions. For example, the irreducible noise terms ε_i may be sufficiently large that no physically acceptable spectrum can yield the data via the specified integral equations. Alternatively,

in addition to the real source spectrum there is an infinite set of non-trivial functions S (often wildly oscillating and physically unacceptable) which also map into the collected data. In general, one needs information (*e.g.*, a theoretical model) *in addition* to the data to sort out undesirable spectra.

In the PBFA-II hohlraum experiments, little *a priori* information was available concerning the analytic form of S. That is, while the measured spectrum was expected to be roughly a filtered blackbody spectrum in shape, it was not known if the blackbody term could be represented by a single temperature or a distribution of temperatures. Moreover, the filtration of the spectrum depends on the temperature distribution of material within the hohlraum and, in principle, on plasma closure of the viewing aperture. Few of these variables were measured independently. Thus, we approximated the source spectrum S detected in the filtered-XRD spectrometer with a suitably flexible linear combination of N basis functions $B_j(E)$:

$$S(E,t) \cong \sum_{j=1}^{N} S_j(t)\, B_j(E) \tag{2}$$

The fit coefficients $S_j(t)$ are to be determined from the experimental data. For initial unfolds, a contiguous set of histograms (first-order B-splines) were chosen as the basis functions. These arbitrarily chosen functions define bins in the energy domain over which the approximating spectrum is constant. The system was generally overdetermined ($N < M$). Other basis functions were considered: a set of black bodies of prescribed temperatures and an underdetermined (*i.e.*, $N > M$) histogram system.

Using this approximating function for the unknown spectrum S, one rewrites the system of equations (1) as

$$\begin{aligned} D_i(t) &= \int_{E_{min}}^{E_{max}} \left(\sum_{j=1}^{N} S_j(t) B_j(E) \right) R_i(E)dE + \varepsilon_i \\ &= \sum_{j=1}^{N} S_j(t) \int_{E_{min}}^{E_{max}} B_j(E) R_i(E)dE + \varepsilon_i \\ &= \sum_{j=1}^{N} S_j(t) R_{ij} + \varepsilon_i \end{aligned} \tag{3}$$

where,

$$R_{ij} = \int_{E_{min}}^{E_{max}} B_j(E) R_i(E)dE \tag{4}$$

At each time step Eqs. (3) constitute a set of linear equations with constant coefficients. This reduction of Eqs. (1) is called the product-moment method.

While reducing Eqs. (1) to Eqs. (3) allows one to use matrix manipulation techniques in constructing an approximate solution, the resulting system of linear equations is still not without difficulties. First, Eqs. (3) remain ill-posed: that is, the set of basis functions is certainly not unique, and one could choose $N > M$. Second, even if one does obtain a unique set of coefficients $\{S\}$ for a particular choice of basis functions, the resulting solution may still not approximate the real spectrum very well. This behavior is particularly evident with histograms of large width, compared to the scale over which significant changes in the spectrum and response functions occur. Then $S_j R_{ij}$ becomes a poor approximation to $\int R_i(E)S(E)dE$ over the histogram in question. The values S_j may then disagree unacceptably with the average of the real spectrum across several histogram basis functions, since Eqs. (3) are coupled. This problem may be ameliorated by choosing either higher-order basis functions or more and smaller bin widths. But both these schemes quickly lead to underdetermined formulations, which we tried to avoid for initial unfolds. A third characteristic of the coupled Eqs. (3) is that although the noise terms ε_i may be themselves statistically independent, the uncertainties in the coefficients S_j (computed by simple error propagation) are not independent. Thus, further computations with the approximate solution of Eq. (2) (such as simple integrals or integrals weighed by response functions) must include the covariance matrix.

Unless the response functions are particularly simple, most algorithms for obtaining the unfold parameters S_j do not attempt a direct solution of Eq. (3). Rather, one accounts for the noise terms by reformulating Eq. (3) as a least-squares problem. That is, one minimizes the residual r^2 between the data D_i and the data predictions $R_{ij}S_j$ by adjusting the unfold parameters S_j.

$$r^2(D_1,\ldots,D_M;S_1,\ldots,S_N) = \sum_{i=1}^{M} \left\{ \frac{D_i - \sum_{j=1}^{N} R_{ij}S_j}{\sigma_i} \right\}^2 \qquad (5)$$

The constants σ_i^2 represent the variance in the noise terms ε_i. The minimized residual may then be used to estimate the "goodness of fit" of the data predictions from the spectral solution to the data. There are many algorithms for dealing with Eq. (5). While most reduce the minimization to solving normal equations, a few iteratively perturb the emerging solution. Some require trial spectra. Others add regularizing conditions.[1] Formulations using Maximum entropy and statistical maximizations instead of least-squares minimization are also available.[1]

In this work, Eq. (5) was minimized with the UFO (UnFold Operator) code.[2] Designed by F. Biggs and L. Kissel at Sandia National Laboratories, this computer program is applicable to many types of weighted least-squares problems, including curve

fits, integral equations, deconvolution, etc. Basically, UFO reduces the residual in Eq. (5) to a set of linear (normal) equations, which are then solved by matrix manipulation using the LSEI algorithm described by Lawson and Hanson.[3] To run the code, one supplies the data values D_i , the uncertainty weights $1/\sigma_i^2$, the response functions $R_i(E)$, the domain $[E_{min}, E_{max}]$ over which the solution is desired, and the approximating basis functions $B_j(E)$. The code then constructs the matrix elements R_{ij}. One may also specify point-wise constraints (e.g., $S(0) = 0$) on the solution, constraints on the derivatives (smoothing equations), and limit the solution to non-negative values. Like the similar Singular Value Decomposition method,[4] the code will usually execute even for under-determined systems. As a measure of goodness-of-fit in overdetermined systems, UFO calculates the minimized residual r_{min}^2 with the solution parameters and specified variances, together with the probability of obtaining a similar χ^2 value for independent and normally distributed data uncertainties (M - N degrees of freedom). Finally, the code constructs the covariance matrix for the unfold coefficients S_j; in general, these coefficients are strongly correlated by overlapping response functions. Also available from UFO is the integral of the product of the approximate solution with an arbitrary function $F(E)$. The uncertainties for such integrals are also propagated using the covariance matrix of the solution.

Collecting the time-dependent XRD data and characterizing the uncertainties are the first major steps in the unfolding process. Figure 1 shows three XRD voltage traces from PBFA-II shot 6517. These traces indicate roughly the range of signals one encounters from the filtered-XRD spectrometer and some of the interfering phenomena which need either correction or characterization. Typically, the cable-compensated XRD voltage traces show rise-times of ~7 ns (10-90%), pulse widths of 10-20 ns, and fall-times of 10-20 ns (90-10%). In these traces, the signals have been aligned to a common reference time to within 0.5 ns; voltage attenuators have been accounted for and capacitive droop corrections due to the bias or isolation box have been made. Some of the channels required further corrections. For example, a low XRD signal (Figure 1c) may ride on a background signal, possibly due to bremsstrahlung radiation (which will be produced wherever appreciable electron loss occurs in the accelerator such as in the current feeds to the diode and in the AK gap) interacting with the signal cables. For this study, such backgrounds were approximately constant during the XRD pulses of interest and were subtracted out as baseline-shifts. On the other hand, cable noise could not be subtracted out and was characterized for inclusion in Eq.(5). The RMS value of this noise was estimated from the baseline traces before the shot and ranged from 0.5% - 4% of peak voltage. Jitter in the recording system was measured to be only ~0.25 ns (compared to ~ 7 ns rise time),[5] and was ignored as an additional source of error.

For the time-dependent unfolds, the background-corrected signals were sampled at a common set of times. Usually, once the peak time is identified, one selects sampling times at 2 ns intervals before and after the peak until the signals drop below about 15% of peak. This procedure will often allow 3-4 points in the rising portion of the curves and at least about 5 points in the tail of the signal. Terminating the samples at the 15% level normally prevents negative data values caused by cable noise at low signal levels. The numerical sampling was done with the UFO function UTERP, which computes a linear interpolation between successive points in the digitized signals.

It is convenient to convert the time-sampled voltage traces to different units in doing the unfolds. The signal voltage V_i (in volts) obtained in the i-th XRD channel depends on the spectrum $S(E)$ (W/(sr-cm^2-eV)), the response function $R_i(E)$ (A/MW), and geometric factors as given in Eq. 6.

$$V_i = \int_{E_{min}}^{E_{max}} S(E,t) R_i(E) dE \left\{ \frac{A_s A_i}{r_1^2} \cos\theta_I \right\} (\alpha Z) \qquad (6)$$

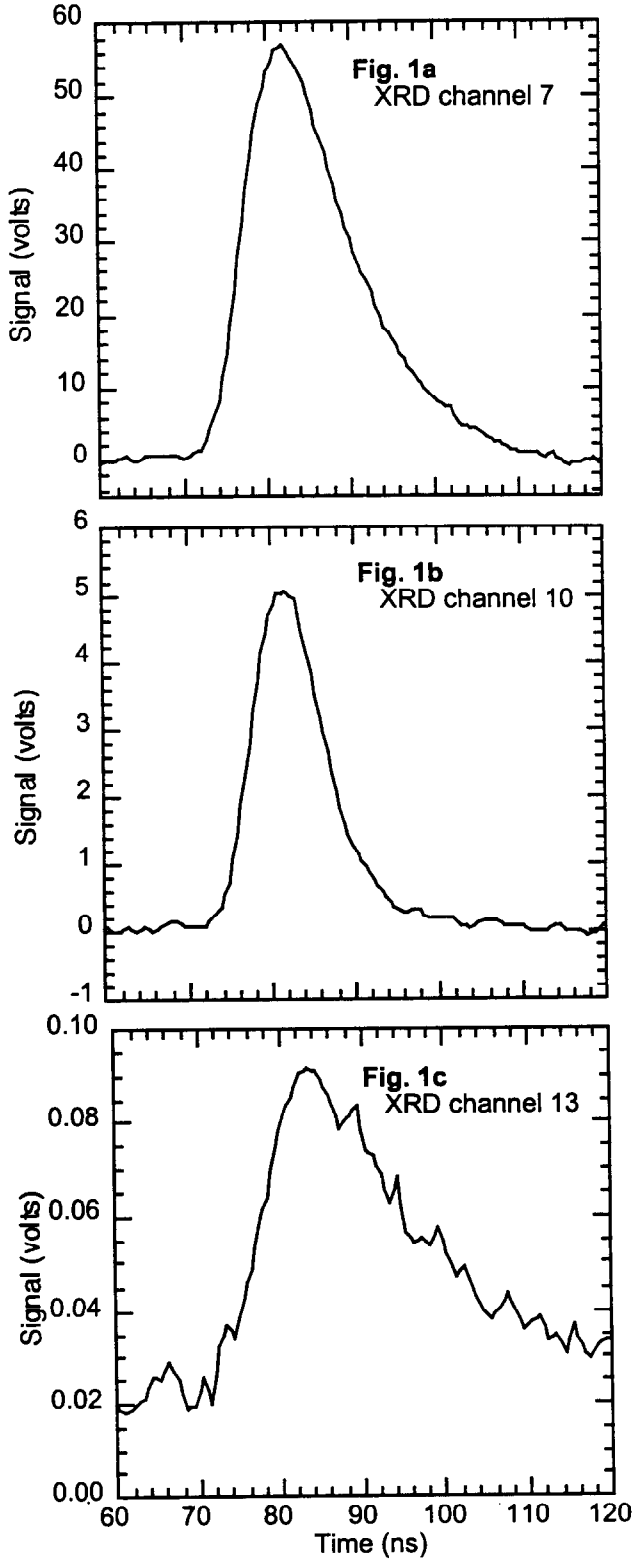

Figure 1. Three representative XRD traces from PBFA-II shot #6517.

Here A_S is the viewing area of the source (cm^2), $A_i \cos\theta_i / r_i^{-2} = \Omega_i$ (sr) is the off-normal solid angle of the i-th XRD channel, Z is the impedance of the recording system (50 Ω), and $\alpha = 10^{-6}$ MW/W. We define the reduced data $D_i(t_k)$ ($\mu A/sr\text{-}cm^2$) at each interpolated sample time t_k as:

$$D_i(t_k) = \left(\frac{r_i^2}{A_s A_i \cos\theta_i \, \alpha \, Z} \right) V_i(t_k) \qquad (7)$$

This conversion groups all of the experimental sources of uncertainty into the data, except for the errors in the response functions. Figure 2 shows the reduced data at peak time for PBFA-II shot 6517 as a function of channel number.

Reducing the experimental data to the above units also makes possible direct comparisons to forward-model simulations. For example, Figure 2 also shows *simulated data* from a set of blackbody spectra $\Phi_{BB}(E,T)$ with prescribed temperatures T of 50, 60, and 75 eV. These UFO simulations were made with continuous source functions and numerical integration of Eq. (1). Such forward calculations suggest several important inferences about the source spectrum at peak time in PBFA-II shot 6517: (1) The experimental data generally follow the shape of the simulated data as a function of channel number. This agreement suggests that there are no gross problems with the experiment and that the peak spectrum is probably not too much different from a blackbody spectrum. (2) If the peak spectrum actually were a pure black body spectrum, then one would expect its characteristic temperature to be between ~50 and ~75 eV. (3) A close comparison of the experimental and simulated data reveals systematic deviations from one channel to the next, and so it is important to attempt some reconstruction of the source function by unfolding.

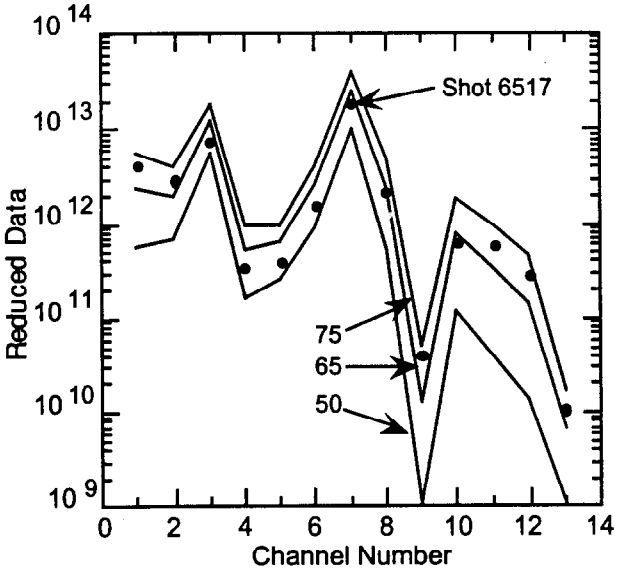

Figure 2. Reduced data as a function of filtered-XRD channel. The solid lines are from simulated 50, 65 and 75 eV blackbodies. The experimental data from shot 6517 are shown as the series of individual dots.

The choice of unfolding parameters [E_{min}, E_{max}, and $\{B_j(E)\}$] depended on several auxiliary measurements and conditions. Since we could only argue theoretically for the constraint $S(0) = 0$, the lower energy bound, E_{min}, was set to 0. The upper bound, E_{max}, was suggested by the reduced data at peak time in Figure 2, theoretical calculations, and signals from heavily filtered p-i-n detectors, which also viewed the x-ray source. From these measurements, one expects no blackbody spectra of higher temperature than 75 eV and no appreciable energy flux from photons of energy > ~ 1 keV. E_{max} was thus arbitrarily set at 1200 eV. This upper bound includes all but 0.01% of the total flux from a 75 eV blackbody. First-order, non-overlapping B-splines (histograms) were chosen as the standard basis functions since these functions require fewer degrees of freedom in the unfold than higher order B-splines. A total of 9 such basis functions spanned the energy domain. The choice of joints (or bin boundaries) was guided by K-edges in the XRD response functions. For simplicity we wished to have only one set of basis functions to approximate the time-changing source spectrum at all the sampled times but other choices of unfold parameters yielded similar results, as seen in Table 1.

This formulation of the unfold problem was then applied to simulated data. Figure 3 shows the results of unfolding data simulated from selected blackbody spectra with characteristic temperatures from 25 - 75 eV. The simulated data have no added noise signals (other than numerical roundoff) but were assumed to have the same fixed *relative* uncertainty in each channel (e.g., σ_i = 20%D_i for all channels i). Given 75 eV as the highest temperature, 25 eV was chosen as the lowest because the data signals from a 25 eV blackbody would roughly produce data signals of $(25/75)^4$ or ~1% of the data signals from the 75 eV blackbody. This ratio is smaller than the noise-to-signal ratio for PBFA-II shot 6517. The unfolded spectra qualitatively fit the blackbody source functions reasonably well. However, there are some distortions, notably in the first bin (which is constraining the condition $S(0) = 0$, as noted above) and in regions where the original spectrum is changing rapidly. Table 1 shows the flux integrals for the original blackbody and the unfolded spectra. If one

Table 1. Comparison of integral fluxes for blackbody source spectra and histogram unfolds from simulated data.

Blackbody Temp. (eV)	$\int F_{BB}(E)dE$ (W/(sr-cm^2))	$\int$Unfold (W/(sr-cm^2))	Percent Flux Difference
Full integrals (0 - 1200 eV)			
75	1.04×10^{12}	1.03×10^{12}	-0.96%
65	5.84×10^{11}	5.73×10^{11}	-1.88%
60	4.24×10^{11}	4.11×10^{11}	-3.07%
50	2.05×10^{11}	1.91×10^{11}	-6.83%
25	1.28×10^{10}	0.85×10^{10}	-33.59%
Partial integrals (98.1 - 1200 eV)			
75	9.64×10^{11}	9.78×10^{11}	1.45%
65	5.28×10^{11}	5.36×10^{11}	1.52%
60	3.75×10^{11}	3.80×10^{11}	1.33%
50	1.69×10^{11}	1.70×10^{11}	0.59%
40	6.09×10^{10}	6.04×10^{10}	-0.82%
30	1.46×10^{10}	1.40×10^{10}	-4.11%
25	5.33×10^{09}	5.08×10^{09}	-4.69%
20	1.35×10^{09}	1.25×10^{09}	-7.41%

calculates the total emitted flux (0 - 1220 eV), the agreement is better than 93% down to a blackbody of about 50 eV, but falls to 66% with a 25 eV blackbody due to the zeroed-out bin. On the other hand, if the flux integrals are computed from the third bin outwards (98.1 - 1200 eV), then the agreement is better than 93% even for blackbodies with temperatures as low as 20 eV. Such partial or truncated fluxes were used in unfolding the data from PBFA-II shot 6517 (see below).

The variance σ_i^2 for each XRD channel was assumed to have two components. The first uncertainty σ_{cable} was derived from the rms cable noise. This contribution was largely insignificant for near-peak signals. The second component σ_{rel} was a fixed percent, relative uncertainty ($\sigma_i = X\%D_i$), identical in each channel. One predicts such a component from the multiplicative, experimental factors (*e.g.*, solid angle and response functions) that are incorporated in the reduced data and that differ from channel to channel. For this initial work, the two uncertainties were combined to yield σ_i^2. Combining these terms in quadrature gave only negligible changes. Relative errors of 10-20% were estimated for the solid angle and response function measurements and yielded reasonable χ^2 probabilities (double-ended 5% confidence) for the unfolds at most of the sample times on shot 6517.

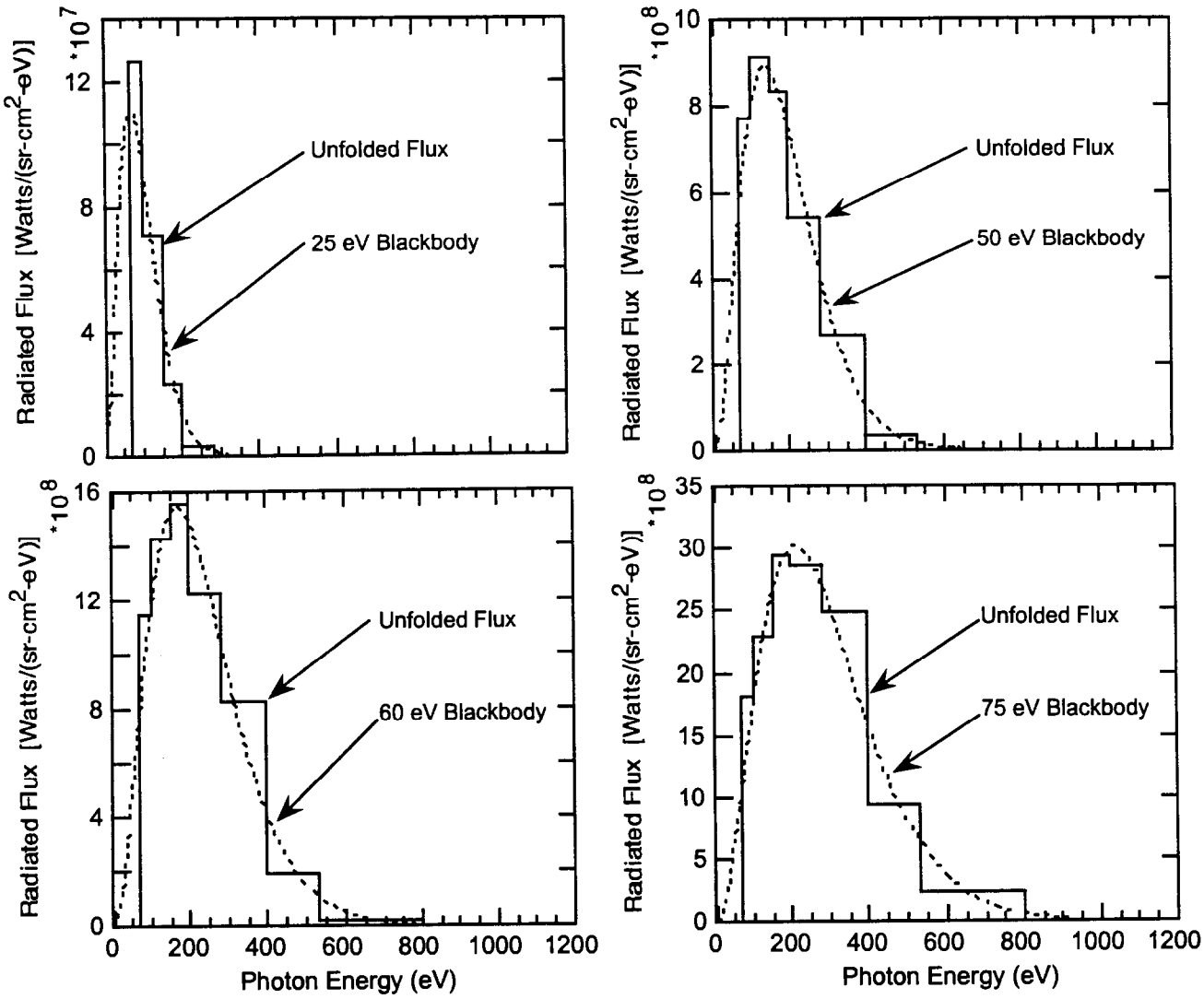

Figure 3. Unfolds of simulated data. In each figure the dashed curve is the blackbody source spectrum that is used to generate simulated data. The spectra unfolded from the simulated data are shown as the histrograms (solid lines).

Even if the unfolded spectra differ in analytic form from blackbody spectra, it is common practice to associate a *brightness temperature* T_{br} with the unfold. This parameter may be defined as the characteristic temperature of a pure blackbody spectrum with the same spectrally-integrated flux as the unfolded spectrum in question. Figure 4 shows a plot (dashed curve) of characteristic temperature versus integrated flux for the blackbody spectra $\Phi_{BB}(E,T)$ considered above ($25 \le T \le 75$ eV). The linear dependence on this scale reflects the Stephan-Boltzmann law. Thus, given a complete differential unfold spectrum, one can easily integrate the flux and interpolate T_{br}. It is also possible to infer a brightness temperature for an incomplete unfold spectrum (see below). That is, suppose that one could only estimate the spectrum over the energy interval $[E_1, E_{max}]$, where $0 < E_1 < E_{max}$. Also suppose that E_{max} is sufficiently large that the contribution to

the total flux from photons of energy above E_{max} is negligible in the comparison blackbody set. Then the *truncated* integral of the spectra from E_1 to E_{max} is still a monotonically increasing function of characteristic temperature, and one can still associate a similarly calculated flux from an unfold spectrum with a characteristic blackbody temperature. The solid curve in Figure 4 shows this association for E_1 = 91.6 eV and E_{max} = 1200 eV.

The peak-time unfold for PBFA-II shot #6517 is shown in Figure 5 (solid line). For this calculation the data in Figure 2 were input to the UFO code with the unfolding parameters just discussed. The dotted lines give the ±1σ unfold uncertainty, propagated from the estimated 20% 1σ errors in the reduced data. The χ^2 probability for fitting the data is 95%. Using the entire spectrum, one obtains a brightness temperature of 61±1 eV. A blackbody spectrum of this characteristic temperature is also shown for convenience. The unfolded spectrum differs noticeably from the blackbody spectrum in two ways: (1) the high energy tail of the unfold lies somewhat above the corresponding tail of the blackbody; and (2) there is a disproportionate peak in the first non-zero channel. The high energy tail may be physically reasonable, given (probable) asymmetric heating of the hohlraum target by Li ions (see Section 12 and Zel'dovich & Raizer[6]). However, the low energy peak is probably not real since a time-integrated spectrum, obtained at much finer energy resolution than the XRD array, showed

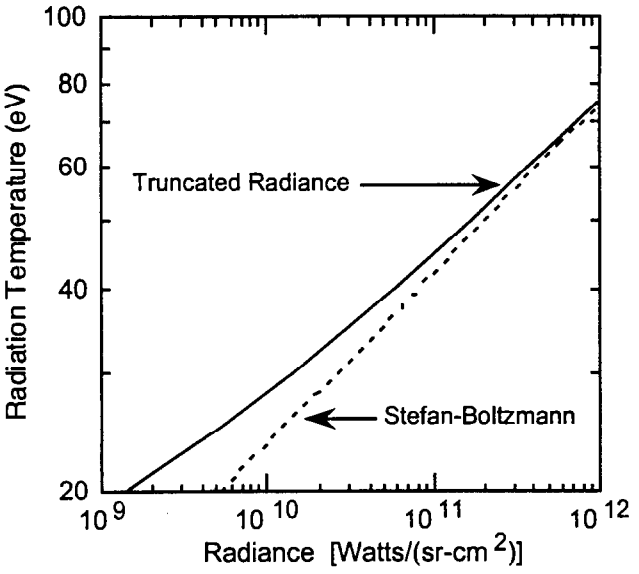

Figure 4. Characteristic temperature as a function of the integral of the differential energy spectrum for emitted flux as given by the Stefan-Boltzman equation (dotted line) and the integral between 98.1 and 1200 eV (solid line).

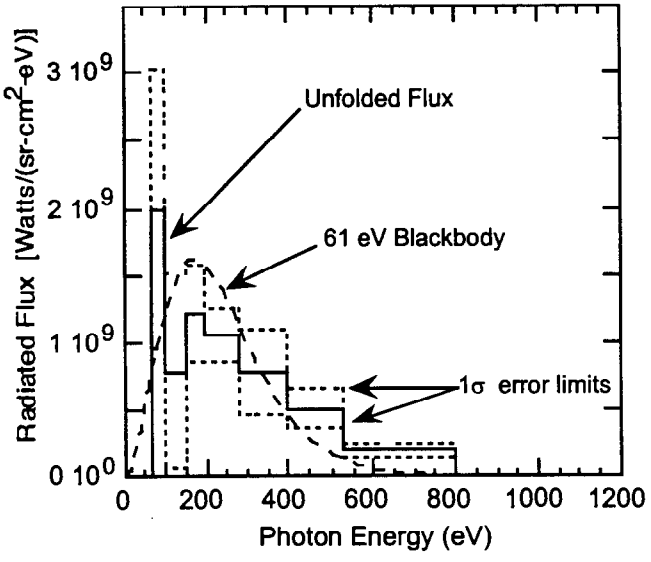

Figure 5. UFO unfold for shot 6517 at peak flux (81 ns). The solid curve gives the unfold derived from the reduced data of Figure 2. The dashed line is the equivalent blackbody spectrum.

no peak between 70 and 90 eV. Pending further studies, we decided to ignore the initial non-zero bin in the unfolded spectrum and to compute the brightness temperatures from the higher energy bins. Using the solid curve in Figure 4, one obtains a brightness temperature $T_{br} = 60.7 \pm 1.5$ for the peak unfolded temperature in shot 6517. We presently estimate that the overall uncertainty in the experimentally determined response functions may roughly double the uncertainty in T_{br}.

The anomalous initial peak in Figure 5 is presently believed to be due to systematic errors in the response functions at low photon energies, *i.e.,* at energies well below the calibration points certified at the Brookhaven x-ray source. The reasons for this belief are as follows: (1) The same data can be unfolded with different unfold parameters and basis functions, but the low energy feature remains (see Figure 6). Hence, the existence of the feature does not depend on the unfold parameters. (2) Systematic errors in the response functions, especially at low energies, can also distort the unfolded spectrum. One can show from *simulations*, for example, that if the data are simulated and unfolded with response functions having a multiplicative factor of 2 more sensitivity at photon energies below 200 eV, then the unfold in Figure 3 *can* grow a low energy peak, although the rest of the unfold spectrum remains intact (see Figure 7). (3) Although the original XRDs are no longer available, three similar XRDs were calibrated at the NIST SURFII facility in the 20 - 230 eV energy range. Overall, the sensitivity of these detectors was approximately 2x higher than extrapolated values below the aluminum L-edge at 72 eV. From 72 to ~ 120 eV the calibrated sensitivity was ~45% higher than the extrapolated response.

The analysis presented here is preliminary. While we expect no major changes in the results, it is clear that some adjustments need to be made in the analysis, and further questions need addressing. For example, more analysis is required of the experimental uncertainties and how to summarize these uncertainties in σ_i^2. Thus far, we have included some of the geometrical and noise errors, but calibration uncertainties in the response function errors are not included correctly. In principle, these lead to a nonlinear regression problem. Finally, there is interest in comparing the unfold solution itself (and not just its integral) to simple blackbody spectra. But these types of spectra are inherently different: one is a histogram and the other is continuous. In addition, one must account for distortions inherent in the unfold process with a given set of unfold basis functions and parameters. In the future we plan to address this problem by comparing the *unfold* of simulated data from known blackbody spectra with the unfold of the real data. This analysis can then be coupled with Monte Carlo simulations to estimate a goodness-of-fit parameter.

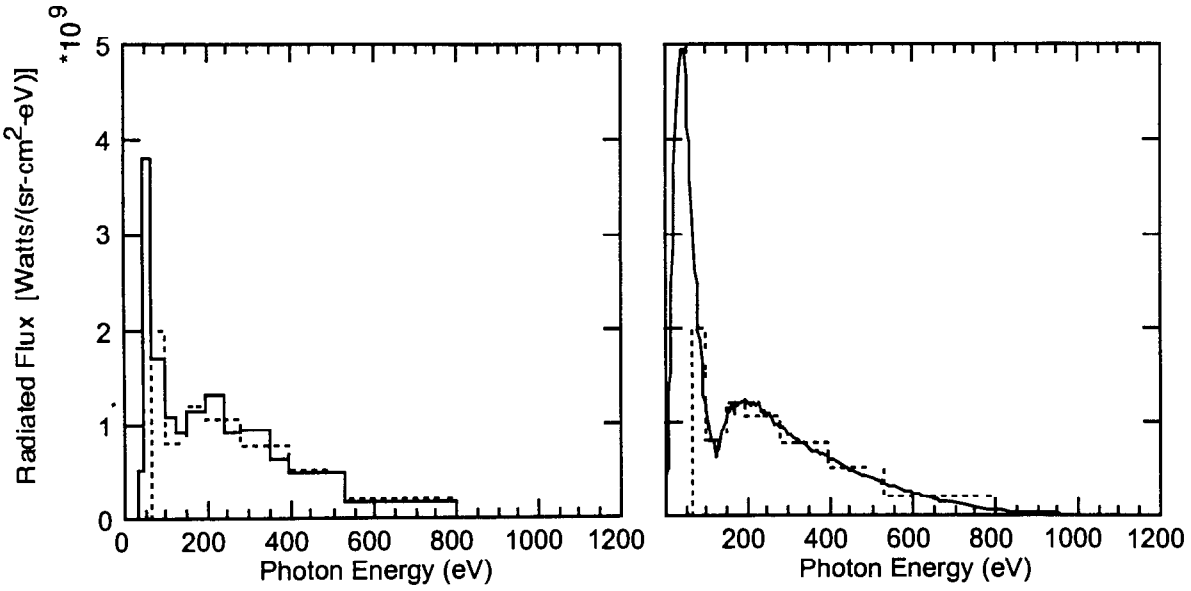

Figure 6. Unfolds of PBFA-II shot 6517 at peak flux with varied unfolding parameters. In Figure 6a the standard unfold is shown with dashed lines along with a spectrum in solid lines which was unfolded as an underdetermined system with additional smoothing constraints and first order B-spline (histogram) basis functions. In Figure 6b the standard unfold is shown along with basis functions consisting of blackbody spectra with characteristic temperatures of 20, 25, 30, 40, 50, 60, 65 and 70 eV. Negative coefficients in the sum were allowed in the unfold.

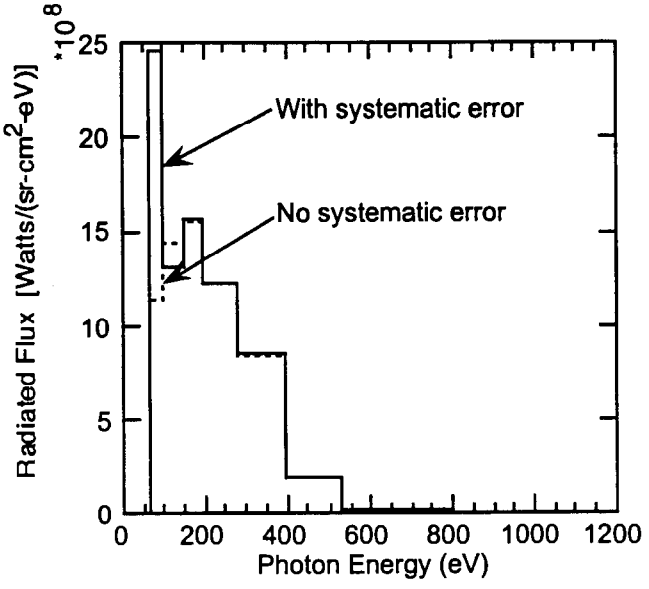

Figure 7. The effect of systematic errors in the low energy response functions can enhance the observed low energy flux. The dashed line is from an unfold of a simulated 60 eV blackbody spectrum. The solid curve results when the data are simulated with the first two response functions arbitrarily having a sensitivity increase of a factor of 2 for photon energies below 200 eV but then unfolded with the standard response functions.

References

[1] I. J. D. Craig and J. C. Brown, Inverse Problems-Astronomy (Adam Hilger, Boston, 1986).

[2] L. Kissel, F. Biggs, and T. Marking, "UFO (Unfold Operator): Command Descriptions," Version 4.0, Sandia National Laboratory Report – SAND82-0396 (Sandia National Laboratories, Albuquerque, NM, January 15, 1990), unpublished.

[3] C. L. Lawson and R. J. Hanson, "Solving Least Squares Problems" (Prentice-Hall, Englewood Cliffs, NJ, 1974).

[4] G. E. Forsythe, M. A. Malcolm, and C. B. Moler, "Computer Methods for Mathematical Computations." (Prentice-Hall, Englewood Cliffs, NJ, 1975).

[5] M. S. Derzon, private communication, 1994.

[6] Ya. B. Zel'dovich and Yu. P. Raizer, "Physics of Shock Waves and High-Temperature Hydrodynamic Phenomena," Academic Press, Vol. I, page 139, 1966.

Intentionally Left Blank

12. Experimental Scaling of Temperature and Intensity on Target - A. R. Moats

One of the most important goals for this 1994 target series was scaling the ion beam intensity with the achieved hohlraum temperature. Table 1 shows the tabulated lithium intensity-on-target and the corresponding brightness temperature as seen by the x-ray diodes or XRDs. The XRDs view the target through a diagnostic aperture which allow a line-of-sight to the foam and interior of the hohlraum. These temperatures are plotted as a function of the average target midplane intensity from the Ti "Bird Cage" fielded in the 1994 cylindrical target series in Figure 1. Also shown are the data from shots in the prior 1993 cone target series (ending with shot 6022). As already mentioned, the intensity values for the 1993 cone series were found retroactively from the 1994 power-coupling series, assuming the same voltage profile as for the 1994 cylindrical target series, and thus may have systematic errors due to changes in the diode. Note also that these shots were from cone targets with varying foam densities, and varying gold wall thicknesses, with the data unfolded from Ti strip K_α measurements from one quadrant only.

The error bars shown for the intensity values in Figure 1 are all errors in the absolute intensity unfold with the exclusion of the standard deviation in the average due to the azimuthal asymmetry. We are assuming a smooth beam behavior between azimuthal data points. As noted in the section on beam characterization from Section 8, the standard deviations for the asymmetry were as high as 86%. Since the 1993 cone targets used only one Ti strip measurement per shot, the relative percentile error for these values are greater than for the 1994 series.

Table 1. Intensity scaling on Target for 1993 and 1994 target experiments.

1993 Cone Targets

DAS Shot No.	Intensity (TW/cm^2)	Hohlraum Temperature (eV)
5936	0.61	48 ± 3
5942	1.89	58 ± 4
5975	0.78	50 ± 3
5979	1.50	46 ± 3
6000	1.05	
6022	0.19	

1994 Cylindrical Targets

6501	1.87	47 ± 2
6517	2.14	61 ± 2
6529	0.08	28 ± 1
6547	2.23	51 ± 1
6551	1.60	56 ±2
6554	2.04	52 ±1
6560	2.41	54 ±2
6569	1.36	55 ±2

In Figure 2, I show only the experimental data from the 1994 cylindrical target series. I also show the theoretical predictions for the dependence of the brightness temperature on beam intensity on target from LASNEX simulations for both 1.5-mm and 3-mm-aperture cylindrical targets [see Section 5]. LASNEX is a 2-dimensional hydrodynamics code with ion and laser energy deposition [Zimmerman and Kryer, 1975]. For these calculations, the assumed aperture reduces the temperature achieved in the hohlraum due to an energy "leak." For comparison, we also show the analytic curve [Dukart, 1995] for an optimized cylindrical target. The model used for this calculation is a simple zero-dimensional power-balance formula with no aperture. The data cluster about the integrated LASNEX predictions more closely than the analytic model calculation.

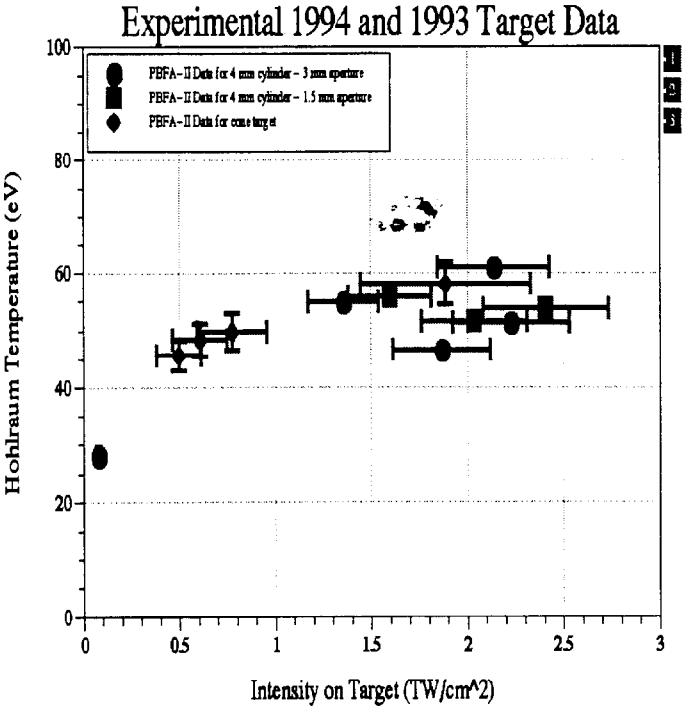

Figure 1. PBFA-II experimental data, showing average intensity on target and hohlraum brightness temperature as seen by the XRDs. Both cylindrical targets (with 3.0- and 1.5-mm diameter apertures) are shown with various wall thicknesses and foam densities. Error bars in temperature are smaller than the circle and square size for many of the experimental point (see Table 1).

As can be seen in Figure 2, the theoretical results for both 1.5-mm and 3-mm apertures are close enough that the scatter in the 1994 target series data blurs any such distinction in the targets. The lack of a temperature trend with aperture size indicates that hole-closure for the smaller 1.5-mm aperture is not a major factor for this kind of scaling study. We do appear to be consistent with the modeling for the cylindrical target. For all but one shot at low intensity, the 1994 target series data cluster about 2 TW/cm^2 power on target. The voltage and current in the accelerator portion of these six shots are quite similar. With this in mind, we then considered these shots to be repetitions of the same experiment. The PBFA-II diode was producing essentially the same nominal beam for these shots. In Figure 3, the experimental data from the 1994 cylinder target series are averaged together (with the exception of the outlier shot 6529). We show for this case an error bar for the intensity that does include the azimuthal asymmetry error. Averaging together the intensities for multiple shots minimize the effects of azimuthal asymmetries. Also shown with this datum is the results of LASNEX simulations. Again, the averaged data point is not inconsistent with our theoretical predictions based on LASNEX. However, more experiments with a more detailed and exact measurement of this asymmetric beam

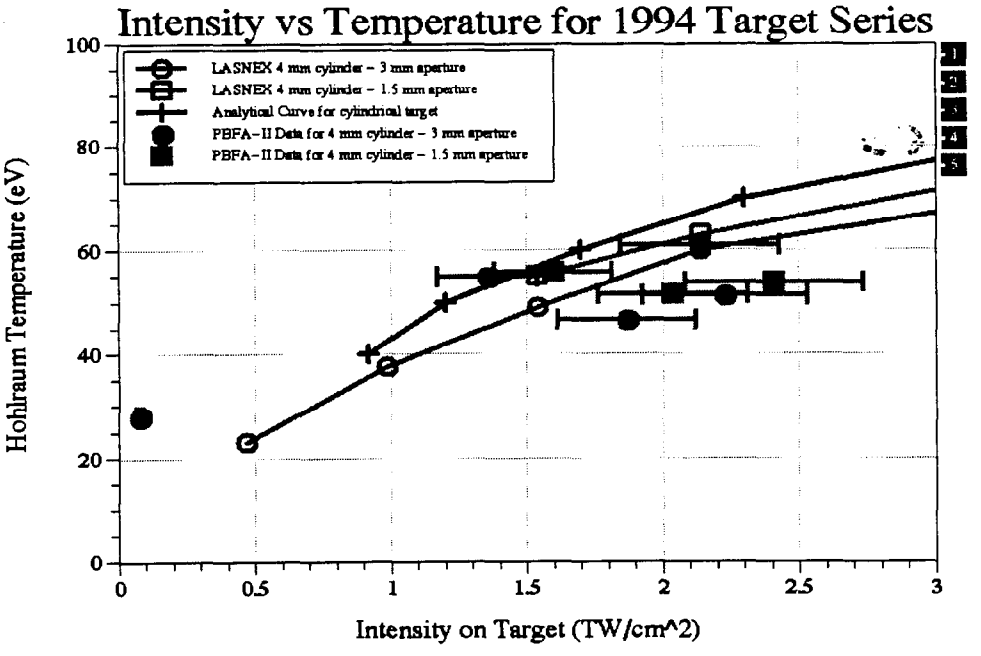

Figure 2. PBFA-II experimental data for the cylindrical targets fielded in 1994, as listed in Table 1 and shown in Figure 1, are shown together with the theoretical predictions discussed in Section 5. The analytical cylinder calculations and the LASNEX simulations for both the large and small aperture targets are shown. Error bars in temperature are smaller than the circle and square size for many of the experimental points (see Table 1).

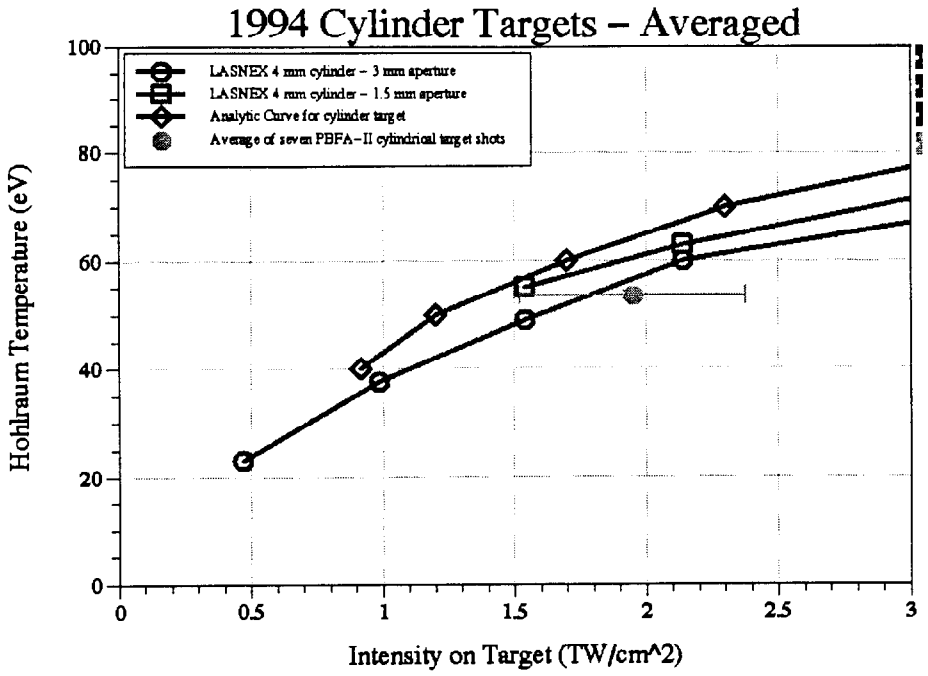

Figure 3. Here we show again the theoretical curves, both analytical and LASNEX, from Figure 2. We also averaged the seven shots from the 1994 cylindrical target series using the assumption that these shots were essentially the same experiment repeated. Only the outlier of shot #6529 was omitted. For this case, the error for this single datum does include the asymmetry error for the averaged intensity. Error bars in temperature are smaller than the circle size for the averaged experimental point.

(reducing our large error bars) or PBFA-II experiments with a more symmetric beam would be needed to reduce the data scatter.

In Figure 4, we show the PBFA-II data from the 1993 conical target series with the LASNEX simulations for the various wall thickness and foam densities. We must caution that there may be a systematic error from changes in the diode's voltage behavior between the dates of the 1993 series and the cross-calibration shots used to determine the absolute intensity in 1994. Bearing that in mind, however, there are still some comparisons to make. We seem to agree with theory at higher intensity, but disagree below 1 TW/cm^2 (indicated in a slope difference between data and theoretical curves). This indicates that a mere systematic increase or decrease of the absolute intensity would not solve this disagreement with the calculations.

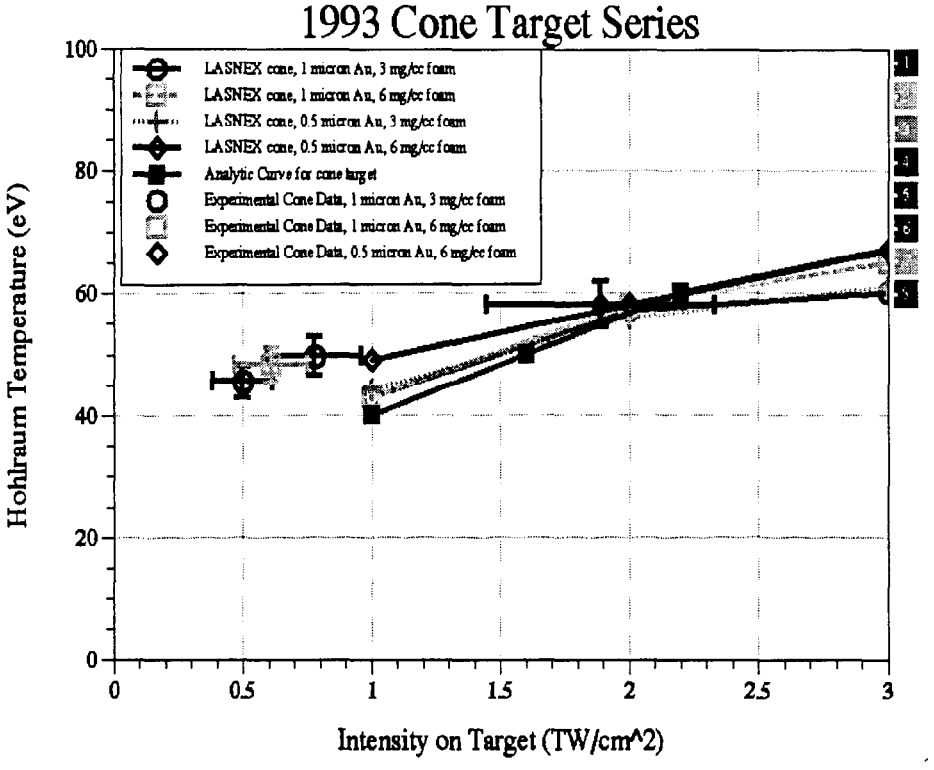

Figure 4. We show the experimental PBFA-II data for the 1993 conical target series, separated by gold wall thicknesses and foam densities, and the corresponding LASNEX calculations for brightness temperature versus ion intensity on target.

We have now enhanced our capability to measure absolute beam intensity on hohlraum targets. With this ability, we can now make quantitative comparisons between our simulations of hohlraum temperature scaling with beam power and our PBFA-II data. For the temperature-intensity scaling comparison to date, we are consistent within our large intensity scatter with theory for the cylindrical targets, specifically with the LASNEX simulations. However, there is a discrepancy on the absolute (and relative) comparison for the cone targets.

References

[1] Dukart, R.J. 1995, Rev. Sci. Instrum. 66(1), 747.

[2] Zimmerman, G. B., & Kruer, W. L. 1975, Commun. Plasma Phys. Control. Fusion 2, 51.

Intentionally Left Blank

13. Summary - A. R. Moats

We had four primary goals for this experiment: (a) understand and measure the beam properties, (b) achieve a 70 eV brightness temperature, (c) observe hole closure dynamics, and (d) scale the hohlraum temperature with the ion beam intensity-on-target for the cylindrical targets. We met a, c, and d with varying success. Regarding our temperature goal, we obtained 61 eV +/- 1.5 eV. In attempting each of these goals, we raised additional questions that can only be answered by further experiment on PBFA-II or another appropriate machine.

The first goal of understanding the beam properties is an ongoing activity for all PBFA-II experiments. Only with a large database of measurements can we hope to understand the numerous factors at play on an accelerator like PBFA II. Towards that goal, cross-calibration and setup shots were fired just prior to the Li-94 target series. D. J. Johnson (Section 3), using magnetic spectrometer and ion movie camera data, showed a diode operating at a peak lithium focus power of between 0.95 and 1.35 TW/cm^2 on a 60 degree sector of a flat-foil target (equivalent to 1.8 to 2.6 TW/cm^2 on the cylindrical targets used later) with a 13 - 16 ns full-width-at-half-maximum pulse. During the target series, the Ti "Bird Cage" diagnostic measured the time-integrated beam properties at 3 - 5 azimuthal positions at the target midplane. This included, for the first time, the absolute intensities. The data showed a rather asymmetrical beam (varying by factors of 3 in intensity azimuthally) that averaged to ~ 2 TW/cm^2 on target for most of the shots.

The primary purpose in achieving a 70 eV brightness temperature on the cylindrical hohlraums was to show significant progress in target heating on PBFA II. This progress was predicated on an increase in total beam power available on PBFA II (which never materialized) and the calculated increase in interior hohlraum temperature from the progression from cone geometry to cylindrical geometry. Our most reliable measurement of hohlraum brightness temperature is from the XRDs, as discussed by G. Chandler and D. Fehl in Section 11. The XRDs are absolutely calibrated and give time-resolved temperature, as opposed to the time-integrating bolometers. The highest peak brightness temperature of 61 eV +/- 1.5 eV occurred for shot #6517. Although this only shows a marginally higher hohlraum temperature than had been seen previously (58 eV for the cone series), it is consistent with the LASNEX prediction (discussed in Section 5 by Ray Dukart) of a hohlraum temperature of only 63.4 eV at the 2 TW/cm^2 intensity level incident on the target. To achieve 70 eV, our calculations indicate an intensity of 3 to 3.5 TW/cm^2 would have been required.

Hole closure dynamics were both modeled and observed directly and indirectly by numerous diagnostics. LASNEX simulations showed an aperture that for the first 4-5 ns of the power pulse closed slowly, but then eventually reached a maximum closing velocity of ~ 1.0 cm/sec. Sometime after 11- 13 ns, the foam fill tamped the aperture

walls open, and the aperture began to reopen. Diagnostic aperture closure was observed by M. S. Derzon, discussed in Section 9, in both time-integrated images from the soft x-ray pinhole cameras and the EST time-resolved measurements. He also saw an initial period of slow hole closure, followed by a maximum closure velocity of 2 cm/ms (the gold sound speed in vacuum), ending with an apparent slowing of the velocity due to the foam fill. The hole closure velocity did not change with increased intensity on target. The difference between the theoretical and experimental observation of maximum gold wall velocity may be due to a possible vacuum gap between the foam fill and the gold aperture and/or differences between the modeled voltage pulse and PBFA-II voltage. Most significant, however, is that analysis from G. Chandler demonstrates that the maximum hohlraum temperature is measured and achieved before significant aperture-closing has occurred (Section 11). XRD temperature measurements which showed no difference in the temperature achieved with 1.5-mm and 3.0-mm aperture targets indirectly support this conclusion.

The final goal was to scale the hohlraum temperature with the ion beam intensity-on-target. This allowed us to compare the integrated calculations from codes such as LASNEX with direct experimental data. R. J. Dukart, in Section 5, discusses these calculations and shows predicted curves of hohlraum temperature (brightness, interior radiation, and wall temperatures) versus ion beam power on target. These included 2-dimensional simulations with real apertures that give us the prediction of the 63.4 eV radiation temperature from the interior walls for a 2 TW/cm^2 power.

Some intriguing results do raise additional questions which need to be investigated in the future. These include the 10% - 30% mottling of the interior hohlraum intensity recorded by the soft x-ray pinhole cameras, the reason the bolometers showed a consistently 20% higher temperature than the XRDs for the cylindrical series, the higher-than-expected temperatures for the cone-target series at low intensity, the disagreement in peak hole-closure velocities, and a non-Planckian spectrum that included a high-energy tail. Improvements in diagnosing the incident beam as well as the spatial characteristics of the x-ray implosion will be required to reduce the scatter in the data and the error-bars on the data to more stringently test the calculations.

Distribution:

1	MS 0620	Donald Noack, 0011
1	1006	Terry Barber, 9651
1	1178	Juan J. Ramirez, 9580
1	1182	Doug Bloomquist, 9536
1	1182	David J. Johnson, 9514
1	1184	Jeff Kellogg, 9537
1	1186	James E. Bailey, 9574
1	1186	Michael Cuneo, 9574
1	1186	Michael Desjarlais, 9574
1	1186	Mark Kiefer, 9542
1	1186	Thomas Mehlhorn, 9574
1	1186	Stephen Slutz, 9574
1	1186	Mary Ann Sweeney, 9502
1	1187	Tom Haill, 9574
1	1187	Keith Matzen, 9570
1	1187	Eugene McGuire, 9574
1	1188	Roy Hamil, 9512
1	1188	Craig Olson, 9500
1	1190	Don Cook, 9500
1	1191	Jeffrey Quintenz, 9502
1	1193	John Maenchen, 9515
1	1194	Dillon McDaniel, 9540
1	1194	Stephen Rosenthal, 9544
1	1194	William Stygar, 9544
1	1196	Thomas Alberts, 9577
1	1196	Gordon Chandler, 9577
10	1196	Mark S. Derzon, 9577
1	1196	David Fehl, 9577
10	1196	Ray Leeper, 9577
1	1196	Richard Olson, 9577
1	1196	Anne Moats, 9577
1	1196	Carlos Ruiz, 9577
1	1196	Jose Torres, 9577
1	1196	Steven. Lazier, 9577
1	1407	Dora K. Derzon, 1811
1	1407	James Aubert, 1815
1	9018	Central Technical Files, 8940-2
2	0899	Technical Library, 4916
2	0619	Review & Approval Desk, 12690 For DOE/OSTI